UC413

LBL-28986

Lawrence Berkeley Laboratory

UNIVERSITY OF CALIFORNIA

Pion Correlations in Relativistic Heavy Ion Collisions at HISS

W.B. Christie, Jr.
(Ph.D. Thesis)

May 1990

For Reference

Not to be taken from this room

NUCLEAR SCIENCE DIVISION

LBL-28986
Copy 1
Bldg. 50 Library.

Prepared for the U.S. Department of Energy under Contract Number DE-AC03-76SF00098.

DISCLAIMER

This document was prepared as an account of work sponsored by the United States Government. While this document is believed to contain correct information, neither the United States Government nor any agency thereof, nor the Regents of the University of California, nor any of their employees, makes any warranty, express or implied, or assumes any legal responsibility for the accuracy, completeness, or usefulness of any information, apparatus, product, or process disclosed, or represents that its use would not infringe privately owned rights. Reference herein to any specific commercial product, process, or service by its trade name, trademark, manufacturer, or otherwise, does not necessarily constitute or imply its endorsement, recommendation, or favoring by the United States Government or any agency thereof, or the Regents of the University of California. The views and opinions of authors expressed herein do not necessarily state or reflect those of the United States Government or any agency thereof or the Regents of the University of California.

LBL - 28986

Pion Correlations in Relativistic Heavy Ion Collisions at HISS

By

William Bennett Christie Jr.

B.S. (Western Washington University)1980

M.A. (University of California, Davis) 1985

Dissertation

Submitted in partial satisfaction of the requirements for the degree of

DOCTOR OF PHILOSOPHY

in

Physics

in the

GRADUATE DIVISION

Of the

UNIVERSITY OF CALIFORNIA

DAVIS

This work was supported by the Director, Office of Energy Research, Division of Nuclear Physics of the Office of High Energy and Nuclear Physics of the U.S. Department of Energy under Contract DE-AC03-76SF00098

This thesis is dedicated to my parents, and my brothers and sisters, for their enthusiasm and support throughout my graduate studies, to my wife Karen for her love, support, and unending patience while I've pursued my Doctorate degree, and to my young daughter who, though she doesn't yet walk, talk, or even have any teeth, has provided me with a lot of motivation to finish up my graduate career.

Acknowledgements

There are many people I'd like to thank for their assistance in the setting up and running of experiment E684H. These people are T. Abbot, D. Beavis, F. Beiser, F.P. Brady, H. Crawford, I. Flores, S.Y. Fung, D. Keane, P. Lindstrom, Y. Liu, W. Mueller, D. Olson, J. Romero, T.J. Symons, C. Tull, and H. Wieman.

I'd like to especially thank W. Mueller for writing the acquisition code, C. Tull for assistance with Fortran, Macintosh applications, and general computer questions, and H. Wieman for generally organizing HISS.

I'm indebted to H. Crawford for graciously loaning me a Macintosh computer for the extended period of time necessary to prepare this thesis.

I'm grateful to Associated Western Universities for financial support.

I'd like to acknowledge the discussions I've had with J. Rasmussen.

I thank J. Draper for serving on my thesis committee and assistance in my Graduate studies.

I thank S.Y. Fung for allowing me to use the data from E684H for this thesis, as well as for serving on my thesis committee and offering suggestions in the writing of this thesis.

I thank my thesis advisor, F.P. Brady for, among other things, guiding me through my graduate studies, support, and making numerous valuable suggestions in the writing of this thesis.

Last, and foremost, I'd like to thank Doug Olson for his invaluable and extensive collaboration in all phases of running, analyzing, and interpreting the results of, experiment E684H.

This work was also supported by the:

Nuclear Science Division

Lawrence Berkeley Laboratory

University of California

Berkeley, California 94720

and by the Director, Office of Energy Research, Division of Nuclear Physics of the U.S. Department of Energy under Contract DE-AC03-76SF00098.

Introduction 1

Chapter 1. Physics Motivation 3

Intensity Interferometry 6

Short Derivation of Theoretical Correlation Function 9

Experimental Extraction of Correlation Function 14

Chapter 2. Experimental Apparatus 19

HISS 19

Experimental Setup 19

Upstream Detectors 21

V1 Soft Collimator 21

Start Scintillator 21

Vectoring and Beam ID 23

S2-V2 Beam Definition Counters 27

Target Wheel 28

Downstream Detectors 29

V4 Trigger Scintillator 29

Black Time of Flight Wall 29

HISS Drift Chamber 30

Time of Flight Walls 33

Targets and Beams 33

Triggers and Data Set 34

Chapter 3. Analysis 41

Computers 41

Analysis Shell LULU 42

First Pass, Tracking 43

Second Pass, Momentum Reconstruction 61

Momentum Resolution 64

Particle Identification 68
Cuts Applied to Data 70
Third Pass, Matrix Filling 71
Fourth Pass, Fitting 77
Method used for Fitting 78
Cuts Applied in Fit 83
Systematic Corrections 89
Acceptance 100
Chapter 4. Results 105
Central Collision Data 107
Argon on KCl 107
Argon on Lanthanum 115
Xenon on Lanthanum 119
Peripheral Collision Data 121
Argon on KCl 121
Chapter 5. Discussion 126
General 126
Comparison with Results of others 133
Conclusions 136
Future Work 137
References 139
Appendix A 143

Introduction

This thesis contains the setup, analysis, and results of experiment E684H "Multi - Pion Correlations in Relativistic Heavy Ion Collisions".

The goals of the original proposal were:

1.) To initiate the use of the HISS facility in the study of central Relativistic Heavy Ion Collisions(RHIC).

2.) To perform a second generation experiment for the detailed study of the pion source in RHIC.

The first generation experiments, implied by the second goal above, refer to pion correlation studies which the Riverside group had performed at the LBL streamer chamber[1 - 7]. The major advantage offered by moving the pion correlation studies to HISS is that, being an electronic detector system, as opposed to the Streamer Chamber which is a visual detector, one can greatly increase the statistics for a study of this sort. An additional advantage is that once one has written the necessary detector and physics analysis code to do a particular type of study, the study may be extended to investigate the systematics, with much less effort and in a relatively short time.

I believe that in reading this thesis one will conclude that both the primary goals of this experiment have been successfully achieved.

This thesis is organized into five main sections. These sections are the Physics motivation for this experiment, the experimental setup and detectors used, the pion correlation analysis, the results, and the conclusions and possible future directions for pion studies at HISS. If one is not interested in all the details of the experiment, I believe that by reading the sections on intensity interferometry, the section on the fitting of the correlation function and the systematic corrections applied, and the results section, one will get a fairly complete synopsis of the experiment.

I'll end this introduction with a short history of the experiment and how I became involved with it. The proposal for the experiment was originally submitted to, and approved by, the Spring 1983 BEVALAC Nuclear Science Program Advisory Committee, by a collaboration from the University of California, Riverside, and the Lawrence Berkeley Laboratory (LBL). The running of the experiment was initially planned for the Spring of 1984, pending completion of what was to be a 2 m × 5 m Drift Chamber (DC) for the Heavy Ion Spectrometer System (HISS) facility at the Lawrence Berkeley Laboratory BEVALAC. On analysis of the data from the 1 m × 2 m prototype[8] for the large Drift Chamber it was decided to scale back the size, and change the design for the HISS DC. The new design was prototyped[9] and used in an experiment[10] (E772H), and the Large 1.5 m × 2 m DC was constructed and tested in early 1987. By this time, almost four years after the experiment was proposed, many of the personnel who were to run and analyze the experiment had moved on to other jobs and projects. I'd been working with the HISS group part - time for a number of years by this time, building and using the Multiple Sampling Ionization Chamber[11] (MUSIC) in a collaborative effort between the University of California, Davis, and LBL, and assisting in the running of the various experiments run at HISS. It was while actually running this experiment (E684H) that the offer was made that I could have the data for my thesis experiment, and the rest, as they say, etc.

Chapter 1. Physics Motivation

Relativistic heavy ion collisions have been studied in experiments at the BEVALAC for almost twenty years now. One of the primary interests in these studies has been to investigate how nuclear matter behaves at the high temperatures and pressures achieved in these collisions. As one cannot solve directly the many - body problems present in analyzing these heavy - ion collisions, the tack taken by most theorists in this area of study is to describe these reactions in the language of thermodynamics. This being the case, one then talks about investigating the equation of state of the nuclear matter in these collisions, and measuring such parameters as the pressure, temperature, volume, entropy etc[12]. I'll briefly describe below a few of the experimental techniques used to extract some of these properties for these collisions, ending with the technique of pion interferometry which is the topic of this thesis.

A simple geometric model is usually used when describing high energy nucleus - nucleus collisions. In this model[13 - 15]commonly referred to as abrasion - ablation or cascade - evaporation, when the two nuclei collide the overlap regions of the two nuclei interact with one another, forming a hot, dense, interaction region, while the remaining parts of the projectile and target nuclei are left largely unaffected aside from some excitation energy. See Figure #1.1 below. It is this interaction region which we wish to study.

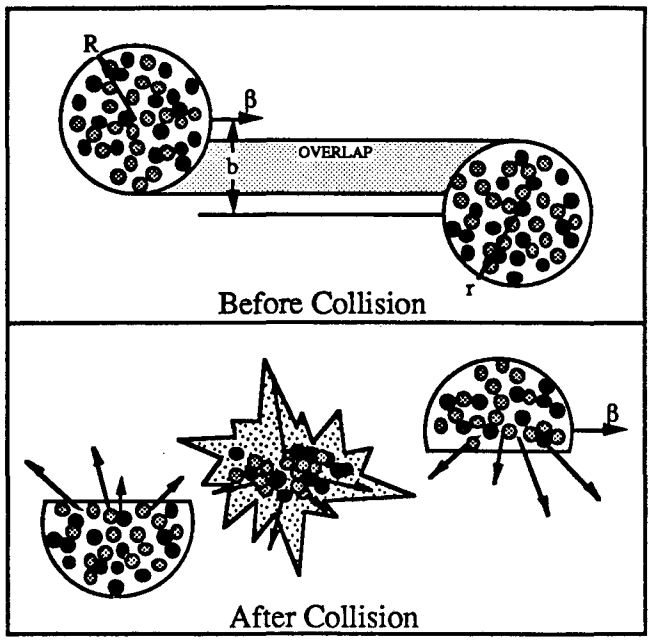

Figure #1.1 Schematic of a Relativistic Heavy Ion Collision.

One of the parameters which one would like to extract for the nuclear matter in this interaction (aka participant) region is the mean kinetic energy of the participants. To extract some measure of the mean kinetic energy of the nucleons, pions, kaons etc in this hot region, a standard technique is to plot the cross section for a particular species of particle versus energy. One then fits a line to the slope of this energy distribution (on a log plot) for the various types of particles which come out of this region[16]. These distributions fall off exponentially with increasing energy, similar to what one sees in a Boltzman distribution. The slope of these fit lines is commonly referred to as merely the slope parameter or, loosely, as the temperature. As the different types of particles have different mean free paths in the nuclear matter, and hence escape the interaction region at different times after different numbers of rescatterings, one may use this technique to probe the time - evolution of this measure of the mean kinetic energy.

The entropy produced in these collisions is thought to be extracted by looking at the yields of composite particles which come out of the interaction region. Keeping in mind that the entropy of a system is the log of the density of states available to a system, the general idea is that the higher the percentage of single nucleons (protons and neutrons) and light nuclei, the larger the number of final states available to the system, and hence the higher the entropy. Early uses of this idea were to merely look at the ratio of "d" like to "p" like (i.e. deuteron like and proton like) nuclei and fragments, with various definitions for these

species, to measure the entropy. There are now more sophisticated theories[17] in which one measures the mass yield distribution and fits the shape. As the entropy is a measure of the number of degrees of freedom of a system, and the number of degrees of freedom of a system changes when a phase transition occurs, it's thought that measurements of this type may be useful to search for phase transitions in nuclear matter.

As the pions that come out of these collisions are not free in the normal nuclear matter of the projectile and target, and are created in the interaction region of these collisions, they are a natural probe to use in the study of the overlap region. The slope parameters which one extracts from the cross section versus energy plot for the pions is interpreted as a measure of the mean kinetic energy for the later stages of the expansion and cooling of the interaction region, due to the large πN cross section. It has been observed[18] that the total pion production in these relativistic heavy ion collisions is less than what one would predict if the collisions are modeled merely as a succession of nucleon - nucleon interactions (cascade model)[19]. One interpretation of this observation has been that some fraction of the energy available for pion production is taken up as some sort of compressional energy. Theorists have thus used the pion yield to test their models and as a way of getting some idea what the compressibility of nuclear matter is.

To extract some measure of the volume of the system, and, if one knows the number of participants, the density, one may use the correlations of identical particles[20-27]. It is this technique, and its application to a few different projectile - target combinations which is the subject of this thesis. In addition to, and many would say more interesting than, the space - time extension of the pion source, there are theories which indicate that one may be able to use the magnitude of the pion correlation effect to extract information on the degree of coherence of the pion source.

Experimental evidence for the existence of correlations in particle momenta in high energy collisions due to the type of statistics the particles follow, either Fermi - Dirac or Bose - Einstein , has been around for about thirty years. The theory necessary to see how

one expects this effect to manifest itself in the data is basic quantum mechanics, as I shall show shortly. The complexity in extracting meaningful information out of a particle correlation analysis can be separated into two general categories. These categories are:

1.) What other processes distort the particles momenta, in this case negative pions, coming out from the nuclear collisions, by how much are they distorted, and how will it show up in the analysis.

2.) What quantities is one actually measuring.

Intensity Interferometry

Brief History

Before giving the generic derivation of the correlation function which is fit to the data for these collisions I'll give a brief history. The first experimental evidence that some measure of the size of the pion source could be obtained from the phase space density of the emitted pions momenta was obtained by Goldhaber[28] *et al* while analyzing $\bar{p}$ - p annihilations in the late 1950s. What they observed was that the opening angles were, on average, smaller for the like sign pions than for the unlike sign pions. The Fermi statistical model they were using to interpret their data predicted no such effect. They found that by symmetrizing the two particle wavefunctions for the identical (like sign) pions, and using a reaction volume with a radius of ≈ 0.75 times the Compton wavelength of the pion (≈ 1.08 fm), they could reproduce their results using the statistical model. They concluded, cautiously, that as the prediction via their model was very sensitive to the size one chose for the reaction volume, this technique of varying the reaction volume to fit the opening angle distributions may be useful to extract the spatial extent of the source. Due to the pioneering nature of their work, this effect is often referred to as the GGLP effect (Goldhaber, Goldhaber, Lee, and Pais, authors of paper).

Through the 1960s various particle physics groups continued to study these opening angle distributions over a wide variety of colliding systems and energies. As the

number of particles coming out of the systems increased it became much more difficult to apply the GGLP technique. In the early 1970s a number of theorists[21-27], at roughly the same time, realized that the GGLP effect was analogous to the Hanbury-Brown and Twiss (HBT) effect in radio and optical Astronomy. This lead to a much more straight forward technique of analyzing the data to extract the space time information for the pion source.

The HBT effect, which the authors came up with in the early 1950s, was the realization that one could use the second - order interference of photons (due to the fact that the photons are bosons) to measure the angular size of stars using not only radio waves but also visible light. Second order interference differs from first order interference in that the fluctuations which one observes are in the intensity rather than the amplitude of the interfering photons.

In the HBT analysis technique[29] to measure the angular size of stars using visible light, one sets up two optical telescopes separated by some distance, roughly perpendicular to the line of sight to the star to be measured. One then puts a filter on each telescope to transmit only light in some small interval around some frequency ω. The transmitted light for each telescope is focused onto a photomultiplier tube and the output of the tubes passed through low pass filters which only pass frequencies in the range of the difference of the frequencies transmitted by the optical filters (possible beat frequencies for the system). The two outputs of these low pass filters are then put into a correlator which in the case of HBT was a linear mixer that put out the average value of the product of the currents from the two phototubes. HBT then put the output of this correlator into an integrating motor and merely used the revolution counter on the motor as their measure of the degree of correlation. Hanbury - Brown shows using the simple example where one just considers the light from two atoms located on opposite limbs of a star that by writing down the intensity of the electric field at the two telescopes due to the atoms, and calculating the product of the two currents which get to the correlator, one ends up with the following:

$$i_{corr} = A \cos\left(2\pi \frac{d\theta}{\lambda}\right)$$

where i_{corr} is the current out of the correlator, A is a constant proportional to the product of the intensities due to the two atoms and any detector efficiencies, d is the distance between the two telescopes, θ is the angular size of the star, and λ is the mean wavelength of the light. Therefore we see that if $\frac{d\theta}{\lambda} < 1$, one may vary the distance, d, between one's telescopes and, using the above equation, extract the angular size of the star.

The simple method used by Hanbury - Brown in the example above relied solely on the wave nature of electromagnetic radiation. He goes on to give a very brief explanation of the HBT effect where one uses the particle nature of the photons. First he considers nearly monoenergetic light ($\Delta\nu / \nu << 1$) falling on a detector. One observes, as a function of the resolving (observation) time τ, the probability that if one observes a photon at one of the detectors that one will also observe a photon at the other. He calls this the conditional probability function $p_c(\tau)\, d\tau$ and defines it as shown below:

$$p_c(\tau)\, d\tau = \alpha I [1 + |\gamma_{11}(\tau)|^2]\, d\tau$$

$$\text{where: } \gamma_{11}(\tau) = \int_0^\infty G(\nu) \exp(-2\pi i \nu \tau) d\nu \Big/ \int_0^\infty G(\nu) d\nu$$

α is the quantum efficiency of the phototube, I is the average intensity at the detector over a few cycles, and $\gamma_{11}(\tau)$ is what he refers to as the normalized auto - correlation function of the incident light.

In his example he assumes that one has a beam of plane polarized light with a Gaussian spectral density $G(\nu)$ of width $\Delta\nu$. He then states that the probability of detecting the second photon is twice as likely if the resolving time $\tau << \frac{1}{\Delta\nu}$ than if $\tau >> \frac{1}{\Delta\nu}$. This is what one would expect due to the fact that the photons are bosons. It's known from quantum mechanics that the probability of a boson going into some state is twice as likely if there is already another boson in the state[30] (indeed, if there are n bosons already in the state the probability of an additional boson going into the state is increased by (n + 1)

factorial.). The conditions on the resolving time above can be understood by using Heisenberg's uncertainty principle. Two photons will be in the same state if the product of the difference in their momenta and positions are close to the physically realizable limit given by the uncertainty principle. As shown below, for photons this relation may be transformed to a function of the arrival times and frequency difference.

$$\Delta p\, \Delta x \geq \frac{\hbar}{2}$$

$$\frac{h\Delta\nu}{c}\Delta x \geq \frac{\hbar}{2}$$

$$\frac{\Delta x}{c} \geq \frac{1}{4\pi\Delta\nu}$$

$$\Delta t \equiv \tau \geq \frac{1}{4\pi\Delta\nu}$$

What this shows is that for $\tau << \frac{1}{\Delta\nu}$, the photons are likely in the same state and one would expect the probability of detecting a second photon after observing the first to be twice as likely as the case in which $\tau >> \frac{1}{\Delta\nu}$. The point to keep in mind is that it's the fact that photons are bosons and as such obey the Bose - Einstein statistics, which allows the photons to have large occupation numbers in a state and allows for fluctuations in the occupation number in these states.

Short Derivation of Theoretical Correlation Function

Moving on now to the application of intensity interferometry in particle physics the explanation will be entirely in terms of quantum mechanics. The very short derivation which I will give can be found in many papers[24,27,31]. There are more sophisticated derivations in the literature which lead to the same result. I've tailored the example below to the case at hand (pion interferometry), but most of the arguments apply to any identical particles, the exception being that if the particles are fermions the exchange term in the two particle counting probability is preceded by a negative sign and one ends up with an anti - correlation.

Referring to figure #1.2 below, suppose that there are two identical pions emitted from the interaction region at points r_1 and r_2 which are detected at the two positions x_1 and x_2, with momenta p_1 and p_2 respectively. (Note: x_i, r_i, and p_i are all four vectors here.)

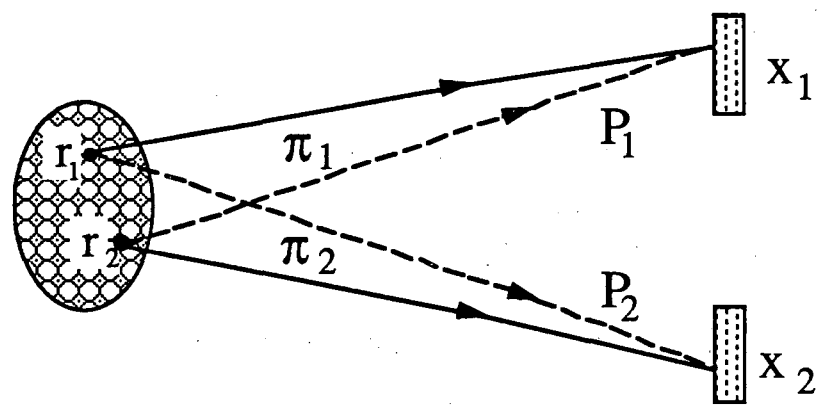

Figure #1.2

As the pions are identical bose (integer spin) particles, and one can't tell whether the pion detected at X_1 came from r_1 or r_2, and likewise for the pion detected at X_2, one must write down both possible histories which lead to the observed final two pion state. Namely, pion #1 coming from r_1 and pion #2 coming from r_2, and vice versa. The probability amplitude for this process is thus:

$$A(1,2) \propto \frac{1}{\sqrt{2}} \left\{ e^{ip_1 \cdot (x_1 - r_1)} e^{ip_2 \cdot (x_2 - r_2)} + e^{ip_1 \cdot (x_1 - r_2)} e^{ip_2 \cdot (x_2 - r_1)} \right\}$$

The proportional sign is used instead of the equal sign as there are some unimportant phase factors which are not included in the above expression. The probability is just the square of the probability amplitude which yields:

$$|A(1,2)|^2 = \left\{ 1 + \cos[(p_1 - p_2)\cdot(r_2 - r_1)] \right\}$$

If one now makes the non-trivial assumption that the pion emitting sources are uncorrelated, with a space - time distribution given by $\rho(r,t)$, the two pion counting rate may be calculated by integrating over the pion emitting region.

$$P(p_1,p_2) = \int |A(1,2)|^2 \rho(r_1,t_1)\rho(r_2,t_2) d^4r_1 d^4r_2$$

$$= 1 + |\rho(q,q_0)|^2 \equiv C_2(q,q_0)$$

where $q = | p_1 - p_2 |$ is the relative three momentum, $q_0 = | E_1 - E_2 |$, and $\rho(q,q_0)$ is the Fourier transform of the pion emitting source distribution. This function $C_2(q,q_0)$ is what I'll refer to as the two pion correlation function.

In the derivation above we see that as long as the two possible histories are indistinguishable, and the pion emission is chaotic, one ends up with an *interference* term. Before I continue with choosing a pion source distribution and detailing how I fit this theoretical expression to the experimental data, I'll briefly discuss the importance of this assumption about the chaoticity of the pion emitting sources.

The assumption made above was that the pion emission is chaotic. If the pion emitted from r_1 and r_2 are not independent the enhancement expected in the two pion correlation function will not appear. This is a general property of second order (intensity) interferometry that the sources must be uncorrelated and the point is made in a number of papers. To show this effect I'll reproduce the example given by M.G. Bowler[32]. Referring to figure #1.2, suppose that the two sources at r_1 and r_2 are coherent (i.e. f_a and f_b below are fixed relative to one another). The amplitude to get a pion of momentum k_1 would be:

$$A(1) = f_a e^{i\mathbf{k}_1 \cdot \mathbf{r}_1} + f_b e^{i\mathbf{k}_1 \cdot \mathbf{r}_2}$$

The probability for the emission of this pion is:

$$| A(1)|^2 = [f_a^2 + f_b^2 + (f_a f_b^* e^{i\mathbf{k}_1 \cdot (\mathbf{r}_1 - \mathbf{r}_2)} + cc)]$$

The joint probability amplitude for emission of a pion with momentum k_1 and one with k_2 is:

$$A(1,2) = (f_a e^{i\mathbf{k}_1 \cdot \mathbf{r}_1} + f_b e^{i\mathbf{k}_1 \cdot \mathbf{r}_2}) \cdot (f_a e^{i\mathbf{k}_2 \cdot \mathbf{r}_1} + f_b e^{i\mathbf{k}_2 \cdot \mathbf{r}_2})$$

which leads to the joint probability:

$$P(1,2) = [f_a^2 + f_b^2 + (f_a f_b^* e^{i\mathbf{k}_1 \cdot (\mathbf{r}_1 - \mathbf{r}_2)} + cc)] \cdot [f_a^2 + f_b^2 + (f_a f_b^* e^{i\mathbf{k}_2 \cdot (\mathbf{r}_1 - \mathbf{r}_2)} + cc)]$$

This is just the product of the single pion emission probabilities. As the correlation function is the joint probability divided by the product of the singles probabilities, we see that when the sources are correlated the correlation function is flat, i.e. shows no enhancement for the

close π^- pairs. If we now suppose that the sources are totally chaotic (i.e. f_a and f_b fluctuate randomly), the averages of all the terms which are multiplied by linear terms in f_a times f_b will average to zero and one is left with:

$$<P(1,2)> = (f_a^2 + f_b^2)^2 + 2f_a^2 f_b^2 \cos(\Delta \mathbf{k} \cdot \Delta \mathbf{r})$$

$$<P(1)> <P(2)> = (f_a^2 + f_b^2)^2$$

which, if one assumes that $f_a \approx f_b$, leads to a normalized two pion counting probability of:

$$\frac{<P(1,2)>}{<P(1)> <P(2)>} = 1 + \frac{1}{2}\cos(\Delta \mathbf{k} \cdot \Delta \mathbf{r})$$

Bowler goes on to point out that the one - half in front of the interference term above is due to using only two sources. If one uses n sources the multiplier is:

$$(1 - \frac{1}{n}).$$

When one goes from the discrete sum of sources to integrating over the sources the factor above becomes equal to one and we're back to the form of the two pion counting probability derived earlier.

Getting back to the derivation, recall that the two pion correlation function was found to be:

$$C_2(q,q_0) = 1 + |\rho\ (q,q_0)|^2$$

To continue one must make some assumption for the form of the pion emitting source distribution. Following the work of Yano and Koonin[25] we've chosen to use their gaussian distribution for the spatial and temporal distribution. In its most general form this distribution is parameterized as:

$$\rho(r_x, r_y, r_z, t) = \frac{1}{\pi^2 R^3 \tau}\ e^{(-r_x^2/R_x^2 - r_y^2/R_y^2 - r_z^2/R_z^2 - t^2/\tau^2)}$$

which may be written:

$$\rho(r_\perp, r_{//}, t) = \frac{1}{\pi^2 R^3 \tau}\ e^{(-r_\perp^2/R_\perp^2 - r_{//}^2/R_{//}^2 - t^2/\tau^2)}$$

or, with the assumption that $R_\perp = R_{//}$ as:

$$\rho(r,t) = \frac{1}{\pi^2 R^3 \tau}\, e^{(-r^2/R^2 - t^2/\tau^2)}.$$

$R_\perp$ and $R_{//}$ above refer to the directions transverse to, and parallel to, the beam, respectively. For ease and clarity I will use the last form in most of the discussion but will also be fitting the correlation function which results if one uses $\rho(r_\perp, r_{//}, t)$ in the results section.

Putting $\rho(r,t)$ into the integral given earlier for $C_2(q,q_0)$ leads to:

$$C_2(q,q_0) = 1 + e^{(-q^2R^2/2 - q_0^2\tau^2/2)}$$

Notice that the expression for C_2 above goes to the value of two as q and q_0 both go to zero. This is merely due to the property of bosons mentioned earlier, i.e. that the probability of a boson going into a state is twice as likely if there is already a boson in the state. In practice it has been observed that the experimentally determined correlation very seldom reaches the value of two at the origin. To get a better fit to the data it was first suggested by M. Deutschmann[33] *et al.* to put another fit parameter in front of the exponent in the function above. This parameter, typically given the symbol lambda, is usually referred to as the chaoticity or coherence parameter. It allows for a decrease in the magnitude of the two pion enhancement due to partial coherence of the emitted pions as well as other correlations[34] imposed on the pions. Some of the various interpretations of this parameter are discussed in the results section. Our final theoretical two - pion correlation function is thus:

$$C_2(q,q_0) = 1 + \lambda e^{(-q^2R^2/2 - q_0^2\tau^2/2)}$$

Before proceeding to describe how this correlation function is extracted from the data, I'd like to present a rough idea on the range in relative momentum of the pion pairs for which one expects to see this effect. Analogous to the arguments given earlier to explain the HBT optical interferometer in terms of the particle nature of the photons, one can use the uncertainty principle to determine how far out in the relative momentum (q) one expects the enhancement in the two pion counting rate to go. I'll take for the uncertainty in the position of the sources of the pions the equivalent sharp sphere radius of whatever nucleus

is to be used in the collision. This Δx can be estimated with a simple equation as shown below. Now, given that I have this position uncertainty for the sources of the two pions, and that one expects an enhancement in the counting rate for pions which come from the same state, what is the range in relative momentum Δp_i, for pions which come from the same state? I can use the uncertainty principle to estimate this as shown below.

$$\Delta p_i \Delta x \approx \hbar$$

$$\Delta x \approx R \approx r_0 A^{\frac{1}{3}} = 4.1 \text{ fm for Argon}$$

$$\rightarrow \Delta p_i \approx 50 \text{ MeV/c}$$

$$\rightarrow q \equiv \sqrt{\Delta p_x^2 + \Delta p_y^2 + \Delta p_z^2} \approx 85 \text{ MeV/c}$$

This will be seen later to be a fairly accurate estimate of the range of the enhancement in the two pion counting rate. Experimentally one turns this process around. One observes an enhancement, for some range of Δp, in the counting rate for pion pairs which come from the same nuclear collision. One then makes an assumption about the distribution function for the pion emitters in the pion emitting region and derives an expected shape and size for the observed enhancement in the relative momentum and energy of the pion pairs which is a function of the size of the pion emitting region and its lifetime, as was shown earlier.

Experimental Extraction of Correlation Function

The theoretical two pion correlation function is defined as the normalized ratio of the inclusive two pion cross section divided by the product of the single pion cross sections.[26]

$$C_2(\mathbf{k}_1,\mathbf{k}_2) = \frac{\langle n_{\pi^-}\rangle^2}{\langle n_{\pi^-}(n_{\pi^-} - 1)\rangle} \frac{\sigma_{\pi^-}\dfrac{d^6\sigma(\pi^-\pi^-)}{d^3k_1 d^3k_2}}{\dfrac{d^3\sigma(\pi^-)}{d^3k_1}\dfrac{d^3\sigma(\pi^-)}{d^3k_2}}$$

where:

σ_{π^-} is the total π^- production cross section,

$\dfrac{d^6\sigma(\pi^-\pi^-)}{d^3k_1 d^3k_2}$ is the double pion inclusive cross section,

$$\frac{d^3\sigma(\pi^-)}{d^3k_i} \text{ are the single pion inclusive cross sections,}$$

and $<n_{\pi^-}>^2$ and $< n_{\pi^-}(n_{\pi^-} - 1)>$ are the first and second binomial moments of the π^- multiplicity distribution. The term which multiplies the ratio of the cross sections above is due to the normalization of the double and single pion inclusive cross sections:

$$\int \frac{d^6\sigma(\pi^- \pi^-)}{d^3k_1 d^3k_2} d^3k_1 d^3k_2 = < n_{\pi^-}(n_{\pi^-} - 1)> \sigma_{\pi^-}$$

$$\int \frac{d^3\sigma(\pi^-)}{d^3k_1} d^3k_1 = <n_{\pi^-}> \sigma_{\pi^-}$$

This gives the correlation function the value of one if there is no correlation in the pions.

While the above expression gives an exact definition to the correlation function it is not the function which is actually fit to the data. Experimentally one extracts a quantity which is the pion pair distribution as a function of q and q_0, or some other parameters related to the pions separation in phase space, for pairs in which one expects to see the enhancement in the distribution due to the Bose statistics, and divides this by the same distribution for pion pairs in which one expects all effects *except* that due to the Bose statistics.

For clarity, let $A(q,q_0)$ represent the distribution of pion pairs in which the effect of the Bose - Einstein statistics is expected to manifest itself. I'll refer to these pairs as correlated pion pairs. These correlated pairs are formed by making all possible combinations of two negative pions from within a given event. Let $B(q,q_0)$ represent the distribution of pion pairs where one expects all effects present in $A(q,q_0)$, other than that due to Bose - Einstein statistics, to be present. I'll refer to these pion pairs which are used to build the distribution $B(q,q_0)$ as uncorrelated pairs. The two pion correlation function is then given as:

$$C_2(q,q_0) = \frac{A(q,q_0)}{B(q,q_0)}$$

The question is thus, how does one construct this background distribution? I'll describe briefly four ways that $B(q,q_0)$ may be extracted.

1.) If one has both positive and negative pions within one's detector acceptance the pairs could be formed combining a positive and negative pion in each pair. While the pairs formed with this technique would not exhibit the effect of the Bose - Einstein statistics, there are a few other problems which one would have to contend with. The positive and negative pions may be created through different processes, any Coulomb effects between the pions themselves and between the pions and nucleons will be opposite for the two types of pions, and unless one has a truly 4π acceptance, the effect of a different acceptance for the two types of pions will have to be understood and corrected for.

2.) One could construct a model for the pion production and form the background pairs using the negative pions which come out of a monte - carlo program. The problems with this technique are numerous. First of all, the result is obviously model dependent. If your model doesn't populate phase space in the same fashion as the real data you obtain a dubious result. One also has all the problems associated with correctly including all the acceptance effects and biases of the experimental detection and analysis.

3.) A technique which has been used by some high energy physics groups is to mix the various components of the pion's vector momentum from the same event in the actual data and then use these "new" pions to form the background pairs. One of the motivations for this method is that one does a fairly good job of preserving overall momentum and energy conservation.

4.) The last technique I'll describe is the one which is employed in this analysis. It is the technique most commonly known as *event mixing*. With this scheme one forms the uncorrelated background pairs by mixing pions from different events. It's clear that with this method all the hardware and software acceptances are automatically correctly taken care of, i.e. one can only use negative pions which have come out of the analysis. The greatest care that must be taken when using this method is that one use as close to the same type of events as possible in forming the correlated and uncorrelated pairs. As will be explained in

complete detail in the section on the pion correlation analysis, care has been taken to use exactly the same pions in both the correlated and uncorrelated pion pairs.

What may seem at first to be a problem with this method, namely the conservation of energy, momentum, charge, and various conserved quantum numbers turns out not to be of concern in RHIC. The reason is that the two colliding nuclei supply a large reservoir of energy and quantum numbers of which the detected pions are but a small portion. An idea of the size of this reservoir can be obtained by calculating the maximum number of pions which may be created with the colliding system that we used for most of this experiment, i.e. 1.8 GeV/n Argon on KCl.

$$E_{cm} = \sqrt{P_1 + P_2} \qquad (P_1, P_2 \text{ are 4 vectors})$$

$$= [\,(E_1 + E_2)^2 - (p_1 + p_2)^2]^{1/2}$$

in the lab frame, with m_2 at rest:

$$= [\,(E_1 + m_2)^2 - \mathbf{p}_1^2]^{1/2}$$

$$= [\,m_1^2 + m_2^2 + 2E_{1lab}m_2]^{1/2}$$

$$E_{cm} = 104.45 \text{ GeV}$$

$$E_{cm} - 2M_{Ar} \approx 30 \text{ GeV}$$

$$\text{Maximum \# of pions} \approx \frac{30}{.1396} \approx 215 \text{ pions} / 3 \approx 70\ \pi^-$$

A more probable number of negative pions is about 15 or so. In the events which are used in the analysis our mean detected π^- multiplicity is just over two, thus we do not expect any significant kinematic correlations to affect our results.

W.A. Zajc[31] has pointed out that one may end up with a correlation in the background distribution $B(q,q_0)$ due to one's limited experimental acceptance, and has proposed a technique to correct for this effect. I only mention this point here for completeness. This background correlation is taken up in detail in the section on the systematic corrections to the pion correlation analysis

I'll close this section with a few general remarks that may alleviate some common questions which some may have about particle correlation studies. The first point is that while most processes that are measured in nuclear experiments are the results of, and explained in terms of, either kinematics or dynamics, the basis of particle correlations is *neither*. The bunching in phase space which one investigates in these studies is due solely to the quantum statistics which apply for the particular particles being studied[27]. Any correlations due to kinematics or dynamics represent the noise in these analyses, which one hopes to understand and correct for.

The other point which may lead to confusion is the analogy that is always made between the correlations of photons used by Hanbury - Brown and Twiss to measure stellar radii, and the correlations, in this case of negative pions, used to get some measure of the spatial and temporal extent of a nuclear collision. As pointed out by G. Cocconi[23], whereas in the case of the photons the interference develops primarily in the region of the telescopes used to detect the photons, far away from their source, in the pion interferometry case the interference develops near the source, as soon as the pions undergo their last rescattering and leave the nuclear fireball.

Chapter 2. Experimental Apparatus

HISS

This experiment was performed using the Heavy Ion Spectrometer System[8] (HISS) which is located in beam line #42 at the Lawrence Berkeley Laboratory's BEVALAC. The HISS facility was designed in a modular fashion to allow one to configure its array of detectors to run a wide variety of experiments.

The heart of the HISS facility is the large superconducting dipole magnet. The HISS magnet has pole tips which are 2.1 meters in diameter separated by a 1 meter gap. It has a maximum central field strength of 3 Tesla, and is mounted on a rotating base.

Experimental Setup

The HISS configuration used for this experiment is shown in figure #2.1 on the next page. I'll briefly describe the set-up here, and then discuss in detail each detector in the experiment. The beam from the BEVALAC comes down the evacuated beam line to the HISS experimental cave as shown at the top of figure #2.1. It impinges onto a soft-collimator, monitor scintillator arrangement (S_1 and V_1 in figure), also in vacuum, which collimates the beam and sets all the timing in the trigger. The beam continues down the beam pipe, through a dipole (B42m3) and three quadrapole (Q3A, B, C) magnets. The beam leaves vacuum at the exit of Q3C and traverses P_1, about 2.5 m of air, and P2. P_1 and P2 are position sensitive scintillation detectors which give the upstream vector for the beam. The beam then goes through another soft-collimator, scintillator arrangement and enters the vacuum chamber of the HISS superconducting dipole. For this experiment the magnetic field of the HISS dipole is pointing down (into the page). The beam then strikes the target located just off-center in the HISS magnet. Any surviving beam or projectile fragments

Figure #2.1 Experimental Setup

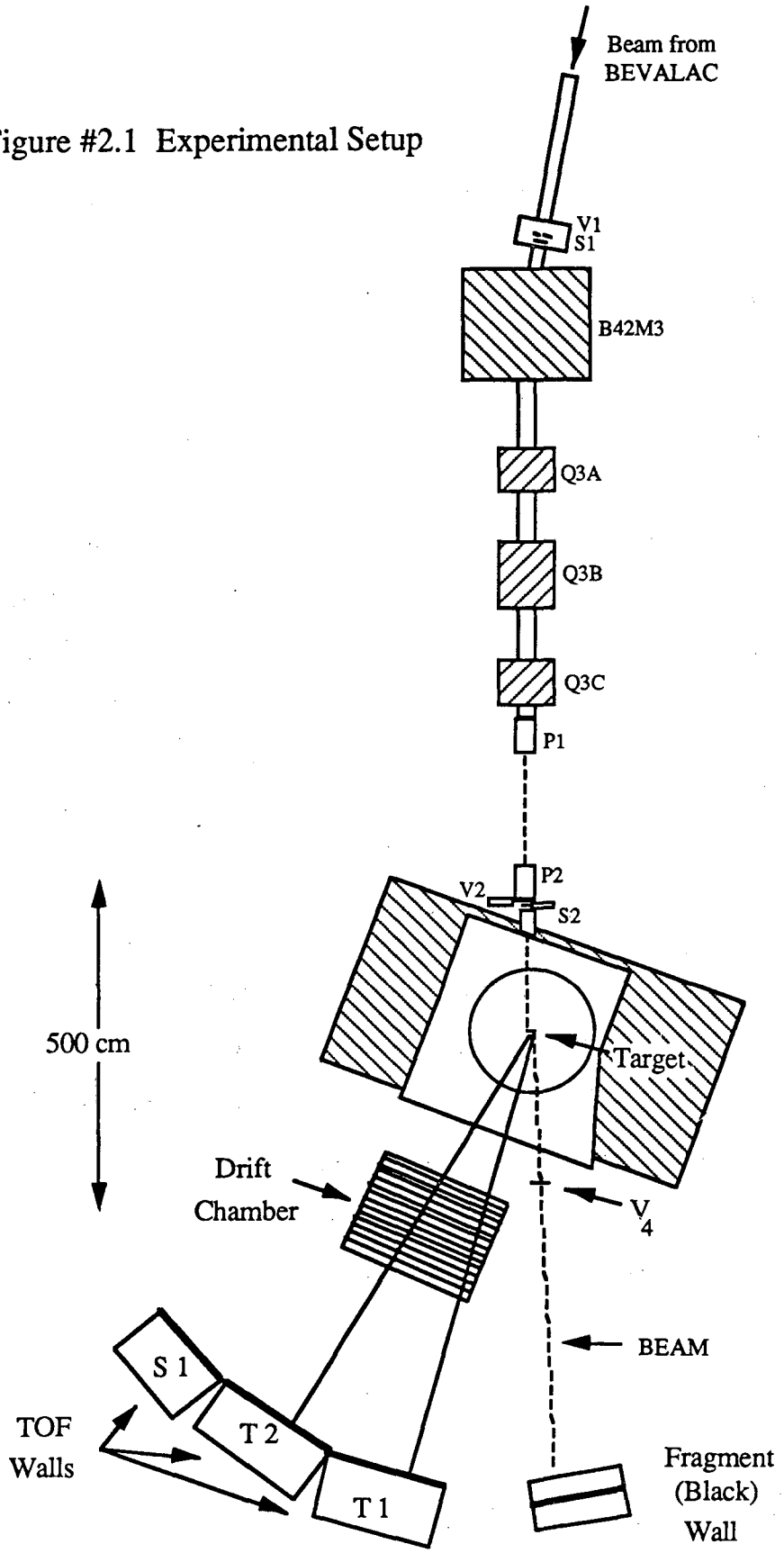

then leave the vacuum chamber, strike the trigger detector (V4), and finally, register in the Fragment wall (following the dotted line in figure). The negatively charged pions (produced around 0° in the center-of-mass (cm)) and light positively charged particles and nuclei (≈ 90° in the cm) travel through the HISS drift chambers and strike the arc of Time-of-Flight (TOF) walls as shown in the figure. The upstream beam vector obtained from the PLUTO detectors and the downstream vectors for the pions obtained from the Drift Chamber are used to determine the pions momentum.

Upstream Detectors

V_1 Soft Collimator

The first detector encountered by an incoming beam particle was a soft collimator which we dubbed V_1. This detector consists of a 1/4" thick piece of plastic scintillator with a one inch diameter hole through it. The scintillator was read out, on one end only, with a 2" photomultiplier tube. V_1 was located 13.1 meters upstream from the center of the HISS dipole, just before the start scintillator described below. The signal from V_1 was incorporated into the trigger as a veto.

Start Scintillator

The start scintillator, which set all the timing for the trigger and other electronics was located 13 meters upstream from the center of the HISS dipole. It was what we refer to at HISS as a MICKEY detector. It consisted of a five cm by five cm , one mm thick plastic scintillator oriented at an angle of ≈ 45° with respect to the beam. The casing of the MICKEY consists of an aluminum , 10 cm cube, with 6 cm diameter holes in five of the sides. The beam passes into and out of the cube through two of the opposing holes. The other two opposing holes are used to mount 2" photomultiplier tubes, at 90° with respect to the beam, which collect the light from the scintillator (see figure).

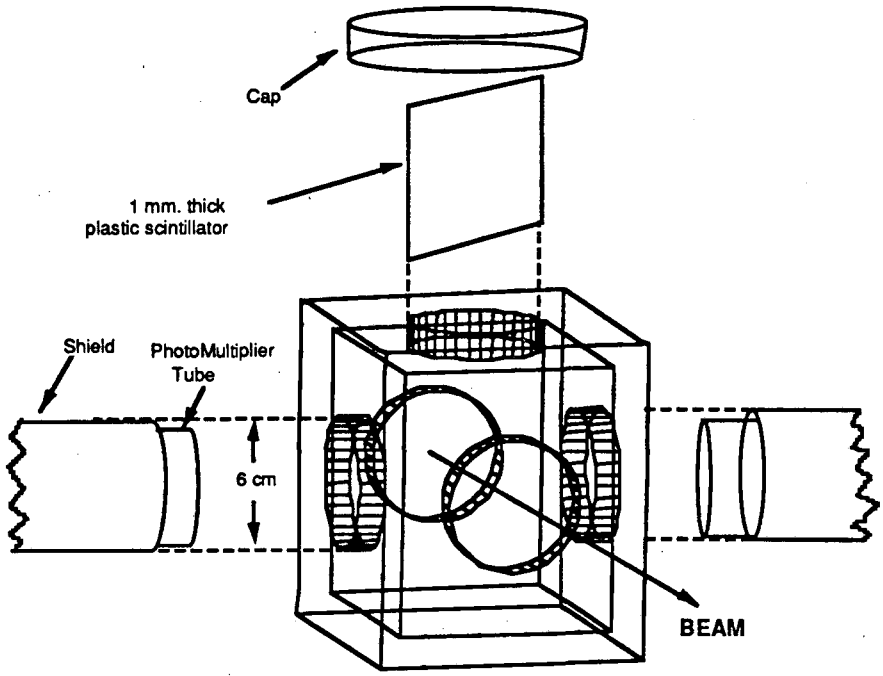

Figure # 2.2 Exploded view of MICKEY detector.

All the timing of the trigger and other electronics is set by the signal from one of the phototubes. In E684H we used the right phototube, as viewed looking along, and in the direction of, the beam.We collected both an ADC and a TDC signal from each tube. The TDC signal for the right tube was split in the cave with one signal patched into the counting house on a short (130 m) 90 Ω cable to use in the trigger.

The resolution we achieved with the MICKEY detector is summarized in the table below.

MICKEY RESOLUTIONS				
Beam	σ_{S1R} ADC % of <ADC>	σ_{S1L} ADC	$\sigma\sqrt{S1R*S1L}$	σ_{S1L} TDC (ps)
1.8 GeV*A Argon	8.2 %	7.0%	5.8%	100
1.2 GeV*A Xenon	9.2%	9.4%	5.2%	70

Table #2.1 MICKEY Resolutions

Vectoring and Beam ID

The next detectors encountered by the beam following the MICKEY detector were what we refer to at HISS as PLUTO detectors. A PLUTO is a position sensitive scintillation detector. We used two PLUTO's to extract the upstream vector and charge ID for the beam, and to monitor the focus of the beamline.

A PLUTO (figure #2.3) detector consists of a piece of plastic scintillator, oriented perpendicular to the beam, which is viewed face-on by four air coupled photomultiplier tubes located towards the top, bottom, left, and right of the center of the scintillator. The position information is derived from the ratios of the pulse heights observed by these four photomultiplier tubes. The detector also contains two scintillating fiber grids, oriented at 90° with respect to one another, coupled directly to two additional photomultiplier tubes. These fiber grids are used to calibrate the positional response of the device (See figure below). In this experiment the scintillator we used was 1 mm thick and the fibers used in the grid had a circular cross section with a diameter of 1.0 mm for one of the detectors and 0.5 mm for the other.

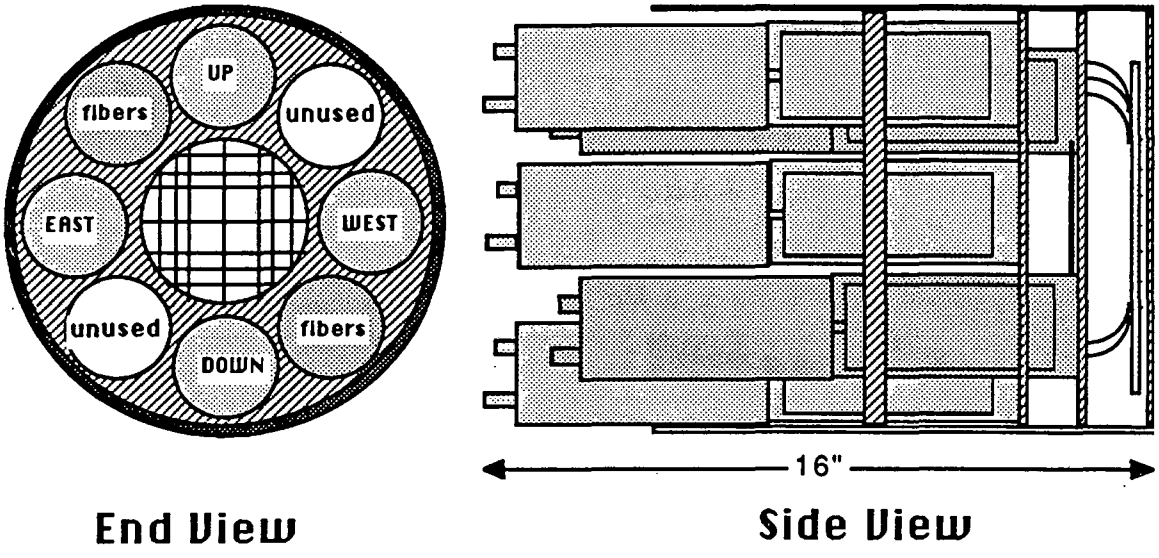

Figure# 2.3 Diagram of PLUTO detector.

The procedure used to calibrate the positional response of the PLUTO detectors was the following:

1.) Select events in which one of the fibers was hit (by requiring a valid ADC value.in one of the photomultiplier tubes attached to the fibers).

2.) Extract a subset of these events which pass a cut on the fourth root of the product of the ADC values from the top, bottom, left, and right tubes, thus selecting those events which were due only to the primary Argon(or Xenon) beam.

3.) Plotting the natural log of the ratio of the ADC values for the top and bottom tubes versus the same quantity for the left and right tubes. This plot yields a distorted picture of the fiber grid.

4.) For each rectangular region of the fiber grid in the plot, the values of the axes (ln(U/D), ln(L/R)) were extracted from the plot and assigned their known X and Y values.

5.) These values were put into the following equations for all four corners of a given region.

$$x_{ij} = a_i + b_i * \ln(L_{ij}/R_{ij}) + c_i * \ln(U_{ij}/D_{ij}) + d_i * \ln(L_{ij}/R_{ij}) * \ln(U_{ij}/D_{ij})$$

$$y_{ij} = e_i + f_i * \ln(L_{ij}/R_{ij}) + g_i * \ln(U_{ij}/D_{ij}) + h_i * \ln(L_{ij}/R_{ij}) * \ln(U_{ij}/D_{ij})$$

Where i = region #

j = corner #

This yields eight equations for eight unknowns in each region of the fiber grid which were solved via Cramer's rule.

The resulting plot of X versus Y is shown in the plot below.The arc on the left side of the plot is a consequence of the soft collimator V2. The sharp break on the right is the limit of the calibration coefficients.

This process was done, and calibration coefficients were extracted, for each of the primary beams used in this experiment.

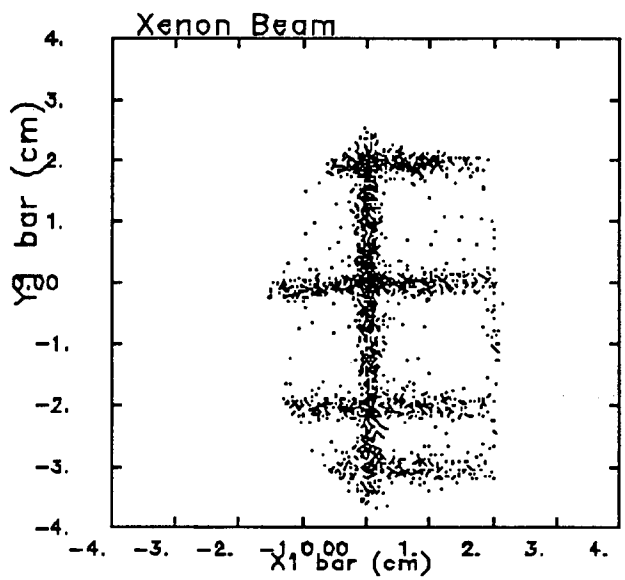

Figure #2.4 Calibrated X-Y for events in which Fiber Grid was hit.

The best value for the beam's position is derived by incorporating the focus of the beam with the positions returned by the two PLUTO detectors. As a consequence of the beam's focus there is a tight correlation between X_1 (X value from PLUTO#1) and X_2, and, similarly, Y_1 and Y_2. By fitting a straight line to the plot of X_1 versus X_2 one extracts an equation for X_1 as a function of X_2. The best value for, say X_1, is what I'll call $\overline{X_1}$. $\overline{X_1}$ is the average of X_1 as determined by PLUTO#1, and by X_2, via the X_1-X_2 correlation. When I refer to the position resolution of the PLUTO's, I'll be referring to the width of the distribution of what I define as ΔX. This ΔX is the difference between X_1 and $\overline{X_1}$. In the figures below I show the distribution of ΔX_1 and ΔY_1 for the Xenon beam.

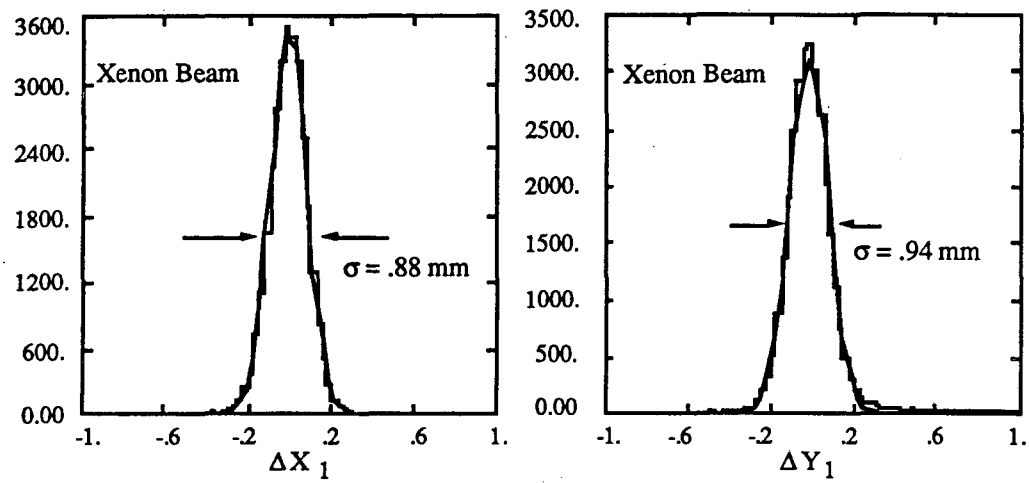

Figure #2.5 Histograms of ΔX1 and ΔY1. σ's are from gaussian fit.

In the table below I've summarized the resolutions observed for the PLUTO detectors in this experiment. The values shown for the pulse height resolution refer to the width of the distribution of the fourth-root of the product of the ADC values from the left, right, top, and bottom photomultiplier tubes of a given PLUTO.

PLUTO Resolutions			
Beam	$\sigma_{\Delta x}$ (mm)	$\sigma_{\Delta y}$ (mm)	$\sigma\sqrt[4]{LRUD}$ ADC
1.8 GeV*A Argon	1.9	1.9	6.2%
1.2 GeV*A Xenon	.88	.94	3.4%

Table #2.2 PLUTO resolutions.

The number attached to the PLUTO detectors refers to the order in which they're encountered by the incoming beam. PLUTO #1 was located 481.33 cm, and PLUTO #2 was 226.53 cm upstream of the center of the HISS dipole. Given the position resolutions of the PLUTO detectors from the table above, one may calculate the angular resolution for the upstream beam vector via the following equation:

$$\sigma_{\theta_x}\,(\text{rad}) = \frac{\sqrt{2}\,\sigma_{\Delta x}}{D}$$

where D = 254.8 cm = distance between the PLUTOs

Putting the observed position resolutions into the equation above yields:

$$\sigma_{\theta_x} = \sigma_{\theta_y} = 1.05 \text{ (mrad)} \quad \text{for Argon}$$

$$\sigma_{\theta_y} \approx \sigma_{\theta_x} = 0.49 \text{ (mrad)} \quad \text{for Xenon}$$

Using the position and angle resolutions above one may calculate the position resolution at the target for the two beams. In this experiment the target was located 3.4 cm to the left of the center of the HISS dipole as viewed by an incoming beam nuclei.

$$\sigma_{x_t} = 3.3 \text{ mm} \quad \text{for Argon}$$

$$= 1.5 \text{ mm} \quad \text{for Xenon}$$

S2-V2 Beam Definition Counters

The last set of detectors which the beam encounters before entering the HISS dipole vacuum chamber consist of two plastic scintillators, V_2 and S_2. V_2 was a rectangular piece of quarter inch thick, plastic scintillator, large enough to cover the entire beam envelope as well as S_2.

There was a five cm diameter hole in V_2 and it was read out on one end via a photomultiplier tube. S_2 was a rectangular piece of half mm thick, plastic scintillator, placed just downstream from V_2, and slightly larger than the hole in V_2. S_2 was also read out on one end via a photomultiplier tube. This is a similar arrangement to V_1 and S_1 discussed earlier. By putting the discriminator signal from V_2 into the trigger as a veto, and requiring the analog signal from S_2 to fall within a gate as a requirement of the trigger, one selects, preferentially, "clean" beam tracks.

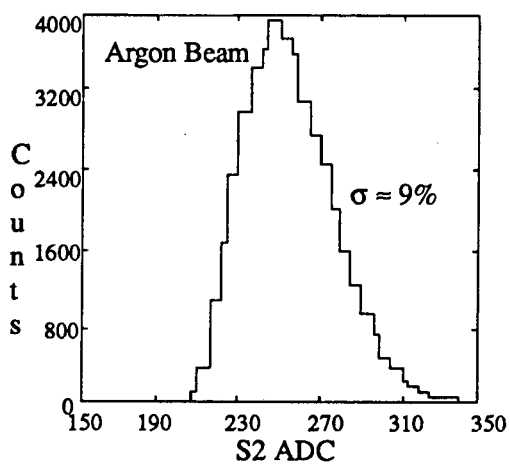

Figure #2.6 Histogram of S_2 ADC.

Target Wheel

All of the targets used in this experiment were mounted on a target wheel inside the HISS dipole scattering chamber. The target wheel itself consisted of a circular piece of quarter inch aluminum, eighteen inches in diameter. There were eight holes, each three and three quarters inches in diameter, spaced evenly around the perimeter of the wheel. (see figure).

We were able to select any of the eight target positions via a remote control in the HISS counting house. The remote control operated an electric motor placed in the cave but outside of the scattering chamber. The motor rotated a shaft, which went into the HISS scattering (vacuum) chamber through a Wilson seal, and rotated the target wheel. The target wheel assembly was mounted on a track, placed perpendicular to the beam's direction, which allowed us to do the final positioning of the target assembly in the beam. This adjustment was done via a hand operated crank which passed into the vacuum tank in the same manner as the motorized crank.

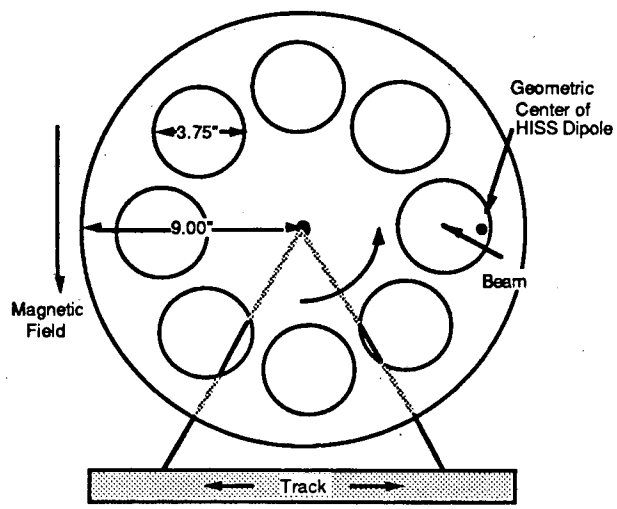

Figure #2.7 Target Wheel.

We determined the final target adjustment in the following way. There is a plexiglass port on the upstream side of the vacuum chamber which allows one to see the target wheel assembly inside. We placed a magnetically shielded video camera such that we could see the target on a TV monitor in the counting house. In one of the target positions on the wheel we placed a piece of phosphor coated glass. By using high flux beam spills we could see the spot on the monitor where the glow of phosphorus caused by the beam appeared. We would then draw a circle around this spot on the monitor screen. By then

sending someone into the cave to shine a flashlight on the target wheel, the person viewing the monitor could determine the relative position of the center of the hole holding the phosphorus, and the beam. We then adjust the target wheel assembly along its track and iterate the procedure until the beam is passing through the center of the hole.

Downstream Detectors

The downstream detectors can be split into two groups. Those in the beam rigidity region, which detect primarily beam velocity projectile fragments, and those which see the negatively charged particles (π^-) emitted close to zero degrees in the center of mass (cm) system along with the light positively charged particles and nuclei emitted at about ninety degrees in the cm system. I'll describe the ones in the beam rigidity region first.

V4 Trigger Scintillator

The detector which we dubbed V4 is the one which determined the centrality of the events which the trigger circuit accepted. It consisted of a 50 cm by 30 cm rectangle of 3 mm thick Pilot 425 plastic Cherenkov radiator. We choose to use a Cherenkov radiator to avoid the saturation in the light output which one observes in plastic scintillators for highly charged fragments. The radiator was read out at both ends via adiabatic plastic light pipe by two inch photomultiplier tubes. This scintillator was mounted just downstream of the HISS vacuum chamber such that the beam spot was centered on the detectors active area. It was mounted with the long dimension vertical, 235.0 cm downstream from the center of the HISS dipole, on a radial line 6° to the left of the 0° line, as seen looking downstream.

One of the analog signals on each tube was patched into the counting house on a short (≈ 100 m) 90 Ω cable for use in the trigger and the other was patched in on long (275 m) 50 Ω cables for input to ADCs.

Black Time of Flight Wall

Downstream from V4 was what I'll refer to as the Black wall. The name comes from the black plastic membrane used to wrap the scintillator slats in the wall. The Black

wall consists of fifteen individually wrapped plastic scintillator slats. Each slat is 89.5 cm long, 10 cm wide, and 6 mm thick. The slats are mounted vertically, long edge to long edge, in a plane, on an aluminum frame. The frame's height is such that the beam (which is 8 feet high in the HISS cave) strikes the center of the slats. On each end of each slat there is attached a tapered plastic light pipe which goes to a 2 inch photomultiplier tube.We collected TDC and ADC information from each end of each slat in the data stream.

The Black wall was incorporated into the experiment to give information on the charge sum of any surviving projectile fragments, and hence give us some means of estimating the impact parameter.

The gains of the phototubes were calibrated at the start of the experiment by using the HISS magnet to sweep the Argon beam across the wall while adjusting the voltages of the phototubes such that the ADC signals of all the tubes were approximately equal. To extract the charge calibration of the Black wall we collected some data with a thick ($\approx$ 3 cm) target placed just upstream of the HISS magnet. This gave a beam of fragments from charge 18 (Argon) down on the Black Wall. The charge calibration can then be read off of the plot of $\sqrt{V_4\ ADC\ hi^2 + lo^2}$ vs $\sqrt{ADC\ hi*lo}$ for the Black wall. With the gains we used for the Black wall one may extract the charge of the projectile fragments down to about charge four. Below this point the ADC values are into the noise.

HISS Drift Chamber

The downstream tracking was done using the HISS Drift Chamber[9] (DC). The overall dimensions of the DC , as seen by a track, are 1.5 m vertically, 2.0 m horizontally, and 1.4 m deep. The detector consists of fifteen modular planes of drift cells. The planes are separated from one another by ten cm along a line normal to the front plane of the DC., and are all contained in the same gas volume. The planes have one of three types of wire orientation, vertical, and tilted to the left or right of vertical by 30°. We define these orientations as S, T, and U, respectively. Defining a prime to denote a 1 cm horizontal offset, the plane orientations are T', S', U', S, T, S, U, S', T, S', U, S, T', S, U' (see figure).

The combination of distributing the planes along the track, and the fringe field from the HISS dipole, help to reduce the number of wires which fire from the delta rays produced when a highly charged projectile fragment traverses the chamber. The distributed planes also lead to better position and angle resolution.

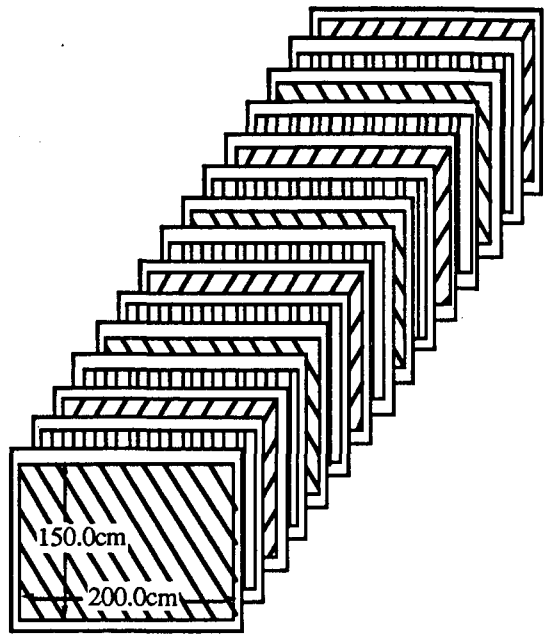

Figure #2.8 Wire orientations of HISS Drift Chamber.

Each plane contains from 100 to 120 drift cells, depending on its wire orientation. Each cell consists of a 1 cm by 2 cm rectangular array of field shaping wires with a sense wire at its center (see figure).In E684h we ran the Drift Chamber with the wires labeled V_3 at -2000 Volts, those labeled V_2 at -1800 volts, and those labeled V_1 at -1600 volts. All the field shaping wires are 75 micron diameter Cu-Be. The anode wire (S in figure) is kept at ground and is 20 micron gold plated tungsten. There are ground wires between each of the planes of the DC to isolate the electric fields. The resulting equipotentials for this configuration, operated at the voltages specified above, are also shown in the figure. The difference between the equipotential lines shown is 40 volts.

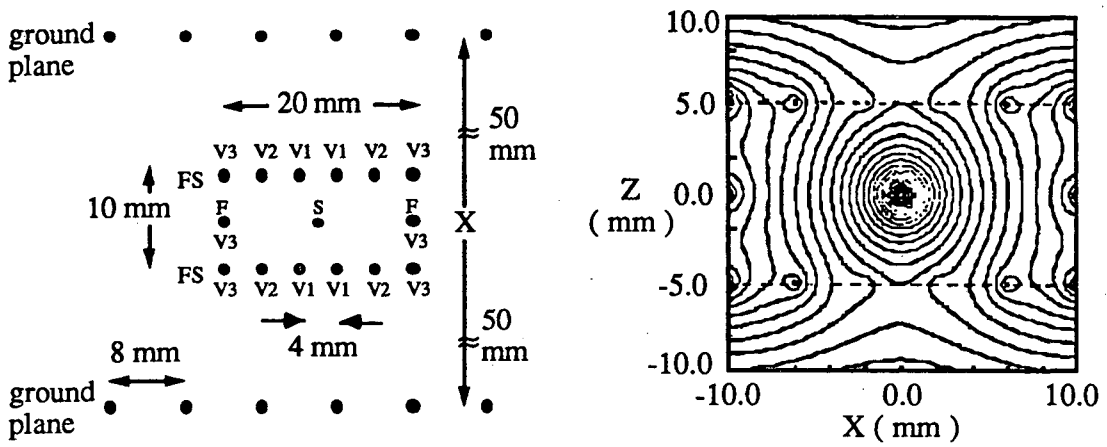

Figure #2.9 Geometry of Drift Cell and associated equipotential lines.

The windows at the entrance and exit of the DC consist of two sheets of 50 micron Mylar separated by a 3 cm gap. Nitrogen gas is purged though the gap. The counting gas we used in the DC was P-10 (90% Argon, 10% CH_4).

The single plane efficiency of the chambers during our run was approximately (within ≈ 1%) 100%. The single plane position resolution and the efficiency of finding spatially close tracks is discussed in the section on the tracking software.

An ADC and a TDC is acquired for each sense wire. The ADCs are necessary to determine which cell was hit by the primary track and which cells in a plane were hit by delta rays (knock-on electrons) when a highly charged nucleus traverses the DC. The ADCs were not necessary in this experiment as the only particles which passed through the DC were the singly charged negative pions and light (up to about Z = 3) mid-rapidity positive particles and nuclei. The discriminators on the front end cards of the DC are Constant Fraction Discriminators (CFD). There are set such that they trigger when a threshold is passed which corresponds to 80% of the maximum pulse height for this cell for this event.

Time of Flight Walls

Downstream from the Drift Chamber we positioned three Time-of Flight (TOF) walls. The information from the TOF walls allows one to extract the velocity, and hence the mass, of the particles for which we get tracks from the Drift Chamber. The TOF walls were laid out on an arc about the center of the HISS dipole. The radius of the arc was approximately 7.5 m. The arc of the TOF walls covered the angles from about 10° to about 55° in the lab as shown in figure 2.1.

The TOF walls labeled T1 and T2 consist of twenty slats each. Each slat is 10 cm wide, 300 cm tall, and 2.5 cm thick. There is a plastic, tapered light pipe attached to each end of the slats which is coupled onto 2 inch photomultiplier tubes. From each tube we collect both ADC and TDC information.

The TOF wall labeled S1 differs from the description above only in the length of the slats and the number. It consists of fifteen slats, each 200 cm long.

Targets and Beams

We used two targets and two beams in this experiment, they are specified in the tables below.

Beam	Z	A	β	γ	K.E. (MeV/A)	P (GeV/c)
Argon	18	40	.94011	2.9336	1799	102.663
Xenon	54	136	.8969	2.261	1175	256.726

Table #2.3 Beams Used. Note β, γ, K.E., and P are values at target.

Target	Thickness (g/cm^2)	L_R (g/cm^2)	θ_0 (mrad)
KCl	1.130	18.5	4.2
La	.446	7.8	5.0

Table #2.4 Targets.

The values listed above for the beam parameters β, γ, K.E., and P are the values at the target after correcting for material upstream in the beamline. The values given for the multiple Coulomb scattering(MCS) (θ_0) are calculated for a pion with a lab momentum of 600 MeV/c which traverses half of the target thickness. The effect of this MCS on the overall momentum resolution for the pions is discussed is the section on the momentum reconstruction and resolution. The column labeled L_R gives the radiation lengths of the target materials.

The beam energies used are the maximum available from the BEVALAC for each beam. The target thicknesses were chosen to give a sufficient data rate while keeping the multiple Coulomb scattering and energy loss in the target tolerable.

Triggers and Data Set

The trigger logic for this experiment was wired up using all the usual discriminator, gate generator, fan in-out, logic (OR, AND, etc.), modules as well as a LeCroy 4508 Programmable Logic Unit (PLU). The way the PLU works is that one plugs into it the relevant logic signals from one's trigger counters, all timed so that they overlap for some period of time (say 10 nsec.), and then give it a strobe signal during this overlap time period telling it to read the logic values (on or off) for the input signals. The PLU then uses a downloaded program which contains the various combinations of these input logic signals which one wants satisfied before the PLU puts out a logic signal on the appropriate output. The PLU model we used had two sets of eight inputs and eight outputs. The same eight trigger counter logic signals were put into each set of inputs. One set of eight outputs was used for the various trigger outputs and the other set of outputs merely passed through the input signals. To change the trigger with this setup merely requires one to move the cable which goes from the PLU to the event accept logic (EAL) module between the eight trigger logic outputs. The sixteen outputs were also put into a coincidence register module and read out in the data stream with the event.

In the following sections I'll describe the trigger outputs we used and show the selection criteria each one put on the events accepted.

Beam Upstream (BU) $\equiv S_1 * \overline{V_1}$

This trigger was the minimum requirement we placed on any of the events which were accepted. The requirement is that both sides of scintillator S_1 have output signals larger than their discriminator thresholds, and the soft collimator (hole scintillator) V_1 has a signal less than its discriminator threshold.

There is a circuit wired into the signal from the AND gate of S_{1r} and S_{1l} which is used to veto events where the beam particle being triggered on was preceded by another particle down the beam pipe by 500 nsec or less, and sets a flag if the beam particle is followed by another particle down the beam pipe within a set period of time. The circuit works as follows. When either the S_1 scintillator or V_1 scintillator is struck such that they put out a signal large enough to fire its discriminator, a logic signal is sent to an UpDating One Shot (UDOS) module. The UDOS module has the following characteristics. It stays in its relaxed, OFF, state until it receives a logic signal. When it receives a signal it goes into an ON state and puts out a logic signal for 520 nsec. If, at any time within this 520 nsec it receives another input signal it resets its clock so that it remains on for 520 nsec after the last signal is received. After a small delay ($\approx$ 20 nsec) this signal is put into a logic module as a veto along with the signal from the AND of S_{1r} and S_{1l}. The output of this module goes into the PLU as S_1. Therefore if the beam particle being considered by the trigger has been preceded by another particle within $\approx$ 500 nsec, the PLU doesn't receive a signal for S_1 and doesn't put out a trigger.

The followed flag works in the following way. Once the trigger being used has been satisfied, a logic signal is taken from the "event accepted" fan-out and converted into a long signal (100's of nsec). This signal is then put into an AND gate along with the signal from the OR of S_{1r} and V_1. If S_1 or V_1 fire within the time that the followed signal is on, a bit is set and a scalar is incremented.

Beam Straight (BS) ≡ $S_1 * \overline{V_1} * S_2 * \overline{V_2}$

The next trigger output used was what we designated as the Beam trigger. In addition to satisfying the previous trigger it required the discriminator for S_2 to fire and the one for the hole scintillator V_2 not to fire. The threshold on S_2's discriminator was set at a level just below the signal for the beam, thus eliminating beam tracks which interact in the vacuum window at the end of the beam pipe, either PLUTO detector, or the ≈ 3 m of air upstream of S_2. This high threshold is the reason for the asymmetric pulse height distribution seen for S_2 in figure #2.6.

Figure #2.10, to the right, shows a scatterplot of the squareroot of the product of the ADCs from the top and bottom tubes for V_4 versus the maximum charge seen by the Black Wall (Z_{max}) for this trigger. The points in the plot which lie in the vertical group below the beam spot correspond to beam nuclei which fragment in the air (≈ 5.5 m) between V_4 and the Black Wall. The points which lie in the near diagonal set of points in the plot are due to beam nuclei which fragment between S_2 and V_4.

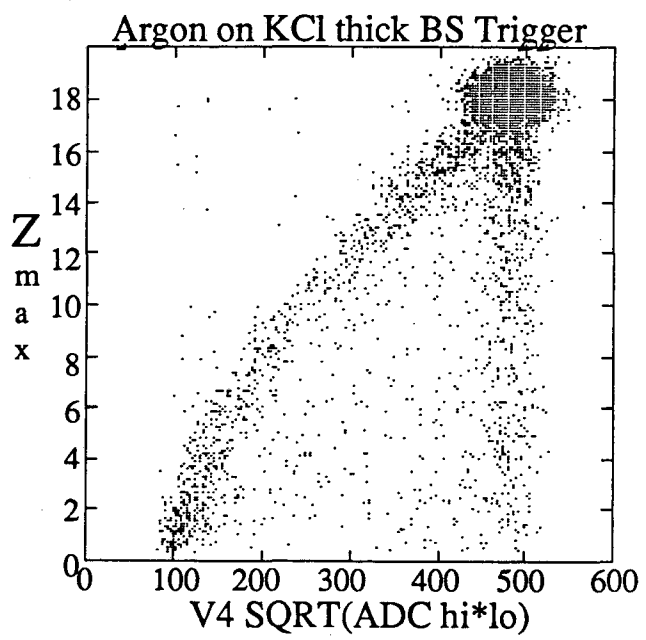

Figure #2.10 Beam Trigger.

Streamer Chamber Soft (SCS) ≡ Beam * $\overline{V_4}$ hi

The reason for the name given this trigger is historical. This trigger is very similar to the trigger used by some members of the collaboration earlier to select central (small impact parameter) events in pion studies using the Streamer Chamber detector at the

BEVALAC. Recall that V4 is a rectangular piece (50 cm x 30 cm) of Pilot 425 Cherenkov radiator, read out by photomultiplier tubes at both ends.

It's positioned just downstream of the HISS vacuum tank, and subtends the beam and heavy projectile fragments. Figure #2.11 shows a plot of the square root of the product of the ADCs for V4 versus the maximum charge seen in the Black Wall for this trigger. As stated explicitly in the section heading above, the trigger required the BS trigger as well as the lack of a signal from the discriminator connected to the upper tube on V4. The beam and target for the data shown in the plot are Argon and KCl thick, respectively. Notice that this trigger corresponds to a cutoff in projectile fragment

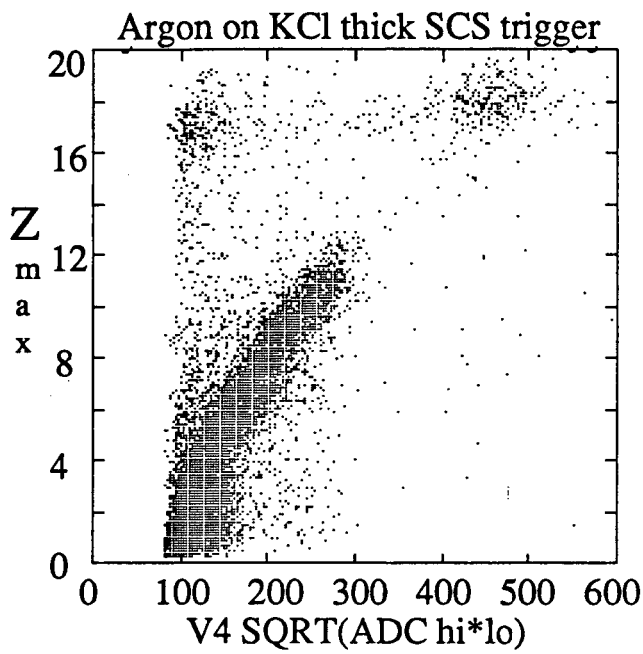

Figure #2.11 V4 vs Z_{max} for SCS trigger.

charge at about Z = 11 or 12. The sparse set of points on the plot which shows up as charge eighteen is from events in which the beam particle that satisfied the trigger was followed down the beam pipe by another beam particle. These followed events are eliminated using software cuts in the analysis. Figure #2.12

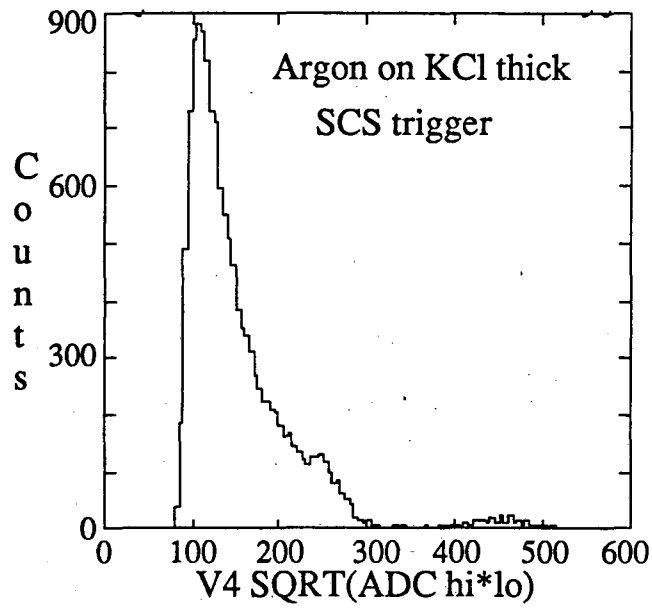

Figure #2.12 Projection onto V4 for SCS trigger.

shows the projection of the data in figure #2.11 onto the X axis.

Using the ratio of SCS to BS triggers, corrected for the dead time and the target out ratio, one may calculate the cross section for satisfying the SCS trigger by inverting the attenuation equation as shown below:

$$N(\overline{SCS}) = N(BS)e^{-\sigma t} = N(BS) - N(SCS)$$

$$\rightarrow \frac{-\ln\left(1 - \frac{N(SCS)}{N(BS)}\right)}{t} = \sigma_{scs}$$

$$\text{where } t = \frac{\#\text{ of target nuclei}}{cm^2}$$

Plugging in the value of t for the thick KCl target and the appropriate value for the ratio from the scalars gives:

$$\sigma_{scs} = 1.404 \text{ (barn)}$$

One may compare this to the geometric cross section calculated with the equation:

$$\sigma_{geometric} = \pi r_0^2 (A_1^{\frac{1}{3}} + A_2^{\frac{1}{3}})^2$$

where A_1 and A_2 are the atomic #s of the projectile and target and $r_0 = 1.2$ fm. Plugging in the values for Argon on KCl gives a geometric cross section of 2.116 barn. Making the comparison one finds:

$$\sigma_{SCS} \approx 66\% \text{ of } \sigma_{geometric}$$

Streamer Chamber Hard (SCH) ≡ Beam * $\overline{V_4}$ lo

This trigger was set to select central events. The differences between this SCH trigger and the SCS trigger of the previous section is that the veto signal came from a discriminator connected to the photomultiplier tube on the bottom of V_4, the voltage of this tube and hence its gain was higher than the top tube used in SCS, and the discriminator threshold was set much lower. Figure #2.13 shows the square root of the product of the ADCs from the top and bottom of V4 versus the maximum charge seen in the Black Wall for data taken with this trigger. The figure also shows the projections of this data onto the X and Y axis, respectively. Notice that for the bulk of the data which passes this trigger the leading charge is less than four. The data in these plots is for the Argon beam on the thick (1.13 g/cm^2) KCl target.

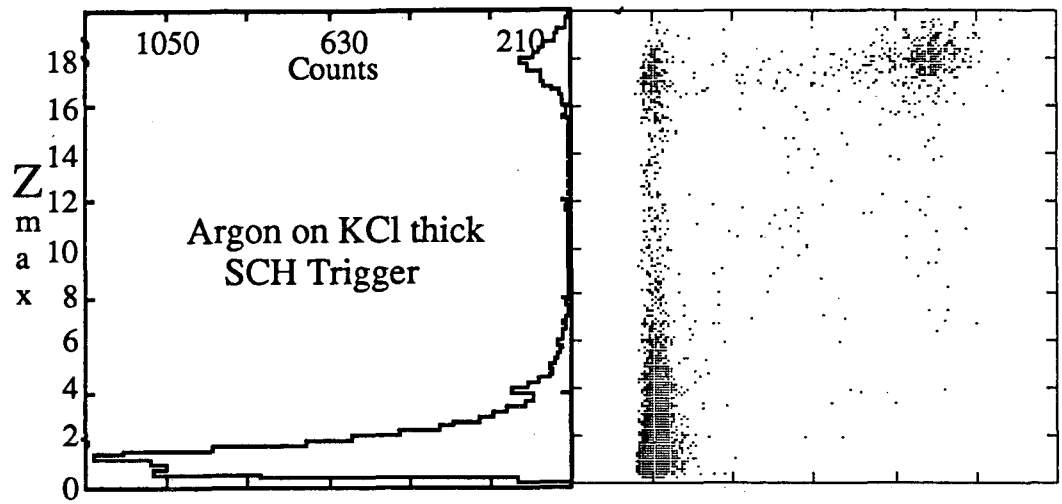

Figure #2.13 V4 vs Zmax and projections for SCH.

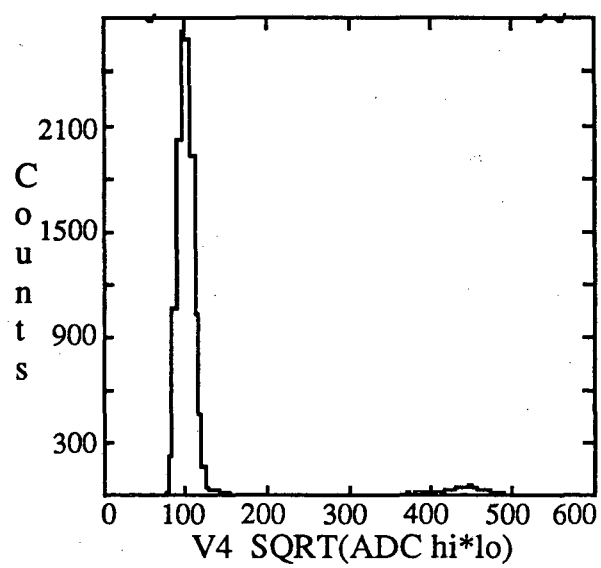

As was done for the SCS trigger, using the dead time and target out corrected values for the ratio of the SCH to BS triggers, and the known parameters for the targets, one may calculate the cross section for the SCH trigger for the beam-target combinations used in this experiment.

In table #2.5 I've summarized these cross sections for the beams, targets, and triggers used in this analysis.

Beam	Target	σ_{geo}	σ_{scs} (barn)	$\sigma_{scs}/\sigma_{geo}$ %	σ_{sch} (barn)	$\sigma_{sch}/\sigma_{geo}$ %
Argon	KCl thick	2.116	1.428	67	0.555	26
Argon	La	3.346	2.438	73	1.358	40
Xenon	La	4.856	3.844	80	1.75	37

Table #2.5 Summary of triggers.

Chapter 3. Analysis

The analysis is performed in four passes through the data. I'll begin this chapter with a brief description of what is accomplished in these four passes and then proceed to describe each pass in detail.

The main task in the first pass through the data is to construct the tracks in the Drift Chamber from the wire hits (wires within an event which receive a valid TDC value). In addition a slight compression of the data is achieved by doing some zero suppression in the Time of Flight (TOF) wall data.

In the second pass through the data the tracks in the Drift Chamber and the incoming beam vector are used to reconstruct the pions momentum.

In the third pass the correlated pion pairs (those formed using pions from the same event) and uncorrelated pion pairs (those formed using pions from different events) are formed and placed into matrices. All the systematic corrections to be applied (Gamow, background correlations, DC efficiency, etc) are calculated and applied to the uncorrelated pairs.

In the fourth pass the multidimensional fitting is performed on the matrices to obtain the best fit to the correlation function and hence extract the spatial (R, or $R_{\perp}$ and $R_{//}$), temporal (τ), and "chaoticity" (λ) fit parameters.

Before preceding with the description of the first pass I'll briefly describe the computers and the analysis shell used for this analysis.

Computers

The data acquisition program was run on a Digital Equipment Corporation (DEC) VAX 750. It read out the data from CAMAC via a Microprogrammable Branch Driver (MBD) and wrote it onto 1600 bpi magnetic tape.

The analysis was started using the HISS VAX 780 and transfered onto a cluster of DEC VS2000 workstations and a DEC 3500 file server.

Analysis Shell LULU

The analysis shell which was used to do all the online and offline analysis is called LULU[35]. It was originally written by Henry Crawford and Peter Lindstrom, from the Space Sciences Lab and Lawrence Berkeley Lab respectively. The primary motivation in writing the shell was that it would be flexible so that it could be easily adapted to the myriad possible configurations of detectors and types of analyses at HISS. LULU contains a graphics package as well as automatic data statistics. It allows users to easily insert subroutines which I'll refer to from now on as analyzers. It also allows run time functions to be defined and applied to the data using Reverse Polish Notation (RPN). Probably the strongest criteria was that LULU had to allow for variable word length events.

LULU allows great flexibility in how one analyzes data. It can process raw data and save the output as scatter plot or histogram files, save a new raw data file for those events which pass some user specified criteria, or save the output of one or more of the analyzers in a fashion which may be read back into LULU for further analysis. These features were used extensively in this analysis.

The data is passed sequentially through the analyzers on an event by event basis. The data from an analyzer is specified as some maximum number of groups, each group containing some specified number of words. An example of this grouping is the Time 0f Flight wall analyzer where a group is put out for each scintillator slat which has a valid ADC or TDC for either the top or bottom tube. The group then contains the ADCs and TDCs for both tubes as well as some quantities calculated from these ADCs and TDCs. The number of groups varies event by event depending on how many slats register a valid hit.

LULU allows for a variety of cuts. Event cuts may be put on which only pass the data onto selected (selected via flags set at run time) subsequent analyzers which pass some requirement or cut. Group cuts may be put on which pass only those groups into scatter

plots which pass some cut, and cuts may be put on which select on a group by group basis which points are passed into an actual plot.

First Pass, Tracking

The first pass through the data was the most computer intensive. The output from this pass consists of four saved analyzer outputs. There are no cuts of any sort applied to the data in this pass. After briefly discussing the output of these analyzers I've included a rather extensive discussion of the Drift Chamber tracking software. Following this is a section on the performance of the tracking software in finding pairs of tracks. The extent of detail included on the tracking software and performance is mandated by its direct effect on our ability to do the pion correlation analysis.

The first analyzer saves all the information from the upstream detectors and V4. The X and Y positions of the beam at the two PLUTO detectors is also calculated and saved.

The second saved analyzer output contains both TDCs and ADCs for any slat in any of the TOF walls (Black, T1, T2, S1) which had at least one valid ADC or TDC.

The third saved analyzer contains the necessary information for all the "good" tracks from the tracking analyzer as well as some summary information from the tracker for every event. "Good" here is defined as those tracks for which the tracker found both an X component and an associated Y component.

The fourth saved analyzer contains all the information from the scalars. The size of the files which contain these saved analyzer outputs are about 65% of the raw data files. I'll refer to the files saved in this first pass as "S files".

Drift Chamber Tracking Software

To assist the reader in following the description of the DC tracking software I'll repeatedly refer to the flow chart for the Drift Chamber tracking software, figure #3.1.The numbers of the subheadings in the following section refer to the bubbles in the Flow Chart.

1. Input

The input to the tracker comes from a separate analyzer (#5). This previous analyzer reads in a map file which translates between the TDC and ADC addresses in the raw DC data and the associated plane and wire numbers in the DC. It then loops through the data and assigns plane and wire numbers to all TDCs and ADCs which appear. It also fills an array which indicates whether the wire registered only a TDC, only an ADC, or both, and whether this wire has the largest ADC value for all wires in its plane of the DC. This wire data is then passed into the tracker.

2. Initialization

The following initialization is done only on the first call to the tracker. First a data file is read in which contains the geometry of the DC. A loop is entered over plane number which assigns to each plane its wire orientation and any left-right spatial offset. A nested loop runs over all the wires in the plane, calculates their positions and stores this information into an array.

3. Load Pointer array

In this stage a loop is entered over all the planes with a nested loop over all the wires within the plane. Each wire is checked and only those which have both an ADC and a valid TDC (valid ≡ non zero and less than overflow value) are passed. For each of these passed wires a drift distance is assigned to the TDC value from a lookup table (Space-time curve, read in as data file), and a counter is incremented to keep track of the number of valid wires in the event. This wire number is then entered into the pointer array and the pointer array is updated. This two dimensional (wire # and plane #) pointer array is filled such that all array values for wire numbers less than the valid one being entered are set equal to the current valid wire number until the next lower valid wire number is reached. This array is used in the subsequent tree search routines.

4. Start Tree Search for S Candidates.

The logic of the tracking software is such that it first finds what I'll refer to as S candidates. An S candidate is a track which is constructed using only the vertical wire (S)

planes and thus can be completely specified with a horizontal position (x) and angle (θ_X). On the first pass through this part of the tracker (bubble #4 on Flow Chart (FC)) a search is made for S candidates which contain wires from either six or seven S planes (recall that there are seven S planes in all). On subsequent passes the number of S planes required to define an S candidate will be reduced.

It starts by selecting two S planes which I'll refer to as planes #1 and #2 These plane #'s as used here do not correspond to the first two S planes in the DC. The two plane numbers are the first two entries in the first combination of S plane numbers, from a list of several such combinations whose use will be explained later.

Referring to the FC we now move to the right to bubble 4a. The first valid wire is obtained for plane #1 from the pointer array. The range of wires to look through for plane #2 is calculated as a function of the perpendicular distance between the planes and a maximum horizontal angle parameter specified via a data statement. To start, the hit in plane #1 is assumed to be to the left of the first valid wire and its position is calculated from the wire position and the drift distance associated with the wire.

4b. Next the first valid wire within the allowed range is obtained for plane #2 from the pointer array(If there is no valid wire within the range the program returns to bubble 4a and selects the next valid wire in plane #1). To start it's assumed that the hit is to the left of the wire and its position is calculated. Using these two x (horizontal) and z (depth into chamber) positions an angle and position (x, θ_X) are calculated for the line which connects them.

A loop is then entered which goes over the remaining five s planes from the combination used above to select planes 1 and 2. For each plane the predicted position of the track is calculated. The corresponding wire # for the plane is then calculated. The program then looks one half cell (1 cm) to the left of the predicted position, in the predicted half cell, and one half cell to the right, for a hit in this plane. If there is no hit it goes on to check the next plane. If it finds one or more hits within these three half-cells it selects the

one which is closest to the predicted position. If the absolute difference between the predicted position and the hit in this plane is less than or equal to a variable cutoff, in this analysis 3 mm, then this new point is used, along with any other points already associated with this candidate, to calculate a new x-θ_x. A chi-square is then calculated using these points and the line defined by this new x-θ_x. If this Chi-square is less than a threshold value for the number of points in the Chi-square calculation, then this new wire hit is designated as belonging to this S candidate. The program then proceeds to check in the next plane.

Once this loop over the other five planes is completed a check is made to see how many wires were associated with this S candidate. If there are more than the minimum number set for this pass a code is calculated for this candidate. This code is calculated by multiplying the plane #, wire#, and pointer for which side of the wire is used, by different numbers. The code is set up so that candidates which differ in any of the above parameters (plane#, wire #, or side pointer) always get assigned distinct codes, and vice-versa. A check is made at this point to see if this candidate has been found in a previous pass. If this is a new candidate a number of arrays are updated with the information about this track and the S candidate counter is incremented.

The program then loops back up to bubble 4a following the path shown as loop #2 in the flow chart. If a candidate was not found on the previous pass a pointer is toggled to try the same procedure as described above assuming the hit is on the right side of the first valid wire in plane #1. If there was a candidate found, or if both sides of the wire in plane #1 have already been used, the program moves onto the next valid wire in plane #1 and repeats the process. The program continues to follow this procedure, in loop #2, until all valid wires have been tried in plane #1.

At this point the program loops back to bubble #4 along the loop designated as loop #1 in the flow chart. At bubble # 4 the decision is made whether to select a different

combination of S planes, and hence a different selection for planes #1 and 2, and move off to the right along loop#1 to repeat the tree search, or to move on to bubble #5.

It's here that the reason for the different combinations of S planes becomes clear. If you're looking only for seven plane S candidates you only need one combination of planes and one selection of planes #1 and 2, as all S planes must have a hit for all tracks. If you're after 6 planes S candidates as well you must use at least two different combinations of S planes to get all the possible combinations of six planes out of seven. (the second combination differs in both planes #1 and 2) From the combinatorics one finds that it takes a minimum of three combinations (each having distinct planes #1 and 2) to get all the possible five plane S candidates. To find all the possible 4 plane S candidates, which is the minimum number of S planes allowed at this point in the tracker, takes seven different combinations of the S plane numbers. The logic of the tracking software is such that in this first round of tree searching it looks for only six and seven plane S candidates, and thus it goes around the loop labeled #1 in the flow chart twice, using two different combinations of planes #1 and 2, before passing on to bubble #5.

5. How Many Distinct

When the program arrives at this point it has some number of S candidates. The question now is how many of these candidates are actually distinct tracks. The minimum number of times the tracker goes through the tree search (loop #1) is twice, thus it's possible at this point to have found the same track twice if the two tracks differ by as little as which side of a wire is used in the track (otherwise the code check would have already determined that the second track had already been found). Whether all the S candidates are distinct is determined by how close they are in x at the back of the DC and how close they are in angle (θ_x). The program loops over the candidates with a nested loop over all the other candidates. First the check is made on position. If the distance between the tracks is equal to or less than ten mm, a check is made on the difference in the angles. If, also, the angles differ by 12 mr or less, these tracks are determined to be non-distinct. To decide

which one to keep, the tracker looks at the number of planes in each of the tracks, keeping the one with the most planes. If they both have the same number of planes it looks at the Chi-square for the two tracks, keeping the one with the smallest. Finally, if they both have identical numbers of planes and identical Chi-squares, it keeps the first of the candidates encountered in the loop. The tracker than updates the arrays which contain the S candidate track information, keeping only the data for the distinct candidates.

It's at this point that wires are first actually removed from the pointer array and hence become inaccessible for use in any subsequent tree searches. The wires used in the set of distinct S candidates are now removed from the pointer array.

I determined the values to use in the checks above (10 mm, 12 mr) by looking at the S candidates found by the tree search in the actual experimental data. By plotting such things as the number of shared wires as a function of the separation in x and θx it was clear where to put these cutoffs. Note that if the tracker incorrectly identifies a track as being non-distinct, it does not necessarily mean that this track is lost. Unless this misidentified track either shares too many wires with another track, or is found on the last pass through bubbles 4, 5, and 6 (pass which searches for S candidates with at least four S planes), it will be found again on the next pass.

6. Eliminate Shared Wires.

To this point there has been nothing in the code to guarantee that a given wire is not used more than once. This could happen with S plane wires if two S candidates either cross, or come within two cm of each other, within the DC. The tracker makes no effort to try to determine which candidate these shared wires best belong to. It removes the shared wires from all candidates where it appears. If a wire is deleted from a candidate, all the necessary arrays are updated, and the tracker keeps track of how many wires were originally associated with the candidate. This original number of wires will be used later by the tracker to prioritize the S candidates and to calculate the number of shared wires in the event.

This elimination of the shared S wires at this stage is particularly important in an analysis where the relevant quantities are associated with the relative positions of the tracks. If one were to leave in these ambiguous shared wires at this point there could be systematic distortions introduced for the low relative momentum pairs.

Referring to the flow chart, at this point the tracker moves to the left and follows loop #3 back up to the start of the S candidate tree search. On the first pass through bubbles 4, 5, and 6 the tracker was searching for the six and seven plane S candidates. On the second pass it looks for S candidates with at least five planes, and on the third pass for those with at least four planes.

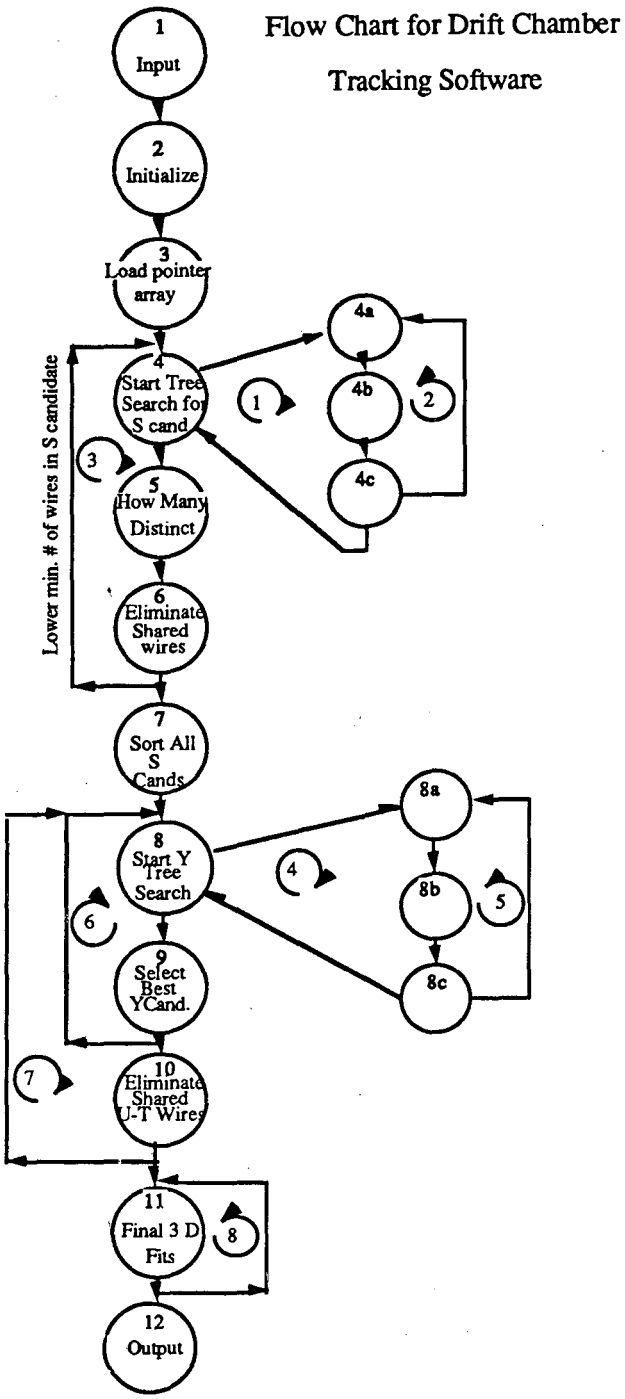

Figure #3.1 Flow Chart for Drift Chamber Tracking Software.

7. Sort S candidates.

At this point the tracker has completed the S candidate tree searching and has found all the S candidates with four or more S planes associated with them. A sorting loop is

entered which orders the S candidates from those with the largest original number of S planes to those with the least. This ordering of candidate numbers is saved into an array and used in the next stage of the tracker to prioritize the search for matching Y candidates.

8. Start Tree Search for Y Candidates.

On entering this part of the tracker the minimum number of T-U planes necessary for a possible Y candidate is set . For this analysis I set this parameter to four (recall that there are eight T-U planes in all). The tracker selects the first S candidate from the array ordered on the number of original S planes in the candidates. It then checks to see that this S candidate has at least three S planes remaining in it and had at least four originally. If not the program goes and gets the next S candidate from the ordered array. If the S candidate passes this check a loop is entered over the T-U planes with a nested loop over the wires in these planes. For each valid wire the y position is calculated for the intersection of the vertical plane containing the S candidate and the wire, and these values are loaded into an array.

The tracker then selects the first of a number of combinations of the T-U plane numbers. This is analogous to what was done in the S tree search earlier. It selects the first two entries in this list, defines them as planes #1 and 2, and, referring to the flow chart, moves off to the right along the loop labeled #4. The pass through bubbles # 8a, b, and c and loop #5 is the same as the pass through bubbles 4a, b, and c and loop #2 described previously, with the exception of three differences.The first is that when the tracker compares the predicted value for the track candidate with the value seen by one of the planes it makes the comparison in a coordinate system where the wires in the plane are parallel to one of the axes. The second and third differences are in the tolerances. Whereas in the S tree search a plane passed onto the Chi-square test if the difference between the predicted and actual positions in a plane was less than or equal to 3 mm, here it passes the plane on if the difference is less than or equal to 12 mm. The third difference is that the maximum Chi-square allowed for a given number of points, below which a plane is

determined to be associated with the T-U candidate, is four times higher than the corresponding Chi-square value used in the S tree search.

When the tracker has tried all the wires in plane #1 for this combination of T-U plane numbers it returns to bubble #8 along loop #4 (analogous to loop #1 in S tree search). It then selects the next combination of T-U plane numbers (and hence new planes #1 and 2) and goes back to the right along loop #4 to repeat the process. It turns out from the combinatorics that the tracker must make ten different selections of U-T plane number combinations to ensure finding all Y candidates with four or more planes.

9. Select Best Y Candidate.

Having finished the Y tree search for this particular S candidate the tracker moves down to bubble #9 with what may be a large number of possible Y candidates. The decision is made on which of these possible Y candidates to choose by looking first at how many planes are associated with each one, selecting the one with the most planes. If there are more than one candidate with this number of planes it selects the one with the smallest Chi-square. If there are two or more of these candidates which have the most planes and have equal Chi-squares then the tracker selects the first one it encountered.

A number of arrays are updated and this best Y candidate is now associated with this particular S candidate.

At this point the tracker loops back up along loop #6 and checks to see if the next S candidate had the same number of S planes originally associated with it as the previous one. If so, it proceeds through the Y tree search and the selection of the best Y candidate for this new S candidate. If not, the tracker proceeds down to bubble #10.

10. Eliminate Shared U-T Wires.

As was done for the shared S wires, the tracker makes no attempt to determine which track the shared (and hence ambiguous) wire best fits. It merely searches through this set of Y candidates, which all are associated with S candidates which had equal numbers of S wires originally, and eliminates any shared T-U wires from all Y candidates

in which it appears. It then updates a number of arrays and keeps track of how many T-U wires were originally associated with each Y candidate.

The tracker now eliminates all the T-U wires used in these Y candidates from the pointer array.

At this point the tracker loops back up to bubble #8 along the loop labeled #7 in the Flow Chart. It repeats this Y candidate procedure for all the S candidates which had the next lower # of S planes originally associated with them, finding the best Y candidate for each one (if it exists), eliminating the shared T-U wires, eliminating the wires from the pointer array, and going on to the next set of S candidates, until it gets to the end of the S candidates. The tracker now has a list of S candidates, some with associated Y candidates, and all the wires associated with each track.

11. Final Three Dimensional Fits.

The tracker now goes into a loop over all the S candidates. The order in which the S candidates are selected is gotten from the ordered array loaded earlier, going from those which had the most S planes associated with them originally, to those with the least.

Having selected an S candidate, the tracker checks to see if it has an associated Y candidate which has at least three remaining U-T planes associated with it. If the S candidate does not pass this check, but has at least three remaining S planes associated with it (out of the minimum original number of at least four), then an output group is loaded for this S candidate and a counter is incremented to keep track of the number of these unmatched S candidates.

If the S candidate does have a good Y candidate then this track is passed into the three dimensional track fitting routine. This routine loops through all the wires (both S and U-T) associated with this track and calculates x and z coordinates for each S wire hit and x, y, and z for each U-T wire hit. It then performs the three dimensional fit and calculates the Chi-square for these points with the new fit.

The routine then loops through the wires in the track once again and checks to see if the drift distance for the wire was less than one mm. If it finds one of these close hits to a wire it checks to see if a better fit is obtained by refitting the track with this hit placed on the other side of the wire. If so it updates the necessary arrays before proceeding.

The tracker now enters a loop over the wires in this track once again to calculate the residuals for each plane. These residuals are the difference between the position of the track in a given plane as calculated from the plane offset, wire #, and drift time, and the position predicted in the plane from the fit track using all the other planes associated with this track except the given plane. When the tracker has finished all these fits it fills an output group with all the necessary information about this track.

Referring to the Flow Chart, the tracker now moves back up along the loop labeled #8, selects the next S candidate, and repeats the final fitting procedure. It continues in this fashion until it reaches the end of the S candidates.

12. Output.

At this point there are only a few summary quantities to calculate to get the final output. The tracker uses a Real Time Library routine to keep track of how much time is spent in the S tree search part, the Y tree search part, and the entire tracking routine. These values are calculated and put into the output. The other summary item calculated is the number of shared S and U-T wires in the event. These summary quantities are placed into the first output group and the tracker is finished with the event.

Figure #3.2 shows a plot of CPU time versus the number of good (both X and Y component) tracks for the tracking software. The CPU time is for a VAX 780.

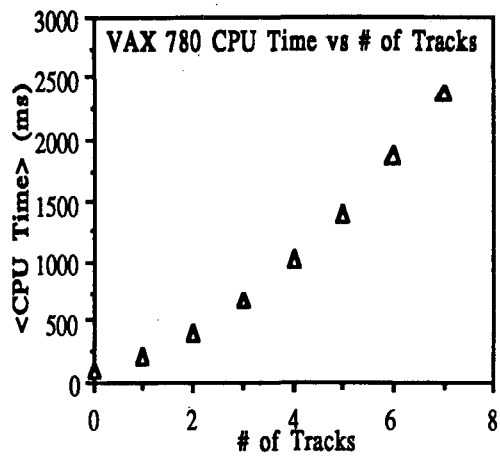

Figure #3.2 CPU time versus # of tracks for tracking software.

Calibration and Single Plane Position Resolution

The two calibrations which were required for the Drift Chamber in this analysis were the horizontal plane offsets and the Space-Time curve (relation between TDC value and drift time). I started the calibrations using a space-time curve from a test run with a proton beam, and merely changed the offset (TDC value which corresponds to zero drift distance).

The horizontal plane offsets are calibrated by looking at the plot of the residuals for each plane. Recall that these residuals are the difference between the position in a plane as determined by the fit track using all planes except the one in question, and as determined using the horizontal offset for the plane, the position of the hit wire in the plane, and the drift distance. The procedure I used was an iterative one in which I'd process a number of events and make histograms of the residuals for each plane. I would then calculate a new set of offsets for the planes by looking at the mean values for the residuals. When the offsets are correct the mean residual for a plane should be zero. This is not a large correction. The largest adjustment made to an offset was 550 μm and the average adjustment was ≈ 150 μm.

Once these offsets are adjusted one may check the space-time curve. To do this I processed a large number of tracks and plotted the position in the drift cell (-10 to +10 mm) for a given plane, as determined from the fit track using all planes except the one used for the plot, vs the TDC value (TDC channels correspond to 1 nsec) for the plane. This leads to the characteristic sawtooth type distribution shown in figure #3.3. I then bin the position into, for example, half mm bins, and for each bin extract the average TDC value. The plot of this average TDC value for a bin versus the position for the midpoint of this bin is then your space-time curve. To get the lookup table to be used by the tracking software one simply does a straight line interpolation between points in the space-time curve. I went through this procedure using various planes and various bin sizes. My results agreed within uncertainties with the space-time curve from the test run and I ended up using this previously extracted space-time curve in the analysis.

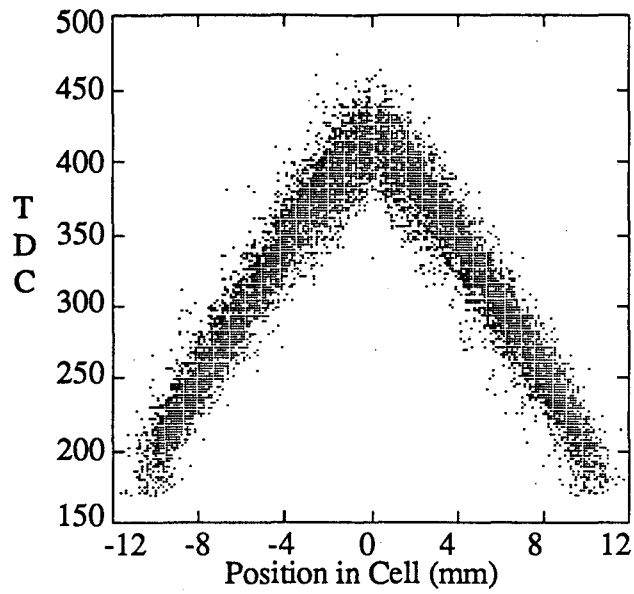

Figure #3.3 Position in Drift Cell vs TDC

With these two calibrations complete one may now extract the single plane position resolution of the Drift Chamber for this data set. This position resolution is the width of the distributions of residuals which were used to adjust the horizontal offsets. The average position resolution for the vertical wire planes is ≈ 670 μm and ≈ 900 μm for the U-T planes. Figure #3.4 shows a typical distribution for a vertical wire plane.

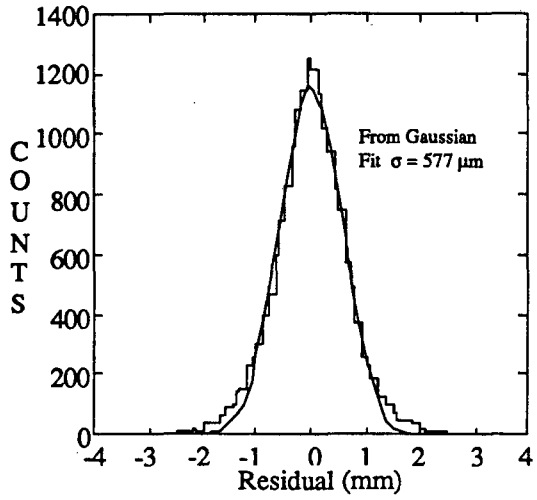

Figure #3.4 Single Plane Position Resolution

Performance of Tracking Software

It's crucial when one does a two (or multiple) - particle correlation analysis that one understands and characterizes the efficiency of the tracking detectors and software for finding close tracks within an event. As a consequence, quite a bit of time and effort has gone into developing the software to extract this efficiency function.

The code which extracts this efficiency function interfaces with the tracking software via the raw wire hit arrays which are normally loaded by the analyzer which precedes the tracker. As discussed previously (Input to tracker) these wire hit arrays are passed into the tracking routines via common blocks. The basic idea is as follows. I first select a number of events for which the tracker returns one and only one good track, and I save the raw data for these events into a file. The LULU reads one of these single track events and loads the wire hit array using the same subroutines as the analysis code. These arrays are passed into the tracking software, also in the same fashion as the analysis code. Some additional constraints are placed on the single track events which are passed on from this point on the total number of wires in the event and the number of wires in the event not

used in the track. These cuts are adjusted, depending on the multiplicity of the events I wish to construct, so that the final distributions of the number of wires, and the number of wires not used or shared, in the concatenated events have approximately the same means and widths as the distributions of these same quantities in the actual data. The single track is then passed into the momentum reconstruction routine (described in the section on second pass through data). The information about the single track from the tracker and momentum reconstruction routine is retained, and the wire hit arrays are copied into holding arrays. The program then reads in the next event from the file of single track events and continues this process until enough tracks have been accumulated to construct the multiplicity event desired. The program then clears the normal wire hit arrays which at this point still hold the information from the last event processed.

At this point a loop is entered over the single tracks, with a nested loop over all the hit wires in the event,which has a nested loop over the wires in all the other loaded events. A check is made for each wire to see if it is used in more than one event. If the wire is used only once it is put into the normal wire hit array used by the tracker.

If the wire is used in more than one event the program goes into the following procedure to mock-up the way in which the Constant Fraction Discriminators (CFD) used on the front-end cards of the Drift Chamber would respond. It first determines which of the events that used this wire has the largest ADC value associated with it. It then looks through these events which use the wire again to see if any of them have an ADC value for the wire which is 80% or more of the largest ADC. If so, the TDC value for the event which satisfies this condition and is closest to the wire (highest TDC) is put into the wire hit array for this wire. Otherwise the TDC value for the wire with the largest ADC is entered into the array. Finally, if none of the events which use this wire has an ADC value for the wire, the TDC value for the track closest to the wire is entered into the array. The ADC value entered into the wire hit array for this wire is the sum of the ADC values for all events which used the wire.

The tracking efficiency program continues in this fashion until all the wires used in all the single track events have been checked and loaded into the wire hit arrays. The arrays are then passed into the tracker in the same fashion as in the analysis code. The output of the tracker is then passed into the momentum reconstruction routines in the same way as in the analysis code.

The efficiency analyzer now has all the information for the tracks which were used to build the concatenated event (x, θ_x, y, θ_y, p_x, p_y, p_z, E, # of planes, etc) as well as all the information for the tracks which were found by the tracker in the event. The program then forms all possible pairs of input tracks and all possible pairs of output tracks. For each pair it calculates a number of quantities including the sum of the differences in the coordinate x at the entrance and the exit of the Drift Chamber (I'll call this DX), the same quantity for the coordinate y (DY), the same quantity for the spatial distance (DLo), the difference in all components of momentum, the number of planes in each track, etc. It also matches each track found in the concatenated event with its closest counterpart from the input tracks.

For clarity:

Let X1f = horizontal position of track #1 in pair at front of Drift Chamber

X1b = horizontal position of track #1 in pair at back of Drift Chamber

X2f = horizontal position of track #2 in pair at front of Drift Chamber

X2b = horizontal position of track #2 in pair at back of Drift Chamber

Ditto for Y or vertical positions

Then
$$DX = \sqrt{(X_{1f} - X_{2f})^2 + (X_{1b} - X_{2b})^2}$$
$$DY = \sqrt{(Y_{1f} - Y_{2f})^2 + (Y_{1b} - Y_{2b})^2}$$
$$DLo = \sqrt{DX^2 + DY^2}$$

One may use the output from this efficiency analyzer to generate efficiency functions using any output quantity one wishes as the independent variable and for any track multiplicity. This is done in the following way. One processes a large number of these concatenated events and saves the output of the efficiency analyzer. One then makes a

histogram of some quantity, for example DX, for all the pairs found by the tracker in the concatenated events and the same histogram for all the pairs put into the events. Dividing the histogram of DX for the output pairs by that for the input pairs yields the efficiency function.

I've looked at these efficiency curves as functions of the difference in the total momentum for the pairs (DP), the transverse momentum (DP_t), the individual components of momentum (DP_x, DP_y, Dp_z), the spatial separation of the tracks (DLo), and the two components of the spatial separation (DX, DY).

As a consequence of the large acceptance in momentum and energy of our experimental setup, and the small rest mass of the pions, the efficiency curves as a function of any of the momentum differences were essentially flat for the pions. By looking at the efficiency as a function of DLo, DX, and DY, and in particular looking at the scatter plot of tracks found as a function of DX and DY, I arrived at the following conclusions. For spatially very close tracks the efficiency is a rapidly changing function of the separation, DLo. Above a certain value of DLo ($\approx$ 100 mm) the efficiency loses its dependence on the separation in the Y (vertical) direction and becomes a function of the X (horizontal) separation alone. I looked at the effect of the multiplicity on the efficiency in the range from two to six tracks. Increasing the multiplicity changes the normalization of the curve but does not have much effect on its shape.

In figure #3.5 I've plotted the pair efficiency for the Drift Chamber and tracking software as a function of DX. The curves in the plot are the absolute efficiency for finding pairs in multiplicity two and six events as well as the renormalized curve for the multiplicity six events (normalized to have same value as multiplicity two curve when both reach efficiency plateau). This efficiency function will be used when I generate the uncorrelated, background spectrum of pion pairs which are used in the fitting of the HBT parameters. The affect on the final values of the HBT parameters will be seen to be minor.

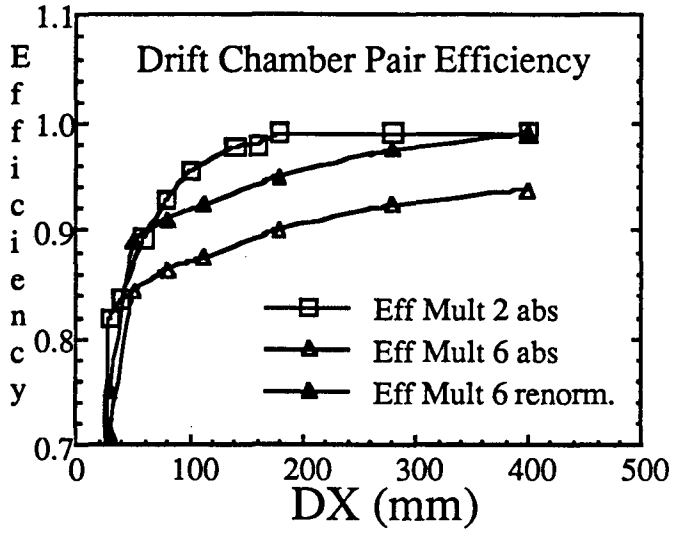

Figure #3.5 Drift Chamber Efficiency.

Second Pass, Momentum Reconstruction

In this second pass of the analysis the energy and vector momentum are calculated for all the tracks and only those events are saved which contain at least one π^-. The input to this pass are the "S files" saved on the first pass, which contain all the trigger and upstream beam detectors, the TOF information, the tracks from the DC, and the scalar information. The output from this pass consists of one saved analyzer output which contains the following for each track:

Word #		Quantity
1	=	Particle track#
2	=	X (mm) at back of DC
3	=	θx in DC
4	=	Y (mm) at back of DC

5	=	θy in DC
6	=	Px (MeV/c) in Center of Mass (cm) frame
7	=	Py (MeV/c) in cm frame
8	=	Pz (MeV/c) in cm frame
9	=	Energy (MeV)
10	=	# of DC planes in track

and in addition it saves one group per event of the following summary information:

1	=	Summary grp ID = 100
2	=	$\sqrt{ADC_{hi}^2 + ADC_{lo}^2}$ for V_4
3	=	π^- Multiplicity
4	=	Total Multiplicity
5	=	Z Sum from Black Wall
6	=	# of Slats hit in Black Wall
7	=	# Z = 1 Slats
8	=	Z_{max} from Black Wall
9	=	Slat # for Z_{max}
10	=	Positive particle Multiplicity

I'll refer to the output files from this pass as "R files". The size of these "R files" is about three to four percent of the size of the raw data files.

The momentum reconstruction was done using the Chebychev polynomial method. This method was originally developed by H. Wind[36] *et al* at CERN. The biggest advantage of this method, as compared to the method of successive approximation, is that it takes orders of magnitude less computing time. The computer code which is used at HISS to generate the coefficients of these Chebychev polynomials, and a complete description of the procedure, has been written by Doug Olson[37]. I will briefly describe the basic ideas here.

The main idea is that the vector momentum of a particle is some function of the coordinates of the particles trajectory as it passes through three position sensitive detectors which straddle a magnetic field. The vector rigidity (momentum / charge) is completely specified by the five quantities, the X and Y (horizontal and vertical) positions at the target, the X and Y positions at the back of the Drift Chamber, and the deflection angle of the particle relative to the beam. One may thus express each component of the rigidity ($R^{(i)}$) of a particle as some function of these five parameters:

$$R^{(i)} = R^{(i)}(x_1,x_2,x_3,x_4,x_5)$$

As the Chebychev polynomials are only defined for arguments in the range $-1 < x < 1$, the actual variables used in the polynomials are mapped onto this range. The goal is thus to determine the coefficients of the series of Chebychev polynomials which approximate the quantity of interest. By choosing particular trajectories such that the variables used in the Chebychev polynomials are the zeroes of the polynomials, the coefficients may be easily calculated using the orthogonality relation for the polynomials. The series of polynomials may be expanded to give whatever accuracy is desired in approximating the function of interest. In figure #3.6 I show a plot of the error in a pion's reconstructed momentum versus the magnitude of the momentum using the Chebychev coefficients which were used in the analysis. The data in this plot is generated by integrating pions, over the range of

momentum shown, through the HISS magnet, using the known field map, and noting where these tracks intercept the front and back planes of the DC. The error shown is the difference between the reconstructed momentum using the Chebychev method and the hit locations in the DC, and the known momentum of the input pion.

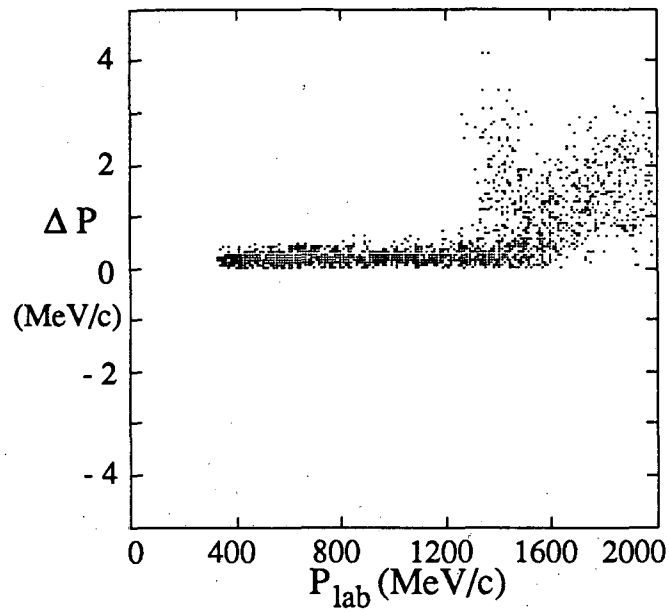

Figure #3.6 Errors in momentum due to Chebychev coefficients.

In addition to generating a set of Chebychev coefficients for the negatively charged pions, a set is generated for the positively charged tracks and for the beam tracks. Recall that the target was positioned just off center in the HISS dipole. As such, the position of the beam on the target is calculated using the known rigidity and mass out of the BEVALAC, and the direction and position of the momentum vector for the beam, upstream of the magnetic field, as given by the PLUTO detectors.

Momentum Resolution

The information contained in the upstream beam vector and the X-Y position of the tracks at the front and back plane of the Drift Chamber actually overdetermine the rigidity (momentum/charge) of the downstream tracks. As the magnetic field has no affect on the component of a particle's velocity along the direction of the field, in this case the Y or vertical direction, the vertical angle of a track through the Drift Chamber is not necessary in calculating the rigidity (note: There is a slight focusing effect in the Y direction due to the fringe field. This is taken into account via the Chebychev coefficients when calculating a

track's momentum.). The information on the Y component of momentum is extracted using the Y position at the target and the Y position at the back of the Drift Chamber for the fit track. We use the difference in the deflection in Y in the Drift Chamber between the fit track in the DC, and for the track reconstructed using the Chebychev coefficients, to derive the momentum resolution for the pions. This quantity, which I'll refer to as DYcheb - DY is illustrated in figure #3.7 below.

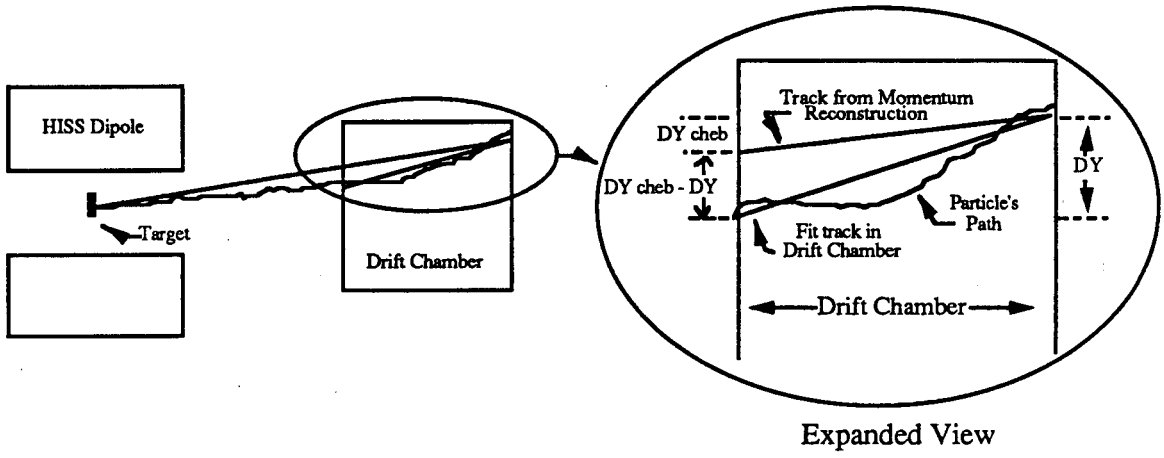

Figure #3.7 Illustration of quantity DYcheb - DY.

In figure #3.8 I show the distribution in DYcheb - DY for some Argon on KCl, central trigger data. The edges of the distribution shown have been cut off via a software cut. The width of this distribution is due to a mixture of the Multiple Coulomb Scattering (MCS) downstream from the target (exit window of HISS vacuum tank, air, and the windows, wires, and gas of the DC) and the position and angle resolution of the DC in the

Y direction. If one has a similar distribution for the X direction one may use these distributions to smear the hit locations of the pions in the DC, recalculate the pion's momentum, compare them to the unsmeared pion track's momentum, and get the error in the momentum of the pions due to these two effects (MCS downstream plus DC resolution)

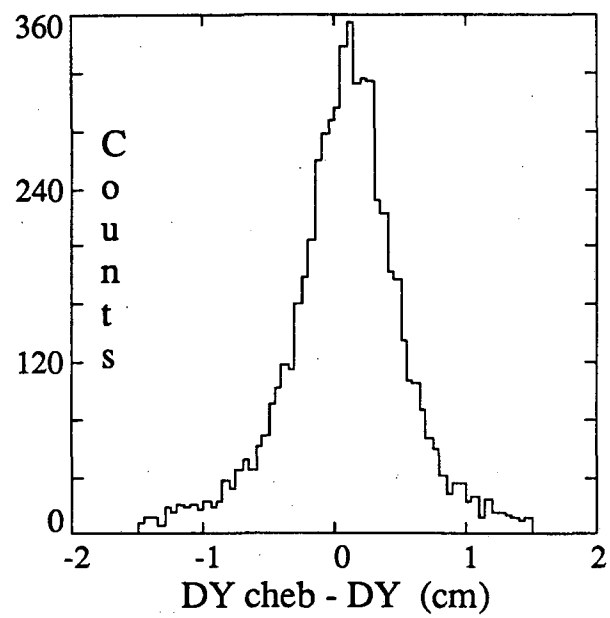

Figure #3.8 DYcheb - DY.

This distribution in X, which I'll refer to as DXcheb - DX, is not expected to have the same width as that for the Y direction. This is because although the MCS component will be the same, the DC does a much better job in determining the position and angle in the X (horizontal) direction. In the absence of MCS one may calculate the ratio of the resolution of the DC in the X direction as compared to the Y direction. In this limit one expects the ratio of the X to Y resolution to be approximately 0.4.

To determine the scaling factor to use in this procedure I employed a simple Monte Carlo procedure. The program starts with a pion at the center of the HISS dipole and then propagates the pion through the vacuum window, the air and the DC. It breaks the path into a large number of steps, calculating the MCS along the way, and ends up with the hit locations of this track at each of the fifteen planes of the DC. The program next smears these hit locations using a gaussian distribution, the width of which is used as a variable parameter, to approximate the single plane position resolution of the DC. These hit locations were then passed into the same three-dimensional fitting code used in the DC tracking software and the parameters (x, θ_x, y, θ_y) for the track extracted. The values of

DYcheb - DY and DXcheb - DX are then calculated and the results passed into a plotting routine. I varied the width of the gaussian used to smear the DC hit locations until the width of the DYcheb - DY distribution and the per plane residuals from the monte carlo matched those in the data. The ratio of the widths of the DXcheb - DX and DYcheb - DY distributions may then be read off of the plots. This ratio turned out to be .53, i.e. the appropriate width of the distribution in the X direction is .53 times the width of the Y distribution.

One now has the information necessary to determine the momentum resolution of the system, for this data set, taking into account the MCS downstream of the target and the DC resolution. One must now take into account the MCS of the pions in the target, and the position resolution at the target as given by the upstream beam vector. The procedure is as follows. Momentum analyzed pion tracks are read in to a track fuzzing routine along with the tracks DC information. This routine smears the hit locations of the tracks at the front and back planes of the DC by randomly sampling the DY distribution previously extracted from the data, and using the appropriate geometric and scaling factors. It then calculates the angles of the smeared track, passes this information into the momentum reconstruction routine, and calculates the momentum for this smeared track. At this point the procedure takes into account the error in the momentum of the pions due to MCS in the target. The program randomly determines a depth in the target for the starting point of the pion and calculates, in a statistical manner, the change in the angle of the pion, and hence it's momentum, due to MCS as it traverses the target. The momentum of the smeared pion track is then modified to include this effect.

At this point one has the momentum resolution which will have an effect on the pion correlation analysis. It includes the MCS in the target and all downstream material to the end of the DC, plus the position and angle resolution of the DC. As is shown in figure #3.9 below, this momentum resolution ($\Delta P/P$) is about 2.5% in the center of mass frame. The error in the momentum of the pions due to the position resolution of the beam on the

target cancels out to first order in the analysis as one will always be dealing with the relative momentum of the pions.

For completeness, and because I'll be showing inclusive pion cross sections and extracting some slope parameters later, I also extracted the contribution to the momentum resolution due to the position resolution at the target. I extract this contribution as follows. After the pion tracks from the DC have been fuzzed, and before the call to the momentum reconstruction routine, I smear the hit locations of the beam at the two PLUTO detectors by sampling a gaussian with a mean of zero and a standard deviation equal to the position resolution of the PLUTOs, and adding this value to the hit positions. The momentum is then reevaluated, the contribution due to MCS in the target added, and the resulting momentum compared to the initial momentum for the pions. The resulting momentum resolution including all the contributions is shown in figure #3.9 below in both the center of mass and lab frame.

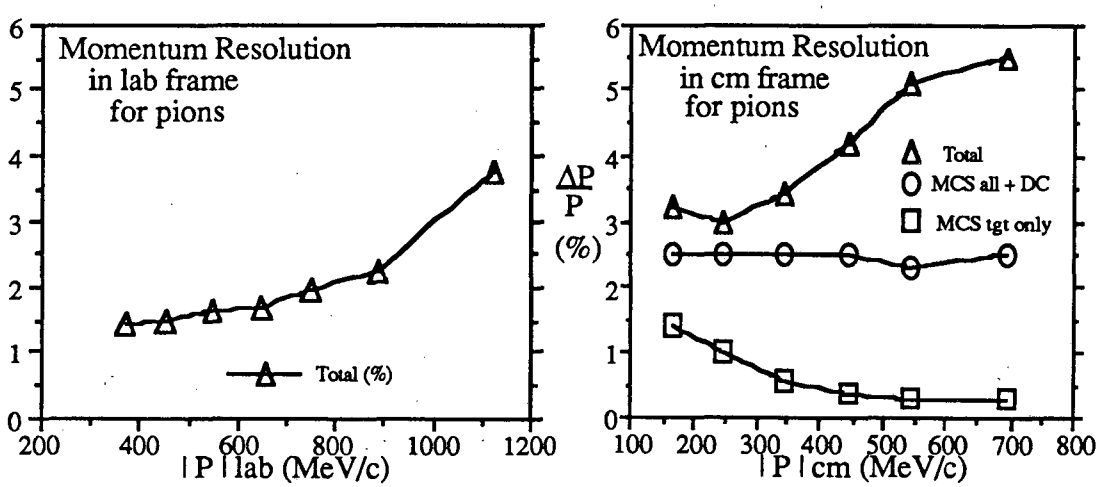

Figure #3.9 Momentum Resolution.

Particle Identification

Using the rigidity information from the Drift Chamber, and the velocity information from the TOF walls, we are able to clearly identify π^+s, K^+s (very few), protons, ^{3}He, A / Z =2 nuclei (deuterons and ^{4}He), and tritons in the positive particle spectrum. The negative

particle spectrum contains essentially only π^-s, as one would expect at these energies as the production cross sections for K^- are about four orders of magnitude smaller[38] than for π^-. Thus, for the negative pion correlation analysis presented in this thesis, one need only separate the negatively charged particles from the positively charged particles. One then identifies all of the negatively charged particles as π^- s. The information we use to distinguish between the positively and negatively charged particles is the position - angle (in the bending plane) correlation of the tracks in the Drift Chamber. Figure #3.10 below

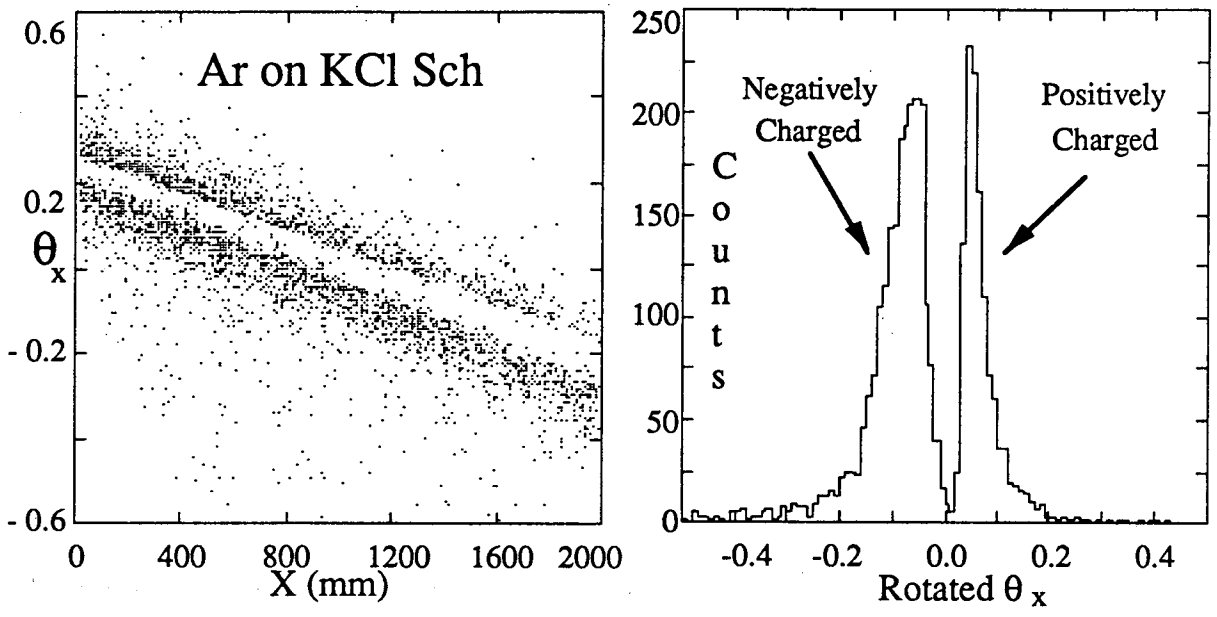

Figure #3.10 Negative Particle ID.

demonstrates the technique. The plot to the left shows the position versus the angle (in bending plane of HISS) in the DC for some tracks. The points in the lower portion of the plot are the negatively charged tracks and the points in the upper portion are the positively charged tracks. The momentum of the particles increases as one moves in the direction of the gap from either side. If one had infinite momentum particles the gap between the two regions would disappear. To get the plot on the right one rotates the angles for the tracks so that the gap in the plot to the left is parallel to the horizontal axis (X in DC) and perpendicular to a rotated θx axis, and histograms the points onto this rotated θx axis. As

indicated in the plot the π^-s are well separated from the positively charged tracks. Collaborators from U.C. Riverside have done the calibrations necessary to get particle identification for the positive particles and are currently investigating the proton - proton correlations in the data.

Cuts Applied to Data

There are six cuts applied to the data in this second pass. Only events which satisfy all of these cuts are saved into the "R files".

The first cut, as was stated at the beginning of this section, is that the event contain at least one π^-. The reason I don't require at least two π^-s at this stage is to allow me to examine the inclusive π^- momentum distributions.

The second cut is merely the requirement that the projection of the beam onto the target via the Chebychev method was "good". "Good" denoting that the position and angle for the beam trajectory given by the PLUTO detectors corresponded to a momentum within the region covered by the Chebychev coefficients.

The third and fourth cuts correspond to a check that the beam focus hadn't changed, and that the beam trajectory for the event in question was in the expected envelope. The cut is placed on delta X_1 and delta Y_1 in the PLUTO detectors. Recall that delta X_1 was the difference between the horizontal position of the beam as seen by PLUTO #1, and as determined by the horizontal position in PLUTO #2 and the X_1-X_2 correlation due to the beam focus. The distributions in Delta X_1 and Y_1 are shown in figure #2.5 back in the section on the PLUTO detectors for the Xenon beam. The cuts for both the Xenon and Argon beams were that Delta X_1 and Y_1 were between -.7 and + .7 cm. These cuts on the focus were quite loose and eliminated a very small percentage of the data.

The fifth and sixth cuts were on the charge ID of the beam upstream of the target. The cuts placed minimum and maximum values on the ADC value of the S2 scintillator and the fourth root of the product of the ADC values for the four phototubes (E, W, U, D) of PLUTO #2. In figure #3.11 I show these distributions for the two beams.

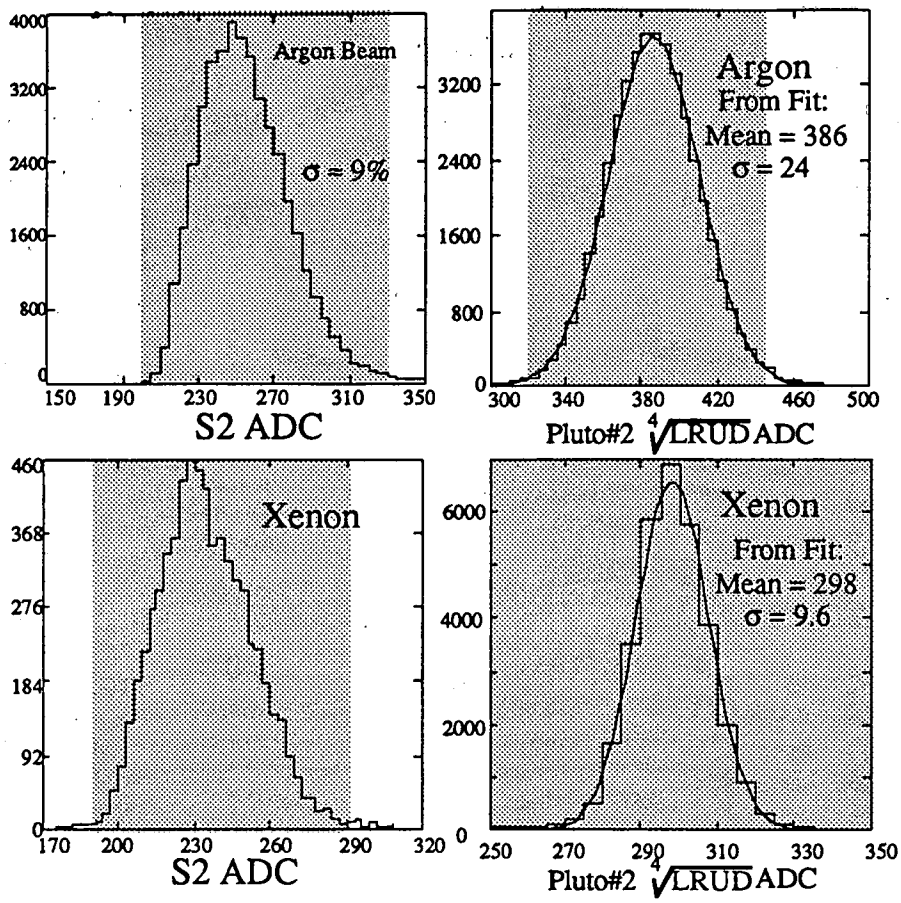

Figure #3.11 Beam ID cuts for second pass.

The cuts passed the parts of the distributions which lie in the shaded regions. As with the cuts on the beam focus discussed earlier, these charge ID cuts eliminate a very small percentage of the data.

Third Pass, Matrix Filling

As stated previously, in this analysis we fit the two pion correlation function to the distribution of relative momentum (q) and relative energy (q_0) for the correlated (same event) pion pairs, divided by the same distribution for the uncorrelated (different event) pion pairs. The method of forming pion pairs from different events is commonly known as event mixing. The technique used in this analysis is to first fill matrices from the distributions of correlated and uncorrelated pion pairs. One then divides these two matrices, cell by cell, to end up with the matrix used to fit the correlation function. I'll first explain

how the pion pairs are formed, and then explain how the matrices for the uncorrelated pion pairs are filled to take into account the various systematic corrections to the data.

The procedure starts by reading in the "R files", saved in the second pass through the data, for the trigger and target combination of interest. From this point on in this procedure there will be a number of requirements placed on the events, and on the pions within these events, which are used to make the pion pairs used in the analysis. The reader should note that both the correlated and uncorrelated pion pairs are formed only from the pions contained in these events and further that all pions used in forming correlated pairs are used in forming the uncorrelated pairs. This care in using the exact same pions in the two distributions is to eliminate as much as possible any bias in the event mixing method. An event cut is checked at this point which must be satisfied if the event is to be passed into the pair analyzer. The cut is a fairly loose one on the ADC signal in V_4 and the maximum charge in the Black wall. The actual values used in this cut will be given in the section on fitting the HBT function.

The information for the good events is then passed into the pair analyzer. On the first call to this analyzer a number of parameters are initialized. I'll discuss the sensitivity of the final HBT fit on these parameters in the section on fitting. These parameters are:

1. The minimum number of remaining planes required in the pion's track from the DC.

2. The minimum value of X (horizontal position) at plane #7 of the DC.

3. The maximum value of X at plane #7 of the DC.

4. The minimum value of Y (vertical position) at plane #7 of the DC.

5. The maximum value of Y at plane #7 of the DC. These four position cuts allow one to define the aperture of the detector setup

6. The minimum value for the pion momentum in the projectile frame. This parameter will be used to investigate if there is any effect due to final state Coulomb

attraction (between the pions and any remaining projectile fragment) on the extracted HBT parameters.

7. A number for the beam ID (Argon or Xenon).

8. The β (v/c) for the frame in which you'd like the momentum to be evaluated, relative to the lab frame. The analysis for the symmetric systems is always done in the nucleon-nucleon center of mass frame. This parameter will be used to investigate the dependence of the HBT fit parameters on the choice of frame in performing the analysis for the asymmetric, KCl on Lanthanum system.

9. The minimum value of momentum to pass, evaluated in the frame in which the HBT analysis is to performed. This parameter and the next allow one to perform the analysis as a function of the individual pion's momentum.

10. The maximum value of momentum to pass, evaluated in the same frame as 9.

The parameters above are set only in the first call to the pair analyzer. In all subsequent calls to this analyzer the first quantity checked is the number of pions in the event (in the summary group out of analyzer #15). If the event contains less than two pions no further action is taken and the program moves on to the next event.

If the event contains two or more pions a loop is entered over the pions which checks if the pion's track is within the required aperture at plane #7 of the DC, transforms the momentum to whatever frame was specified (this is only necessary if one wishes to perform the analysis in a frame other than the nuc.-nuc. cm frame), calculates the magnitude of the momentum in the projectile frame and checks whether it's larger than the minimum specified, and checks if the pion's momentum is within the specified range. If there are less than two pions in the event which satisfy all these conditions the program returns and goes on to the next event. If there are two or more pions which pass these requirements an event counter is incremented and the information for the accepted pions (event counter value, P_X,

P_y, P_z, E, X, θ_x, Y, θ_y, multiplicity of event) is loaded into an array. The program continues in this process until it has collected ten events which pass all the checks.

When ten such events have been collected the pair analyzer goes into a loop over the events. It forms all possible pairs within each event, and for each pair calculates the relative X,Y, and Z components of momentum, the relative energy and transverse momentum, the summed momentum, the efficiency of the DC and tracking software to find this pair, and the Gamow factor for the pair. All these quantities are loaded into an output group which also contains a flag identifying the group as a correlated (as opposed to uncorrelated) pion pair.

The efficiency of finding the pair is arrived at by merely calculating the value of DX for the pair and using an interpolation procedure to get the efficiency from the curves shown in the section on the tracking efficiency.

The Gamow factor[26], which I'll discuss in greater detail in the fitting section, is calculated from a widely used formula and is used to correct for the shifting of close, correlated pion pairs to larger relative momentum and energies due to their mutual Coulomb repulsion.

After all the correlated pion pairs have been formed, and their output groups loaded into the output array, the analyzer goes into a loop over the first nine of the ten events collected. For each of these events a loop is entered over the pions within the event. For each pion a further loop is entered over all the pions in all the events with event numbers greater than that from which the pion was selected. Pion pairs are formed using the selected pion and all the pions in these other events. For each pair the same quantities are calculated as those for the correlated pairs and the values loaded into output groups along with a flag identifying it as an uncorrelated pair. With the loops as described above, all possible uncorrelated pion pairs are made once, and only once, using all the pions contained in the ten events.

The choice of how many events to collect before forming the correlated and uncorrelated pion pairs dictates what the ratio of correlated to uncorrelated pairs will be. If I assume that each event in the analysis has an average of two pions, the number of correlated pairs one can form from N collected events is, of course, equal to N. The number of uncorrelated pairs one can form using the pions in these N events is:

$$2\sum_{i=1}^{N-1}(N-i)$$

The ratio, of the number of uncorrelated to correlated pairs is thus:

$$\frac{\#\,\text{Uncorr.}}{\#\,\text{Corr.}} = \frac{2\sum_{i=1}^{N-1}(N-i)}{N} .$$

For N equal to 10 this leads to a ratio of 9. Using this ratio one may calculate how the statistical uncertainty in the quantity which will eventually be fit to the HBT function, the ratio of the number of correlated to uncorrelated pion pairs, is affected. As shown below:

$$\sigma\,(\%) = \sqrt{\sigma^2_{\text{corr.}}(\%) + \sigma^2_{\text{uncorr.}}(\%)} = \sqrt{\sigma^2_{\text{corr.}} + \frac{\sigma^2_{\text{corr.}}}{9}} = 1.05\,\sigma_{\text{corr.}}(\%)$$

the statistical uncertainty in this ratio is only increased by 5% from that which one would get if one had an infinite number of uncorrelated pairs. In the analysis the ratio of uncorrelated to correlated pairs turned out to be ≈ 16, thus, this contribution to the statistical error is a little less than calculated above.

These correlated and uncorrelated pion pairs are next passed into the analyzer which does the matrix filling. Whereas in the passage of the data into the pair analyzer there were criteria specified which the pions must pass to be used in the pairs, when the pairs are passed into the matrix filling analyzer one may also impose some conditions on which pion pairs are used. These parameters are:

1. Minimum DLo cut. This will be used to eliminate the pairs which have values for the DC closeness parameter DLo that are in the region where the tracking efficiency varies rapidly with DLo, and in which the efficiency is a function of both DY and DX.

2., 3. Minimum and maximum values for the summed momentum of the pion pairs. I'll use these parameters to investigate the effect of the mean momentum of the pions on the HBT fit parameters. This procedure is theorized to yield information about the space-time evolution of the pion emitting source.

4., 5. Which words to select, from the pion pairs word groups, for ultimately using as the variables in the HBT fit. For the "standard" fit one selects the relative momentum (q) and the relative energy (q_0) here, to extract the values of their conjugate variables the radius (R) and the lifetime (τ). I'll also use this feature to select the relative transverse and parallel momentum of the pairs ($q_\perp$, $q_{//}$) to investigate the shape of the source, and the relative X and Y components of momentum to check the analysis technique (one expects the two transverse dimensions of the pion source to be equal when averaged over a number of events).

6. The maximum relative parallel momentum of the pion pairs. As the Bose-Einstein enhancement shows itself only for bosons (in this case the pions) which are in nearly the same state, it will be necessary to set this limit fairly low in order to investigate the X and Y components of the source radius.

7. Minimum allowed value of DX. This is used, as is the DLo cut above, to eliminate those pairs for which the DC efficiency is rapidly changing.

8., 9. The range of the variables to be used in the HBT fitting (i.e. q and q_0 from 0 to 400 MeV/c and MeV respectively), and the number of bins to use for the variables.

The effect of these criteria on the HBT results and the values ultimately used in the analysis will be discussed in the section on fitting the HBT function.

As the pion pairs are passed through this analyzer they are checked to see if they pass the criteria set above. If so, the variables to be used in the HBT fit are selected and the

indices for the matrix bin are calculated. As an example, suppose the fit is to use q and q_0 as the fit variables, the range of the matrices is to be 0 to 400 in each variable, and there are to be 40 bins in each variable. If the incoming pair has q equal to 78 and q_0 equal to 42 the program will determine that some value for this pair is to entered into matrix bin (8,5).

The flag of the pion pair is checked next to determine if it is a correlated or uncorrelated pion pair. If it's a correlated pion pair, the value in the appropriate matrix bin of matrix number one is increased by one. If it's an uncorrelated pair, there are four matrices which have the values in the appropriate bin incremented by the appropriate amount. The systematic correction which one wishes to apply to the data dictates by what amount the value in a given matix's bin is incremented.

The quantity used to increment the bin's value in matrix number two is the product of the DC efficiency times the Gamow factor for the pion pair.

The quantity used to increment the bin's value in matrix number three is the Gamow factor for the pair.

The quantity used for matrix number four is just one.

The quantity used for matrix number five can be either the Drift Chamber efficiency, or the product of the DC efficiency, the Gamow factor, and a background correction factor which I'll call delta, for the pion pair. I'll define and discuss this factor delta in the section on fitting the HBT function.

The output of the third pass through the data is thus five matrices, one for the correlated pairs, and four for the uncorrelated pairs.

Fourth Pass, Fitting

It's a bit of a misnomer to describe the fitting, and for that matter the matrix filling of the previous section, as a pass through the data. As shall be seen in this section, the matrix filling and the fitting are done many times in order to chart out the dependence of the final

HBT parameters on all the various cuts and limits which one may set in the analysis. This section is divided up as follows:

I'll first derive the function which is minimized in this analysis for fitting the HBT parameters, and describe the graphical technique which I'll be employing to assign the errors to said parameters.

In the second section I'll show the dependence of the final fit on a number of the adjustable parameters in this analysis, the value I settled on for the particular cut, and where applicable, any information which may be gleaned from the dependence on the parameter.

In the third section I'll describe the systematic corrections applied to the data and show how they affect the final HBT fit parameters.

Method used for Fitting

The functions which I will fit to the data are:

$$C_2(q,q_0) = N[1 + \lambda e^{(-q^2R^2/2 - q_0^2\tau^2/2)}] \ ,$$

$$C_2(q_\perp, q_{//}) = N[1 + \lambda e^{(-q_\perp^2R_\perp^2/2 - q_{//}^2R_{//}^2/2)}] \text{ , and}$$

$$C_2(q_\perp, q_{//},q_0) = N[1 + \lambda e^{(-q_\perp^2R_\perp^2/2 - q_{//}^2R_{//}^2/2 - q_0^2\tau^2/2)}]$$

The function to be minimized is derived using the Method of Maximum Likelihood[39]. In the following discussion I'll be referring only to the fit of the first of the forms given above for C_2, but the method is identical for all the forms. The distribution to be fit to the data, C_2 above, is characterized by the four parameters N, λ, R, and τ. The observables in this experiment correspond to the number of counts for the correlated pion pairs in the q-q_0 matrix bins. I'll represent these data points individually by c_{ij}. To represent the product of the number of counts in the uncorrelated pion pairs (u_{ij}) and the function C_{2ij} I'll use $u_{ij}C_2$. I'll represent the probability distribution function (p.d.f.) for data point ij by $f(c_{ij}, u_{ij}C_2)$. The p.d.f. gives the probability that one would observe the number of counts in the bin, c_{ij}, for a given set of parameters N, R, λ, and τ, given the assumed form for C_2, and the observed number of counts in the corresponding bin for the uncorrelated pion pairs, u_{ij}.

The principle of maximum likelihood then states that the best values for the HBT parameters will be those which maximize the joint p.d.f. for all the data. If the data points are independent, which is the case in this analysis, this joint p.d.f., also known as the Likelihood, is:

$$L\,(N', R', \lambda', \tau') = \prod_{ij} f\,(c_{ij}, u_{ij}C'_2)$$

The primes above just denote that this is the likelihood for a given set of the fit parameters, N', R', λ', τ', and for a given form of C_2.

Without making any assumptions about the number of counts in a given c_{ij}, or that the distribution for c_{ij} is a normal distribution, the most general distribution to use for the p.d.f. is a Poisson:

$$f(c_{ij}, u_{ij}C_2) = \frac{e^{-(u_{ij}C_2)}\, u_{ij}C_2{}^{c_{ij}}}{c_{ij}!}$$

For the sake of rigor I will derive the function to be minimized via two methods. In the first method I will derive the function to be minimized using the Poisson p.d.f. above. In the second method I will show that for the data set in this analysis (i.e. good statistics) the Poisson p.d.f. converts to a Gaussian, and the Method of Maximum Likelihood leads to a Chi-squared minimization.

Method I

To begin, one takes the negative log of the Likelihood function. It is a standard practice in performing a Maximum Likelihood analysis to take the log of the Likelihood function to convert the product which appears in the function into a sum, which is more tractable. The maximum of the log of the function, and of the function itself, give identical values for the parameters of interest. By taking the negative of the log one merely converts the task at hand from one of maximizing the function to minimizing it.

$$\ell \equiv -\ln L = -\sum_{ij} \ln\left[\frac{1}{c_{ij}!}\,(u_{ij}C_2)^{c_{ij}}\, e^{-u_{ij}C_2}\right]$$

$$= \sum_{ij} \ln c_{ij}! - \sum_{ij} c_{ij} \ln(u_{ij}C_2) + \sum_{ij} u_{ij}C_2$$

Applying Stirling's approximation: $n! = \sqrt{2\pi n}\, n^n e^{-n}$

$$\ell = \sum_{ij} \ln\left[\sqrt{2\pi c_{ij}}\, c_{ij}^{c_{ij}} e^{-c_{ij}}\right] - \sum_{ij} c_{ij} \ln(u_{ij}C_2) + \sum_{ij} u_{ij}C_2$$

$$= \sum_{ij} c_{ij} \ln c_{ij} - \sum_{ij} c_{ij} + \frac{1}{2}\sum_{ij} \ln 2\pi c_{ij} - \sum_{ij} c_{ij} \ln(u_{ij}C_2) + \sum_{ij} u_{ij}C_2$$

$$= \sum_{ij} u_{ij}C_2 - \sum_{ij} c_{ij} - \sum_{ij} c_{ij} \ln \frac{u_{ij}C_2}{c_{ij}} + \frac{1}{2}\sum_{ij} \ln 2\pi c_{ij}$$

Expanding the log which appears in the third term to second order:

$$\ln \frac{u_{ij}C_2}{c_{ij}} \approx \frac{u_{ij}C_2 - c_{ij}}{c_{ij}} - \frac{1}{2}\left[\frac{u_{ij}C_2 - c_{ij}}{c_{ij}}\right]^2$$

Putting this into the equation for ℓ leaves:

$$\ell = \sum_{ij} \frac{(u_{ij}C_2 - c_{ij})^2}{2\, c_{ij}} + \frac{1}{2}\sum_{ij} \ln 2\pi c_{ij}$$

One may drop the last term as it's a constant and will affect only the magnitude of the minimum of ℓ, but not the values of N, R, λ, and τ for the minimum. This leaves one with the function which is to be minimized to extract the best values for the HBT parameters below:

$$\ell = \sum_{ij} \frac{(u_{ij}C_2 - c_{ij})^2}{2c_{ij}}$$

The standard errors, σ_i, are assigned to the fit parameters using a graphical technique[39,40]. Referring to figure #3.12, one constructs the contour corresponding to $\ell_{min} + s^2/2$, where s equals one for the one σ error, two for the two σ error, etc., by varying the two parameters being plotted(in the figure R and λ).

All other parameters (in this example N and τ) are allowed to vary to minimize the function ℓ. The errors are then read off of the rectangle which bounds the resulting ellipse, as shown.

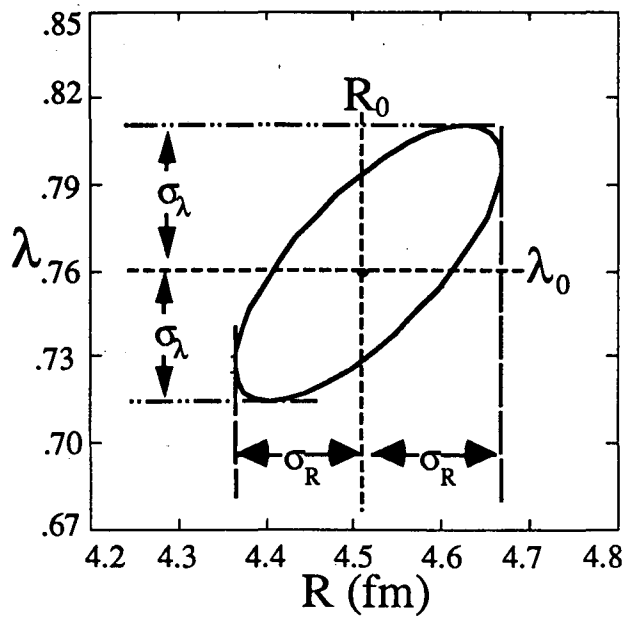

Figure #3.12 Graphical Error Technique.

Method II

Now, following the method in reference 39, one can show that, with a few conditions, the Poisson p.d.f. goes to a Gaussian p.d.f., and maximizing the Likelihood becomes identically equal to minimizing Chi-squared. One begins again with the Poisson p.d.f.:

$$f(c_{ij}, u_{ij}C_2) = \frac{e^{-(u_{ij}C_2)}\, u_{ij}C_2^{\,c_{ij}}}{c_{ij}!}$$

Using $x_{ij} \equiv c_{ij} - u_{ij}C_2$

$$f(x_{ij}, u_{ij}C_2) = \frac{e^{-(u_{ij}C_2)}\, u_{ij}C_2^{\,x_{ij} + u_{ij}C_2}}{(x_{ij} + u_{ij}C_2)!}$$

$$= \frac{e^{-(u_{ij}C_2)} u_{ij}C_2^{\,u_{ij}C_2}}{u_{ij}C_2!} \left\{ \frac{u_{ij}C_2}{u_{ij}C_2 + 1} \cdot \frac{u_{ij}C_2}{u_{ij}C_2 + 2} \cdots \frac{u_{ij}C_2}{u_{ij}C_2 + x} \right\}$$

One may rewrite the term which multiplies the brackets above, using Stirling's approximation, if the number of counts in the bins is large enough so that the error in using the approximation is small. The larger the value of n the smaller the percentage difference between n! and the value arrived at by using Stirling's approximation. For n equal to five, Stirling's approximation is off by only two percent. For n equal to 10 the difference is slightly less than one percent. For the statistics in the data set in this experiment we may make this approximation. This leads to:

$$f(x_{ij}, u_{ij}C_2) = \frac{1}{\sqrt{2\pi u_{ij}C_2}}\left\{\frac{u_{ij}C_2}{u_{ij}C_2+1}\cdot\frac{u_{ij}C_2}{u_{ij}C_2+2}\cdots\frac{u_{ij}C_2}{u_{ij}C_2+x}\right\}$$

Looking at the terms in brackets, one may multiply through, top and bottom, by $(u_{ij}C_2)^{-1}$ which yields:

$$\left\{\frac{u_{ij}C_2}{u_{ij}C_2+1}\cdot\frac{u_{ij}C_2}{u_{ij}C_2+2}\cdots\frac{u_{ij}C_2}{u_{ij}C_2+x}\right\} = \left\{\frac{1}{1+1/u_{ij}C_2}\cdot\frac{1}{1+2/u_{ij}C_2}\cdots\frac{1}{1+x/u_{ij}C_2}\right\}$$

Now, for $x/u_{ij}C_2 << 1$:

$$1+\frac{x}{u_{ij}C_2} \approx e^{\frac{x}{u_{ij}C_2}}$$

This leads to:

$$f(x_{ij}, u_{ij}C_2) \approx \frac{1}{\sqrt{2\pi u_{ij}C_2}}\exp\left\{-\left[\frac{1}{u_{ij}C_2}+\frac{2}{u_{ij}C_2}+\cdots+\frac{x}{u_{ij}C_2}\right]\right\}$$

$$= \frac{1}{\sqrt{2\pi u_{ij}C_2}}\exp\left(\frac{-1}{u_{ij}C_2}\sum_{i=1}^{x} i\right)$$

With the final approximation:

$$\sum_{i=1}^{x} i = \frac{x}{2}(1+x) \approx \frac{x^2}{2} \qquad \text{for } x >> 1$$

One is left with:

$$f(x_{ij}, u_{ij}C_2) \approx \frac{1}{\sqrt{2\pi u_{ij}C_2}}\, e^{\frac{-x^2}{2u_{ij}C_2}}$$

Which is the Gaussian distribution. To summarize the requirements in the approximations used, one needs $u_{ij}C_2 >> x >> 1$ and the distribution of $c_{ij} - u_{ij}C_2$ to be a maximum at zero and symmetric about $u_{ij}C_2$.

Now, if one starts with a Gaussian probability distribution function, and writes down the joint probability function for all the data, i.e. the Likelihood function, one gets:

$$f(x_{ij}, u_{ij}C_2) = \frac{1}{\sqrt{2\pi\sigma_{ij}^2}}\exp\left\{-\frac{1}{2}\left[\frac{c_{ij}-u_{ij}C_2}{\sigma_{ij}}\right]^2\right\}$$

$$L\,(N', R', \lambda', \tau') = \prod_{ij} f(x_{ij}, u_{ij}C_2) = \exp\left\{ - \sum_{ij} \frac{1}{2}\left[\frac{c_{ij} - u_{ij}C_2}{\sigma_{ij}}\right]^2 \right\} \prod_{ij} (2\pi\sigma_{ij}^2)^{-1/2}$$

If one now defines Chi-squared as:

$$\chi^2 \equiv \sum_{ij} \left[\frac{c_{ij} - u_{ij}C_2}{\sigma_{ij}}\right]^2$$

The Likelihood becomes:

$$L\,(N', R', \lambda', \tau') = e^{-\frac{\chi^2}{2}} \prod_{ij} (2\pi\sigma_{ij}^2)^{-1/2}$$

Looking at this last expression for the Likelihood it is clear that maximizing the Likelihood is equivalent to minimizing Chi-squared when one has a Gaussian p.d.f. Thus the function to be minimized following this prescription is:

$$\sum_{ij} \left[\frac{c_{ij} - u_{ij}C_2}{\sigma_{ij}}\right]^2$$

Where $\sigma_{ij}^2 = c_{ij}$. This is the same function as that derived earlier starting with the Poisson p.d.f., with the exception of the factor of two in the denominator, which has no effect on where the minimum of the function will fall. In assigning errors to the HBT parameters which result from minimizing the Chi-squared function, one uses the same graphical technique described previously (and illustrated in figure #3.12), with the contours corresponding to $\chi^2_{min} + s^2$ where s equals one for the one sigma error, two for the two sigma error etc.

Cuts Applied in Fit

There are a number of cuts and/or limits applied to the data in loading the matrices and performing the fit to the HBT function. In this section I'll describe the nine which are applied in the standard HBT fit (for N, λ, R, τ) and illustrate how the extracted HBT

parameters are affected by four of these cuts for the data set consisting of an Argon beam on a KCl target with the SCh trigger.

The nine cuts and limits used in the standard fit for the data set specified above are:

1.) $0 \leq \sqrt{V4\ ADC_{top}^2 + ADC_{bot}^2} \leq 200$ (See figure #2.13)

2.) $0 \leq Zmax \leq 8$ (See figure #2.13)

3.) Minimum number of planes/track in the Drift Chamber ≥ 7

4, 5.) Position of tracks at plane #7 of DC. $0 \leq x\ (mm) \leq 2000$ $-90 \leq y\ (mm) \leq 1420$

6.) Minimum value of DC closeness parameter DLo for pairs. $Dlo \geq 100$ mm

7.) Minimum value of DC closeness parameter DX for pairs. $DX \geq 40$ mm

8.) Minimum value for relative momentum of pair. $q_{min} \geq 10$ (MeV/c)

9.) Minimum number of counts/bin for correlated and uncorrelated pairs

#cnts/bin > 5

Cuts #1 and 2 above are merely quality cuts on the events passed along to the matrix filling analyzer. Recalling the discussion that went along with figure #2.11, these cuts eliminate those events in which the beam projectile which satisfied the trigger conditions was followed too closely down the beam pipe by another nuclei.

The next cut is on the minimum number of planes which must be associated with a track in the DC for the pion to be passed into the pair analyzer. Shown below are plots of the HBT fit parameters, R and λ, versus the minimum number of planes/track. For all the fits represented in the plots, the other eight cuts were set to their final values, given above. To give the reader a sense as to what magnitude of change is significant as the minimum number of planes/track is varied, I've included error bars corresponding to plus or minus one σ for the data point corresponding to the final value used for the cut (7 planes).

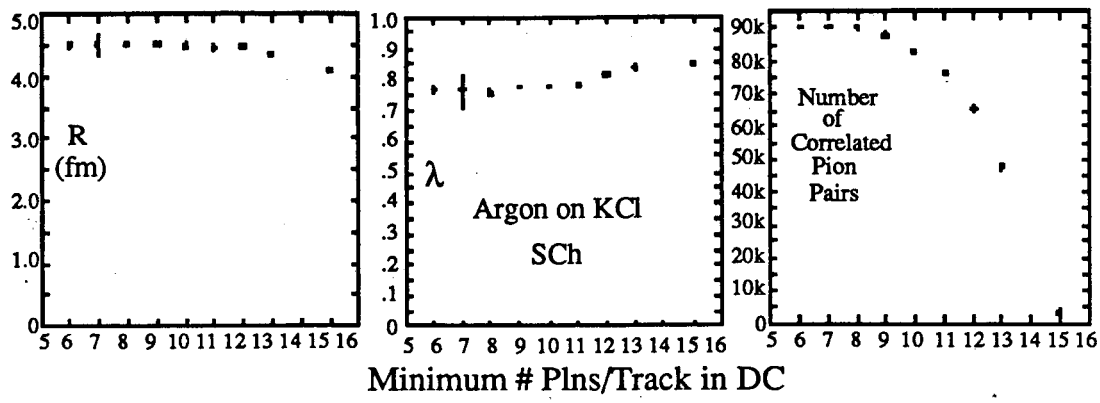

Figure #3.13 HBT fit as a function of Minimum # planes/track.

Also shown is a plot of the number of correlated pion pairs left in the analysis as a function of the minimum number of planes/track. The average number of planes/track for the pions in this data set is thirteen. The reason that the number of pion pairs starts to drop off fairly rapidly when ten or more planes/track are required is due to the fact that the mean pion multiplicity for the events in the analysis is just slightly larger than two. Thus when one of the tracks in the pair fails to satisfy the cut, the pair is lost. As can be seen from the plots, the final result is not very sensitive to this cut.

The next cut in the list is one which in effect defines the aperture of the detector setup. There is nothing in the tracking software that requires that a track either enters through the front of, or exits through the back of, the Drift Chamber. As such, one ends up with tracks which enter through the side and exit via the back, enter through the front and leave through a side, etc. The fact that one ends up with a number of tracks with less than fifteen planes is due mostly to the above effect, and to a lesser degree due to the removal of wires shared by more than one track in the tracking software. The values shown for this aperture cut, in the list of cuts given earlier, corresponds to the requirement that the track is within the active volume of the Drift Chamber at plane number seven. I'll postpone showing how this aperture cut effects the HBT fit parameters until the next section, where I'll discuss a technique which is used to correct for this systematic aperture effect.

The next two cuts in the list deal with how close the tracks which form a pair are in the Drift Chamber. As I discussed back in the section on the efficiency of the DC and tracking software, for tracks with a value of DLo less than 100 mm the efficiency is not only rapidly changing, but is a function of both DX and DY. For values of DLo greater than 100 mm the efficiency can be parameterized as a function of DX alone. In figure #3.14 below I show the values of the HBT parameters for various values of DX where all

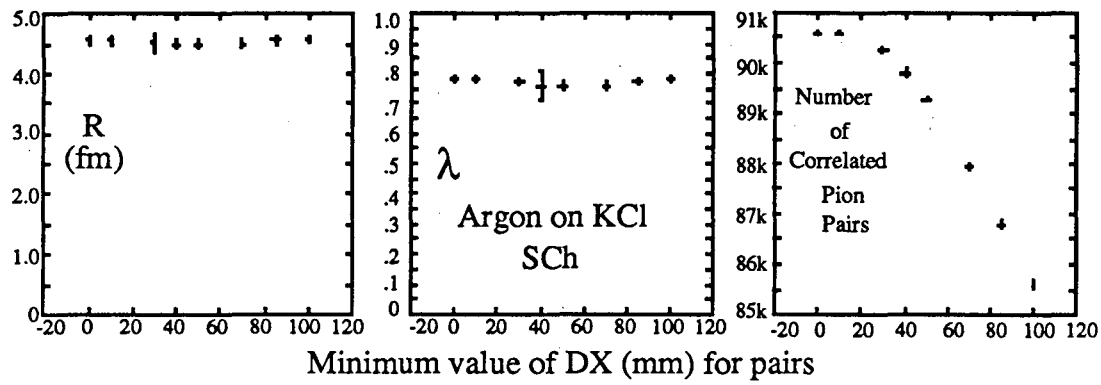

Figure #3.14 HBT versus minimum value of DX for pairs.

other cuts, including DLo, are set at their standard values (given in list earlier). The one σ error is shown for the data point which corresponds to the final value used for the DX cut. The fits shown are corrected for the Drift Chamber efficiency. As I'll show in the next section, the systematic correction for the Drift Chamber efficiency has a small effect on the HBT fit parameters.

The next cut is on the minimum value of the relative momentum (q MeV/c) for the pairs. The fits represented in the plots below show the dependance of the final HBT

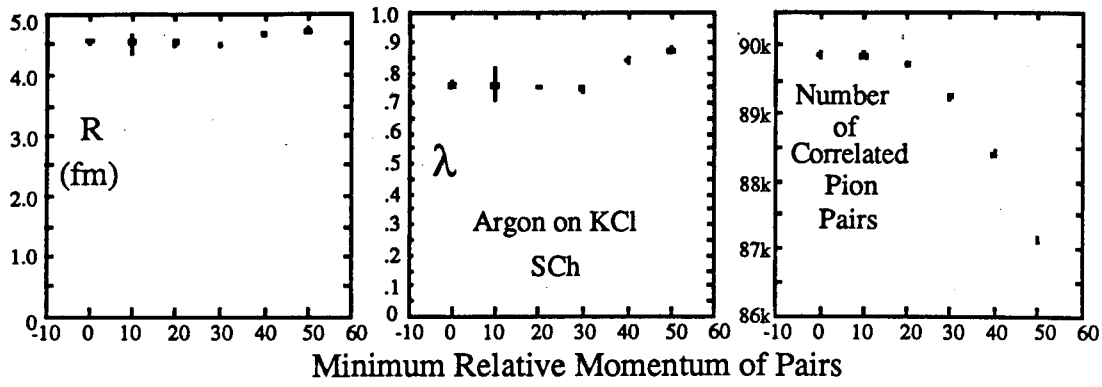

Figure #3.15 HBT fit parameters versus minimum value of q (MeV/c) for pairs.

parameters on this cut. Notice that the HBT fit parameters are insensitive to this cut until one reaches a value of $q_{min} \geq 30$ MeV/c. The relative insensitivity below 30 MeV/c is due to the relatively low population of pion pairs in this region. Notice that above 30 MeV/c the radius and chaoticity (λ) parameters vary in the same manner. In this region the two parameters are correlated in that an increase in R can be compensated for by an increase in λ. This correlation, which has been observed earlier[5] by others, will manifest itself by a tilt, or angle, between the semi-major axis of the error contour ellipse and the coordinate axes, as shown in figure #3.12.

The final cut I wish to illustrate in this section is the minimum number of counts required in a matrix bin for the bin to be included in the fit. As shown in the plots below, the radius and chaoticity parameters are not sensitive at all to this cut. This lack of sensitivity is

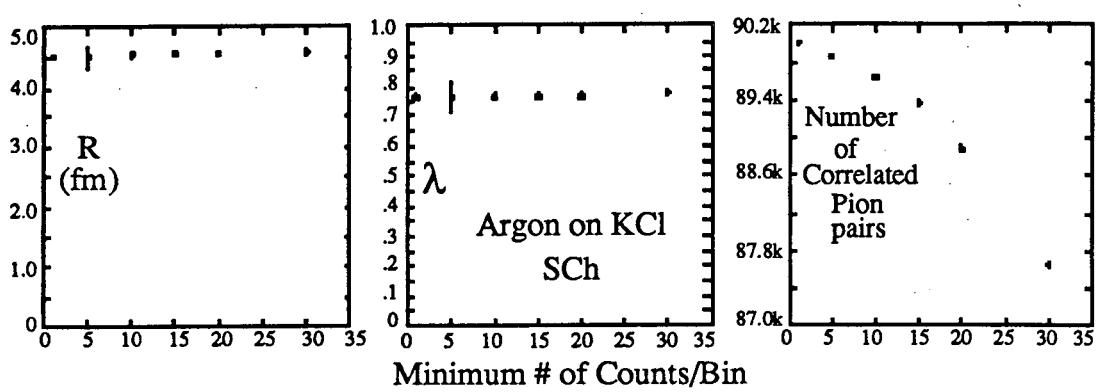

Figure #3.16 HBT fit parameters vs the minimum # cnts/bin

due mostly to the good statistics of the data set which leads to well populated bins and thus very few bins excluded by this limit. This is shown graphically in the rightmost plot of the figure above. The large bin populations over the entire range of relative momentum (q) and relative energy (q_0) enhance one's justification in using Stirling's approximation in the derivation of the function which is minimized, shown at the start of this section.

The bin width (i.e. 10 MeV x 10 MeV/c or 20 MeV x 20 MeV/c bins etc) is one other quantity which is chosen when filling the matrices. I've done fits using bin widths of 8, 10, 16, 20, 25, and 40. The resulting HBT fit parameters are essentially unaffected up through the bin widths of 20. Lambda starts decreasing for bin widths of 25, and at bin widths of 40 the radius parameter R has decreased by one sigma. Unless otherwise specified all fits presented will be for bin widths of 10.

If, at this point, the reader is wondering why I've spent a few pages describing cuts and limits which have almost no effect on the resulting HBT fit parameters, then the purpose of the section has been served. Besides pointing out that I've checked for all these possible effects in the analysis, and for completeness have specified all cuts and limits applied, I wish to emphasize the point that the results of this HBT analysis, on this data set, are highly insensitive over a large range, to any of the choices one picks for these cuts.

Systematic Corrections

In this section I'll describe the four systematic corrections applied in the analysis and show how, and by how much, they affect the resulting HBT fit parameters.

I begin with the systematic correction for the Drift Chamber's efficiency in finding close pairs of tracks. This effect introduces a bias into the final matrix used in the fit (matrix of correlated pairs divided by matrix for uncorrelated pairs) as follows. Whereas the efficiency of the Drift Chamber in finding a pair of tracks in the same event may be, say, 80% for a pair with a certain value of the DC closeness parameter DX, the efficiency of finding pairs of tracks in the uncorrelated pairs is always 100%. Thus if there is any correlation between the relative momentum and or relative energy and the closeness of the tracks in the DC, a bias will be introduced. The bias will show up as a decrease in the population of some of the bins in the correlated pion pairs matrix, as compared with the population one would get if the DC efficiency was 100%.

This systematic effect is corrected for by introducing the same DC pair efficiency into the uncorrelated pairs matrix. When an uncorrelated pair is formed values for DX and DLo are calculated. When this pair is passed into the analyzer which fills the matrices, the value in the appropriate bin is increased by one in one of the uncorrelated matrices, and by whatever the DC efficiency is for the pair (say .8) for another of the uncorrelated matrices. This allows one to apply the correction or not, by simply choosing which uncorrelated matrix one uses to divide into the correlated pairs matrix.

When I present the results for the various beam target combinations I'll list the results of the fits with and without the various corrections. To give the reader an idea just how small this DC efficiency effect is I note here that for the Argon on KCl data set with the central (SCh) trigger, the application of the DC efficiency increases both R and λ by an absolute amount of .01 (R = 4.51 fm, λ = .76). The reason this correction is so small is due primarily to the absence of a significant correlation between the relative momentum and or energy and the spatial separation of the tracks in the DC.

The second systematic correction which one may apply in the analysis is to correct for the effect due to the mutual Coulomb repulsion between the pions in the correlated pairs. In reference #26, the authors show that the effect of a two-body final state interaction is merely to multiply the correlation function which one would observe in the absence of the interaction by a penetration factor. For the repulsive Coulomb interaction between the two π^- in a pair this penetration factor is the well known Gamow factor:

$$G(\eta) = \frac{2\pi\eta}{e^{2\pi\eta} - 1}$$

$$\text{where } \eta = \frac{m_\pi \alpha}{\sqrt{q_0^2 - q^2}}$$

This Gamow correction is applied to the uncorrelated pion pairs before the HBT function is fit. When filling the matrices for the uncorrelated pairs I increment the value in the appropriate bin of one of the matrices by the value of the Gamow factor. In this way one effectively introduces the mutual Coulomb repulsion into the uncorrelated pairs before the HBT function is fit. As discussed earlier, with the one correlated and four uncorrelated pair matrices one may perform the fit of the HBT function with or without the various corrections, or series of corrections applied. The Gamow correction has a substantial ($\approx 4\ \sigma$) effect on the λ parameter and a relatively small ($\approx \sigma/3$) effect on the radius parameter. For the Argon on KCl, SCh data set, the application of the Gamow correction raises the value of λ from .57 to .76 and raises the value of R from 4.46 to 4.51 fm.

The third systematic correction which may be applied to the data is to correct for what, for lack of a better name, I'll refer to as the finite aperture effect. This correction technique was first derived and applied by Zajc[31] in his analysis of a pion interferometry experiment using the Janus spectrometer at the BEVALAC. That this aperture effect can bias the uncorrelated pair spectrum is seen through the following argument. Assume that the spectrometer one uses has a small phase space acceptance for pions, so that the pion pairs always have $p_1 \approx p_2$. If one now allows the range of acceptance to shrink towards

zero one ends up with pion pairs which are all within the relative momentum region of the correlation. If one now applies the technique of event mixing to this data one ends up with uncorrelated pairs which also have $p_1 \approx p_2$, thus washing out the enhancement in the correlation region. This effect does not go away completely as one goes to the limit of a four π spectrometer. In this limit the same effect shows up in the uncorrelated pairs, to a lessor degree, due to the finite phase space distribution of the pion source. One could think of the correction in this limit as a finite temperature effect.

I'll forgo duplicating the mathematical derivation of this correction here and refer the interested reader to reference 31. The result is that one calculates a quantity, δ, for each pion in the data set via the following equation:

$$\delta_i = \frac{\sum_{m \neq i} N_m \lambda e^{(-q^2R^2/2 - q_0^2\tau^2/2)}}{\sum_{m \neq i} N_m}$$

where i refers to a particular pion, the sum over m refers to all the other pions, N_m is the number of pions with momentum specified by m, q and q_0 have their normal meanings of relative momentum and energy, and are calculated using pions i and m, and λ, R, and τ are reasonable values for the HBT parameters. One calculates this quantity for all the pions in the data set, and then weights the uncorrelated pair formed using pions i and j by the factor Δ_{ij} given by:

$$\Delta_{ij} = \frac{1}{[1 + \delta_i][1 + \delta_j]}$$

This is an iterative procedure in which one first makes a best guess of the values for the parameters λ, R, and τ. One then performs the HBT fit, using the best guess parameters in the calculation of the weighting of the uncorrelated pairs, and gets a new set of HBT parameters. One then does the HBT fitting again using these new parameters and continues until the parameters converge to stable values.

Looking at the equation for δ given above, one sees that if the data set contained a uniform phase space density of pions, all the δ's would come out to be equal, and hence all the Δ's used to weight the uncorrelated pairs would be equal, and the application of this correction would have no effect on the HBT fit parameters, it would merely change the normalization parameter, N, in the fit. The important quantity is thus how much these δ's vary over the data set. In figure 3.17 below I show plots of these δs versus the magnitude

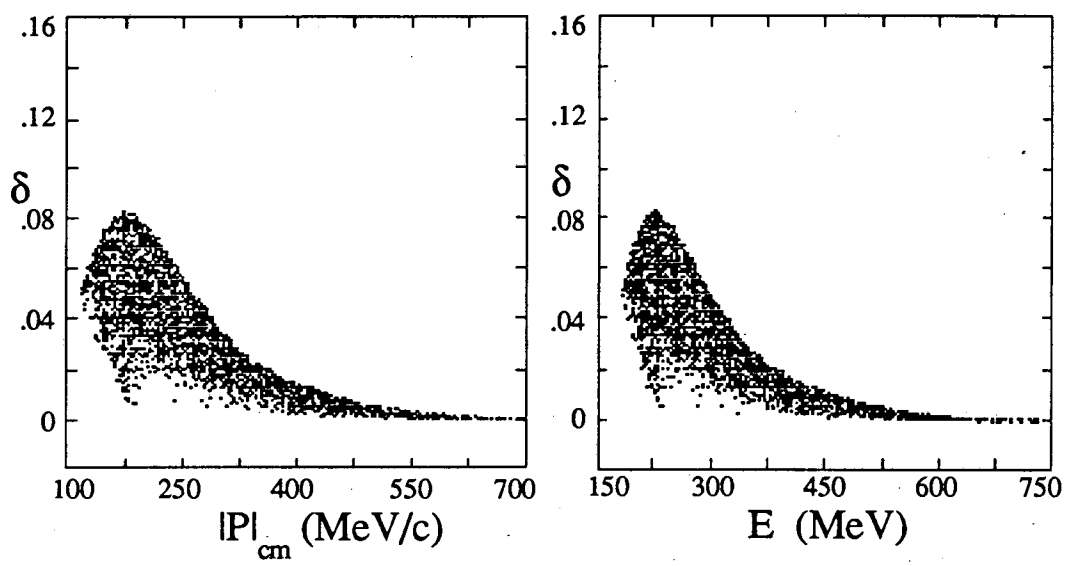

Figure #3.17 Deltas vs center of mass momentum and energy.

of the three momentum and energy of the pions in the nucleon-nucleon center of mass. The data is from the Argon on KCl, SCh trigger set. The δs above were calculated using a subset of four thousand pions and $\lambda = .76$, $R = 4.51$, and $\tau = 0$. The average value of δ for this data set is .03, and, as shown in the plots (on a greatly expanded scale), the maximum value is ≈ .08. Referring back to the equation above for Δ, the weighting factor to be assigned to an uncorrelated pair, one sees that this factor will vary from the value of 1 (if both pions have a δ of 0) to .85 (if both pions have the maximum δ of .08).

In practice, to perform the calculation in a reasonable amount of computer time, when I calculate the δs I always restrict the sum to run over some subset of the pions in the data set. I've applied the correction using subsets of 5,000 and 10,000 pions and for both

cases the HBT fit parameters converge to the same values, in the same number of iterations. From this I conclude that the use of the restricted sum does not affect the result if 5,000 or more pions are used in the calculation.

To check that the final HBT fit parameters are independent of the parameters used in the initial iteration, I've performed the fits on the Argon on KCl, SCh data set, starting with R values from 4 to $\approx$ 4.5 fm, τ values from 0 to 3 fm/c, and λ values from $\approx$ .75 to 1. In all cases the procedure converges, within two iterations, to the same values for the HBT parameters.

To check that this procedure corrects for the size of the spectrometer aperture, I've done the fits with no bounds on the position of the pion tracks at the middle plane of the Drift Chamber, with my standard cut requiring the pion's tracks to be within the physical bounds of the DC at the mid-point ($0 \leq X$ (mm) ≤ 2000, $-90 \leq Y \leq 1420$), and with the requirement that the tracks be within smaller bounds ($200 \leq X \leq 1800$, $60 \leq Y \leq 1340$) at the mid-point of the DC. The number of correlated pion pairs in these three cases was $\approx$ 97k, 90k, and 55k, respectively. The fits with no bounds and the standard bounds started out close before the background correction ($\Delta R \approx .04$ fm, $\Delta\lambda \approx .02$) and converged to values with about the same spread. The fit to the smaller bounds started out with a lower R value ($\Delta R \approx .07$) and a larger λ value ($\Delta\lambda \approx .04$) than those for the standard bounds, and converged to values which differed by $\Delta R \approx 0.1$ (lower) and $\Delta\lambda \approx 0.05$ (larger) from the final values for the standard bounds. Since all these spreads are less than or about equal to the one σ errors in these parameters, I can't really conclude whether this procedure corrected for the size of the aperture or not.

For the standard bounds I use, this correction lowers the values for the radius parameter R by slightly more than 1 σ, from 4.51 down to 4.30 fm. It has no affect on the lifetime parameter τ, leaving it at zero, and increases the λ parameter by about half a σ, from .76 to .78.

Another systematic correction is to use the known momentum resolution of the experimental setup to extrapolate back to infinite (perfect) momentum resolution. Recalling the discussion in the section on how the momentum resolution was derived, I extracted a distribution which I referred to as DY_{cheb} - DY and the scaling factor appropriate for this distribution in the X, or bending plane, direction. By using these distributions to "Fuzz" the pion tracks I obtained the momentum resolution for our experimental setup. To investigate the effect of the momentum resolution on the HBT analysis I used various multiples of these distributions to "Fuzz" the pions tracks, adding on the same multiple times a calculated MCS for the pions in the target. For the data without any fuzzing of the tracks, which corresponds to a fuzz factor of one (i.e. it contains one multiple of the systems momentum resolution), I extracted the HBT fit parameters R = 4.52 and λ = .77. Applying one half of a multiple of the fuzzing distributions and the MCS in the target, which corresponds to a fuzz factor of 1.5, I extracted HBT parameters of R = 4.46 and λ = .76. For a full multiple of the fuzzing distributions and the MCS in the target (fuzz factor of 2) the values dropped to R = 4.22 and λ = .67. In all the fits the lifetime parameter τ came out equal to zero. This lowering of the spatial HBT fit parameter is intuitively what one would expect as the width of the area of enhancement in the relative momentum distribution is inversely proportional to the size of the source, and by smearing the momentum one widens this distribution.

I used the following reasoning to extrapolate to a fuzz factor of zero, corresponding to perfect momentum resolution. Fuzzing the pions momentum can be dealt with as though one is adding together two Gaussians. The first of these Gaussians is that due to the Bose - Einstein enhancement. I'll denote the width of this distribution as σ_{BE}. The second distribution is that due to the finite momentum resolution. I'll denote the width of this second distribution as σ_F. The extracted HBT radius parameter is thus inversely proportional to the square - root of the sum of the squares of these sigmas.

$$R(x) = \frac{C}{\sqrt{\sigma_{BE}^2 + x^2\sigma_F^2}}$$

where x is the fuzz factor and C is a constant. Dividing through the numerator and denominator on the right side by σ_{BE}^2 yields:

$$R(x) = \frac{C / \sigma_{BE}^2}{\sqrt{1 + x^2(\sigma_F / \sigma_{BE})^2}}$$

$$R(x) = \frac{C_1}{\sqrt{1 + x^2 C_2}}$$

where in the last step I've merely renamed some constants.

We now have one equation with two unknowns which one can solve given the values above for R(1), R(1.5), and R(2). The desired quantity is R(0), which will be given by C_1. Using R(1) and R(1.5), and R(1) and R(2), to solve for the constants, and taking the average, gives a value for R(0) of 4.60 fm. Thus the effect of the finite momentum resolution is that the extracted HBT parameters are decreased by about 1.8%. It will be seen later that this shift due to the finite momentum resolution corresponds to about one half of the sigma for the most precise fit presented.

The conclusion I draw from the above simple calculations is not that the effect is precisely equal to 1.8%, but rather that the effect of the finite momentum resolution on the extracted HBT parameters is negligible with respect to the errors in the fits, and thus for this data set one may ignore this correction.

There is another systematic effect that I include here for completeness. This is the Coulomb attraction between any remaining projectile spectator fragment and the negatively charged pions. These effects have been seen in inclusive pion studies[41] as an enhancement of the ratio of the π^- to π^+ cross sections for momentums close to that of the projectile. H.M.A.Radi *et al*[42]. have derived a formula that does a good job of reproducing these inclusive pion cross sections for BEVALAC data taken at 0°. They include not only the regular Coulomb function but also the velocity dispersion of the projectile fragments as has

been observed and parameterized at the BEVALAC. They've also included an averaging technique which weights the various possible impact parameters for the collisions as a function of the probability of producing pions.

Shown in figure #3.18 below is a plot of the enhancement predicted by the formula in the π^- cross section, versus the pions momentum in the projectile frame, for three different values of the parameter σ_0 and for four different projectile fragments. In generating the data for these plots I did not do the impact parameter averaging. This parameter σ_0 is used in the formula for the calculation of the velocity dispersion of the projectile fragments. The larger the parameter the wider the distribution of velocities. This parameter, as initially derived by Goldhaber[43], is thought to be associated with the Fermi momentum of the projectile nucleus. In fragmentation studies at the BEVALAC this parameter has been seen by some to be a little larger and by some to be a little smaller than one would predict from the Fermi momentum of the projectile. When Radi *et al.* fit their formula to the inclusive pion data they found that they got the best fit using a value of 60 MeV/c for σ_0. Fermi momentum would predict a value of approximately 86 MeV/c for this parameter. As seen in the plot below, for a projectile fragment of ^{9}Be, the choice of this parameter is not critical, and for a fairly wide range of values, makes almost no difference for pions with momentum of 10 MeV/c or more in the projectile frame.

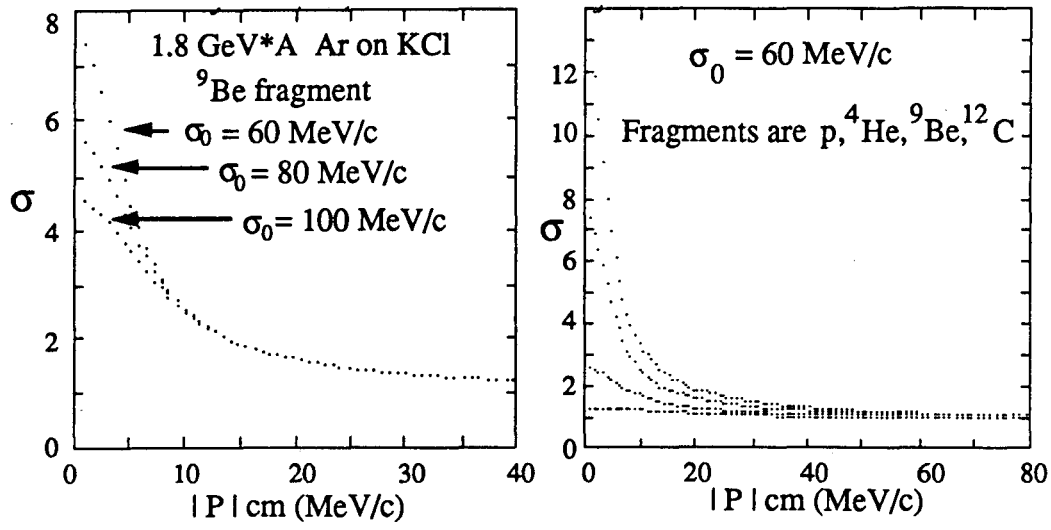

Figure #3.18 Coulomb Effect due to projectile fragment.

Referring now to the plot on the right in figure #3.18, the enhancement in the π^- cross section is shown for various projectile fragments. The two bottom curves, corresponding to projectile spectator fragments of protons and ^{4}He, are the ones to concentrate on for this data set. In previous experiments people have tried to either correct for this effect or have cut out the data thought to be affected. To correct for this effect one must either know, on an event by event basis, what the projectile fragments are and their associated momentum vectors, or, one chooses what one believes to be a reasonable distribution for these fragments and their momenta. One then corrects, on a component by component basis, the momentum of the pions. The other method is to merely transform all the pions momentum into the projectile frame and then place a threshold on the pions momentum in this frame.

I investigated how this Coulomb attraction affected the pion correlation analysis by employing the latter technique above. I performed the HBT analysis with cuts on the minimum allowed pion momentum in the projectile frame rangeing from 0 up to 95 MeV/c. For thresholds on the pion momentum of 0, 5, 10, 15, and 30 MeV/c the value of the extracted HBT radius parameter varied randomly in the range of 4.51 to 4.47 fm while the

lambda parameter varied in the range of .76 to .78. With the threshold at 30 MeV/c ≈ 4% of the total correlated pion pairs were eliminated. For a threshold of 50 MeV/c the radius decreases to 4.39 fm (from 4.51 with no cut), Lambda went to .80, and about 14% of the correlated pion pairs are eliminated. Increasing the threshold up to 95 MeV/c one sees the radius parameter decrease to 4.27 fm, Lambda varies randomly between .80 and .75, and up to 55% of the correlated pion pairs are eliminated.

I interpret the above variations as follows. As shown in figure #2.13(hard trigger plots) for most of the events accepted by the central trigger the largest projectile fragment charge is two or less. Figure #3.18 above shows that for charge two projectile fragments one expects the enhancement in the π^- cross section, small to begin with, to decrease to almost nothing for pion momenta of 30 MeV/c. As there is essentially no variation in the extracted HBT parameters for thresholds up to 30 MeV/c, I conclude that this Coulomb effect is not manifesting itself in this data set and HBT analysis. I believe this is primarily due to the hard central collision trigger which precludes events with highly charged projectile fragments.

As this cut is increased up to 95 MeV/c the pion acceptance and statistics are altered appreciably. As stated above, with the threshold placed at 95 MeV/c, 55% of the correlated pion pairs are eliminated. Another affect of the high threshold is that the mean momentum of the pion pairs increases by ≈ 50 MeV/c. This latter consequence, increasing the mean momentum of the pairs, may, as will be seen in the section on the results, indeed cause the extracted radius parameter to decrease.

Finally, I also investigated, in an approximate manner, how the Coulomb interaction between the participant (i.e. fireball) region and the π^-s affected the HBT analysis. I did this by using the formula below, valid only to lowest order in $Z\alpha$ in the classical mechanical limit[44], to correct, on a component by component basis, the momenta of the pions.

$$\delta p_f(\mathbf{k}) \approx \mathbf{k}\,\frac{Z\alpha m}{(k^2 + k_T^2)R}$$

The formula above approximates the change in the momentum of the pion in the fireball rest frame. Z is the charge of the fireball, α is the fine structure constant (1 / 137), m is the mass of the π^-, R is the radius of the fireball, $k_T = 3mT(m/m_p)$ is the thermal average momentum, T is the temperature of the proton gas, and m_p is the proton mass.

To get an estimate of the upper limit on the size of this effect for the Argon on KCl data set I used the formula above, with the values Z equal 35, T equal 100 MeV, and R equal 4 fm, to correct all the momenta of the pions in the data set. I then performed the HBT analysis and compared the extracted HBT parameters with those I obtained without this correction applied. The Coulomb correction lowered the values of the perpendicular and parallel radii by about one half their associated σs, raised the chaoticity parameter λ by one half of its σ, and raised the lifetime parameter by a little less than one σ. The σs are the one standard deviation errors to the fit parameters as determined via the graphical technique presented earlier in this section.

I applied the same procedure to the Xe on La data set with values of the input parameters of Z equal 90, T equal 100 MeV, and R equal 6 fm. In this case the perpendicular radius was reduced by two - thirds its σ, the parallel radius was reduced by about one fourth its σ, λ was reduced by half its σ, and the lifetime parameter was unchanged from zero.

What I conclude from the above is that this effect is negligible for this experiment. As the upper limit of this effect is less than the uncertainty obtained in fitting the data, and depends on one's assumptions about the charge, size, and temperature of the fireball, I will not apply this correction in the final fits to the data. That the size of the effect is small is not a surprising result as the important quantity in the analysis is the *relative* momentum and energy of the pions. The size of the effect I calculated is very similar to that which others have found[6,31] doing this type of analysis.

Acceptance

In this section I will present the acceptance of the experimental setup due to constraints of both the hardware and the analysis software. As there are not any widely preferred plots to show a systems acceptance I will show a wide enough variety to hopefully satisfy most readers. All the plots which I show in this section are from the Ar on KCl, central collision trigger (Sch) data set. The coordinates are defined such that Px is the component of momentum in the bending plane of the HISS dipole, Py is the vertical or out of bending plane component, and Pz is the component in the direction of the beam, i.e. longitudinal component.

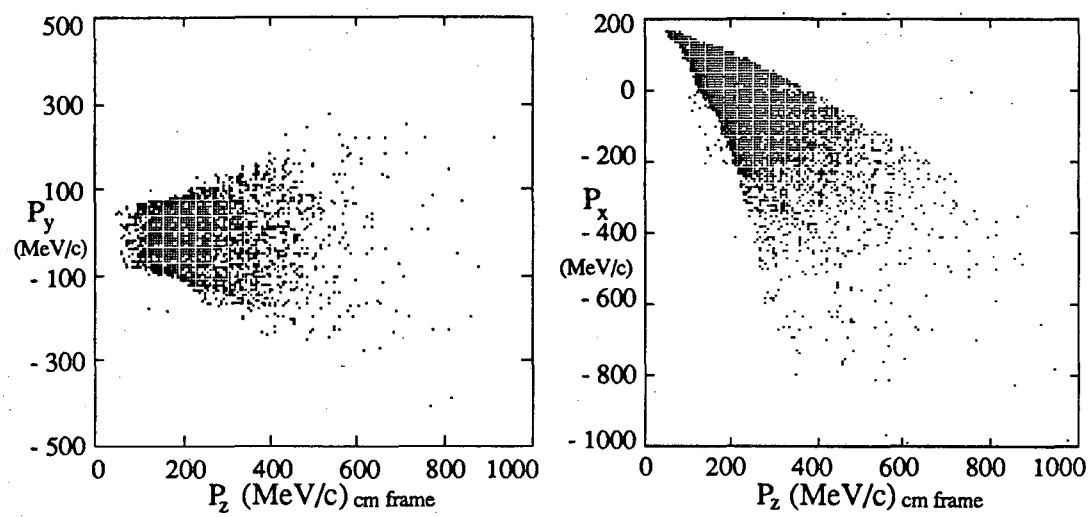

Figure #3.19 Acceptance for P_x, P_y, and P_z.

In figure #3.19 above the inclusive pion acceptance is shown for P_x, P_y, and P_z. The values for P_z are evaluated in the nucleon - nucleon cm system. In the plot to the left, the arcs on the top and bottom edges of the P_y distribution are due to the cut which restricts all pion tracks to be within the physical bounds of the Drift Chamber at it's midpoint. This requirement on the tracks is also responsible for the sharp limits on the top of the distribution for P_x in the plot to the right. The bottom edge of the P_x distribution shows a

small arc from the tip of the distribution (upper left corner) down to a P_x value of about 0 MeV/c which is due to a bound in the Chebychev momentum reconstruction coefficients. The remainder of the lower edge of the Px distribution is again due to the requirement on the tracks in the Drift Chamber.

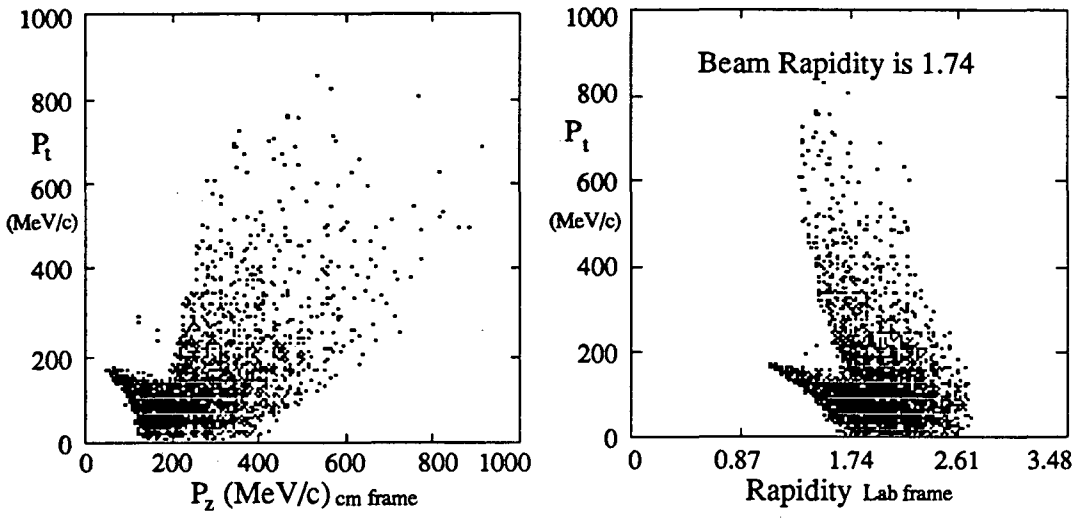

Figure #3.20 P_t vs P_z and rapidity.

The acceptance for P_t (component of momentum transverse to the beam direction) is shown in the figure above as a function of P_z and rapidity. Rapidity is defined as:

$$\text{Rapidity} \equiv y = \frac{1}{2} \ln \left\{ \frac{E + P_z}{E - P_z} \right\}$$

Distributions plotted as a function of rapidity are invariant under boosts in the z direction. The rather odd shape for the P_t distribution in the plots above is due to the upward folding of the negative portion of the P_x distribution that occurs in calculating P_t (i.e. $P_t = (P_x^2 + P_y^2)^{1/2}$). The plot to the right above shows that part of the pion distribution is at, and close to, the rapidity of the beam. This would lead one to expect that the pion momenta in this region would be distorted by the Coulomb interaction with any remaining projectile fragment.

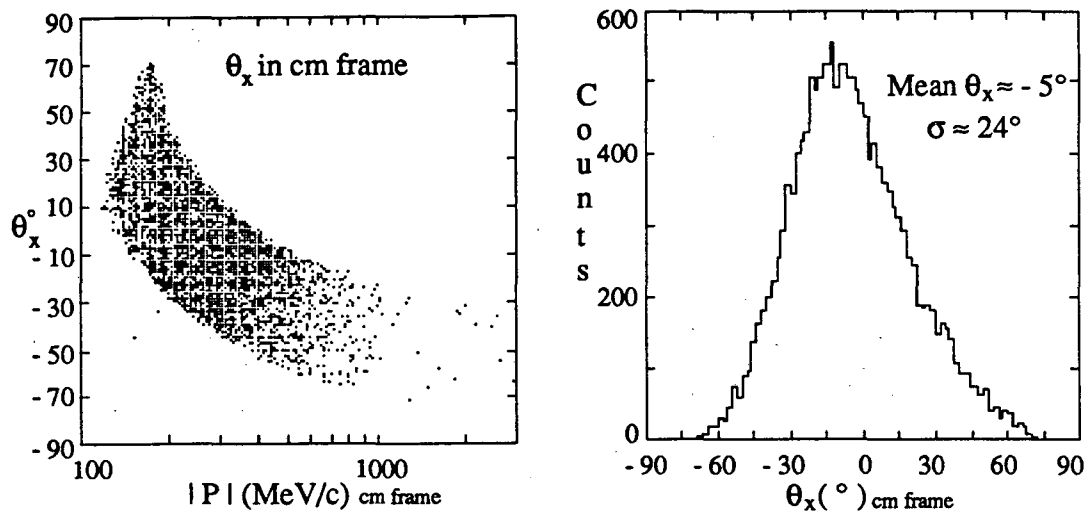

The upper left plot shows the acceptance in θ_x versus the magnitude of the momentum, both evaluated in the nucleon - nucleon cm frame. The upper right plot shows graphically what I've been referring to as pion interferometry at zero degrees in the cm frame. As shown, the pions used in the correlation analysis actually come from a distribution of angles with a mean of about - 5°. The histogram of the inclusive momentum distribution is also shown.

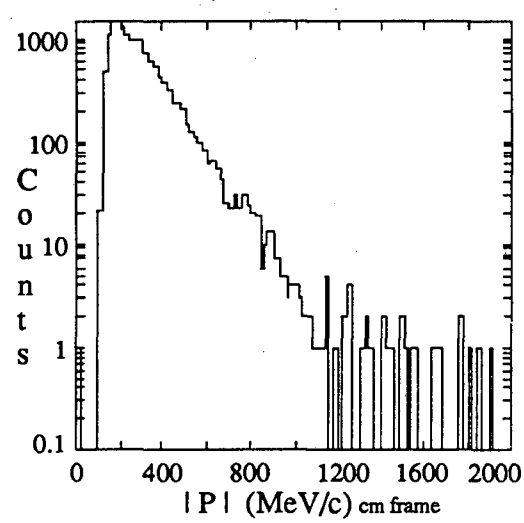

Figure #3.21 Acceptance in θ_x and $|P|_{cm}$.

I now turn to the acceptance for the pion pairs, in particular the distributions for the relative momentum of the pairs (q) and the relative energy of the pion pairs(q_0). To remind the reader, the data shown in the figure below is from the Argon on KCl, central collision trigger data set.

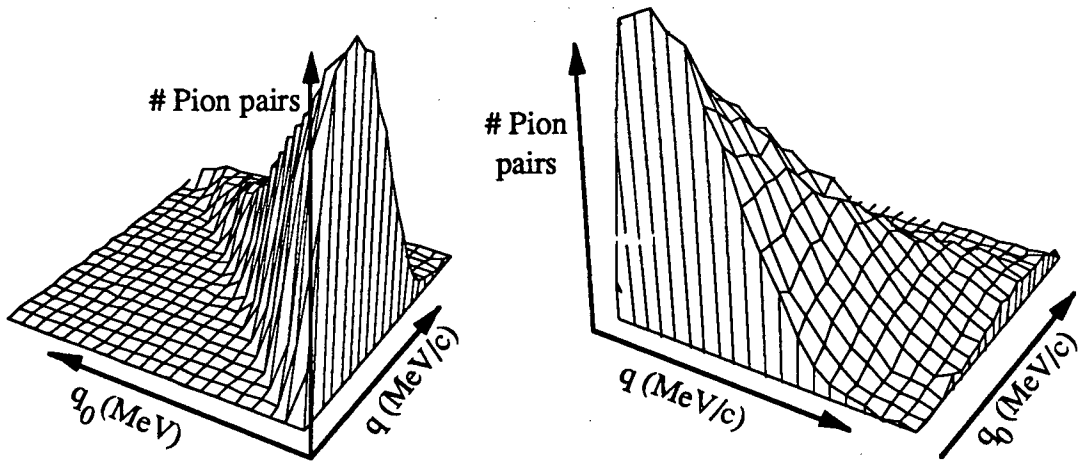

Figure #3.22 Acceptance for Correlated pion pairs, two views.

The bin widths in the plots above are twenty units wide (MeV/c or MeV). Notice that only half of the q - q_0 plane is populated. This is due to a restraint imposed by relativistic kinematics. As pointed out by Zajc[31], this is most easily seen in the following way. In the nucleon - nucleon cm system the relative four - momentum is given by

$$t = (P_1 - P_2)^2 = q_0^2 - q^2$$

where P_1 and P_2 are the four - momentum of the two pions and q_0 and q have their usual definitions of relative energy and relative momentum, respectively. This quantity t is Lorentz invariant, i.e. it must have the same value in any frame in which it is evaluated. If we calculate this quantity in the center of mass frame for a given π^- pair we know that, for equal mass particles, the energy of the two π^- will be equal and their three - momentum will be equal in magnitude and opposite in direction. Evaluating the relative four - momentum in this frame and equating it to the value in the n-n cm frame above we see:

$$\{P_1^* - P_2^*\}^2 = \left\{ (E^* - E^*)^2 - (2Q^*)^2 \right\} = -4\,Q^{*2}$$

$$q_0^2 - q^2 = -4\,Q^{*2}$$

$$\rightarrow q^2 = q_0^2 + 4\,Q^{*2}$$

where E* and Q* represent the energy and the magnitude of the three momentum of the π^- in the two pion cm frame. Thus we see that for all non - zero Q*, $q > q_0$, and hence only half of the q - q_0 plane can be populated. Note that this equivalence between the relative four - momentum in any frame and the relative three momentum for the pion pair in their cm system is used in the evaluation of the Gamow correction factor, discussed in the section on systematic corrections.

Chapter 4. Results

The results will be subdivided for the various beam - target - trigger combinations. In each subsection I've tabulated the fits to the three forms of the correlation function given earlier (section *Methods used in Fit*). To remind the reader these three forms are:

$$C_2(q,q_0) = N[1 + \lambda e^{(-q^2R^2/2 - q_0^2\tau^2/2)}] ,$$

$$C_2(q_\perp, q_{//}) = N[1 + \lambda e^{(-q_\perp^2R_\perp^2/2 - q_{//}^2R_{//}^2/2)}] , \text{ and}$$

$$C_2(q_\perp, q_{//},q_0) = N[1 + \lambda e^{(-q_\perp^2R_\perp^2/2 - q_{//}^2R_{//}^2/2 - q_0^2\tau^2/2)}]$$

The quantities q and q_0 refer to the relative three momentum and energy of the pion pairs. The quantities $q_\perp$ and $q_{//}$ refer to the relative three momentum of the pion pairs perpendicular and parallel to the beam direction, respectively. The fit parameters $R_\perp$ and $R_{//}$ are thus interpreted as measures of the source radius in these two directions.

The results of the fits are shown with the following combinations of systematic corrections applied: no corrections, just the Drift Chamber (DC) efficiency correction, both the DC efficiency and the Gamow corrections, and the DC efficiency, Gamow, and correction for Background correlations all applied. Where calculated, the one σ errors are given for the parameters as derived via the graphical error technique discussed in the section on the fitting method used. Also listed in the tables the reader will find the $\chi 2$ and the number of independent degrees of freedom (NDF) for the fit. Using these two quantities I've calculated what is known[39] as the *Upper - tail area function* using the First approximation to $\chi 2$. This Upper - area tail function (UTAF) gives the probability of getting a value for $\chi 2$ greater than that measured. Its value is the percentage of the area of the $\chi 2$ distribution from the value for $\chi 2$ which one obtains from the fit to the end of the distribution. For a perfect fit this function is equal to its maximum value of one half. The first approximation to the $\chi 2$ distribution used in the calculation of the UTAF is for ease of calculation and gives a very

good approximation to the $\chi 2$ distribution. For all fits the range of the independent variables (i.e. q, qo, $q\perp$, q//) was from zero to four hundred.

The tables given in the subsections also contain the number of correlated and uncorrelated π^- pairs used in each of the fits. The variation in the number of π^- pairs used in the various fits for a given beam - target - trigger combination is due to the different numbers of matrix bins into which the pairs are placed (i.e. $C(q, q_0)$ or $C(q_\perp, q_{//}, q_0)$) and the requirement that all bins used in the fits contain at least five correlated pairs.

I've also included two calculated values for most of the fits. These calculated values are the volume of the pion source as given by the spatial HBT parameters from the fits, and the inverse ratio of this "measured" volume to a calculated volume for an assumed number of participating nucleons at Normal Nuclear Density (NND). In calculating the volumes using the HBT fit parameters I've multiplied all the spatial fit parameters by a conversion factor of 1.52. The origin of this conversion factor is discussed in appendix A. Multiplying the spatial fit parameters which are given in the results tables by this conversion factor (1.52) allows one to compare them to the equivalent sharp sphere nuclear radii given by the familiar formula. For clarity, the values given in the tables are calculated with the following equations:

$$\text{Volume measured} = \frac{4}{3}\,\pi\,(1.52\,R_{fit})^3$$

$$\text{or} = \frac{4}{3}\,\pi\,(1.52\,R_{\perp fit})^2\,(1.52\,R_{//\,fit})$$

$$R_{NND}\,(\text{fm}) = 1.2\,A^{\frac{1}{3}}$$

$$\text{Volume}_{NND} = \frac{4}{3}\,\pi\,R_{NND}^3$$

where R_{fit}, $R_{\perp fit}$, and $R_{//\,fit}$ are the fit values for these parameters as shown in the results tables, and A is the assumed number of nucleons in the participant region (note: if one wishes to convert the fit parameters in the results tables to the equivalent rms values the appropriate conversion factor is $\sqrt{3/2}$). The assumption used for the calculation of the

volume at NND is that the collisions have an impact parameter of zero for the Ar on KCl and Xe on La data, and an impact parameter of 2.1 fm for the Ar on La data. Thus the values of A used in the calculations of the NND volumes are 80 for Ar on KCl, 270 for Xe on La, and 116 for Ar on La. The choice of 80 nucleons for Ar on KCl and 270 nucleons for Xe on La are the maximum numbers possible for these collisions, the choice of 116 nucleons for Ar on La is discussed in the results section for this data set. As a consequence of these assumptions the calculated ratios of the volumes are more suitably interpreted as upper limits for this quantity.

Central Collision Data

Argon on KCl

In this section I'll list the results for our central collision Ar on KCl data set. The details of this trigger, which we refer to as Streamer Chamber Hard, may be found in the earlier section on triggers. The trigger selected ≈ 26% of the geometric cross section for the Argon on KCl system. We took approximately thirty 1600 bpi (bits per inch) magnetic tapes for this trigger. Each tape contained ≈ 40 to 50 thousand events. Out of these approximately 1.2 to 1.5 million raw events we ended up with ≈ 90 thousand correlated pion pairs which passed all the various cuts and acceptance limits discussed in the previous sections (*Cuts applied to Data*, and *Cuts Applied in Fit*). With the scheme used for generating the uncorrelated pion pairs (detailed in section *Third Pass, Matrix Filling*) we ended up with ≈ 1,350,000 uncorrelated pairs. Bin widths of 10 MeV (MeV/c) were used in the first two sets of fits in the table and widths of 20 were used in the last set of fits ($C_2(q_\perp, q_{//}, q_0)$). The results are listed in table #4.1 below.

Table # 4.1 1.8 GeV*A Argon on KCl					
Systematic Corrections Applied	DC eff.		X	X	X
	Gamow			X	X
	Background				X
R (fm)		4.46	4.46	4.51±.14	4.30± .14
τ (fm/c)		0.0	0.0	0.0+1.1	0.0
λ		.56	.57	.76± .05	.78± .05
$\frac{\chi 2}{NDF}$		$\frac{753.2}{726}$	$\frac{750.3}{726}$	$\frac{750.0}{726}$	$\frac{745.1}{726}$
Pr ($\chi 2 \geq \chi 2_{meas.}$)		.15	.18	.18	.23
Volume measured (fm^3)				1349± 125	1170± 114
Volume at NND (A=80) / Volume measured				0.43± .04	0.49± .05
89,847 Correlated π^- pairs, 1,389,400 Uncorrelated π^- pairs.					
$R_\perp$ (fm)		4.58	4.54	4.68± .17	
$R_{//}$ (fm)		3.82	3.91	3.80± .23	
$\lambda_{\perp //}$		.55	.56	.76± .04	
$\frac{\chi 2}{NDF}$		$\frac{1442.8}{1418}$	$\frac{1439.8}{1418}$	$\frac{1434.9}{1418}$	
Pr ($\chi 2 \geq \chi 2_{meas.}$)		.25	.28	.32	
Volume measured (fm^3)				1224± 116	
Volume at NND (A=80) / Volume measured				0.47± .04	
93,375 Correlated π^- pairs, 1,441,300 Uncorrelated π^- pairs.					
$R_\perp$ (fm)		4.51		4.62± .18	4.39± .15
$R_{//}$ (fm)		3.44		3.63± .33	3.48± .30
τ (fm/c)		1.98		$1.08\pm^{1.12}_{1.08}$	$1.30^{+.90}_{-1.30}$
λ		.55		.75 ± .04	.77± .05
$\frac{\chi 2}{NDF}$		$\frac{2107.2}{2081}$		$\frac{2093.6}{2081}$	$\frac{2088.3}{2081}$
Pr ($\chi 2 \geq \chi 2_{meas.}$)		.28		.39	.43
Volume measured (fm^3)				1140± 136	987± 108
Volume at NND (A=80) / Volume measured				0.51± .06	0.59± .06
88,709 Uncorrelated π^- pairs, 1,357,500 Uncorrelated π^- pairs.					

As a true believer in the premise that "A picture is worth a thousand words", I've included a few figures to assist the reader in visualizing the distributions being fit. Figure #4.1 below shows the experimental correlation data (i.e. the distribution as a function of q and q_0 of the correlated π^- pairs divided by the same distribution for the uncorrelated pairs) in the plot to the left and the fit theoretical correlation function to the right. The data and fit shown correspond to the first set of fit parameters in table #4.1 above, with the DC efficiency, Gamow, and background corrections all applied.

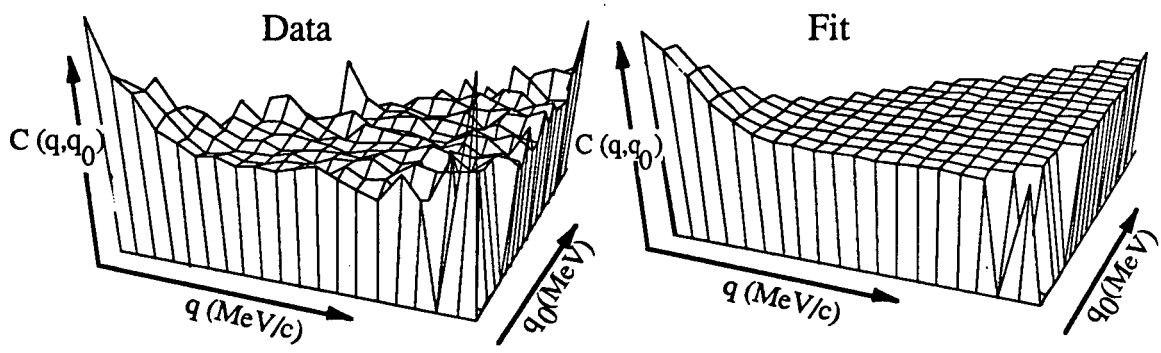

Figure #4.1 $C(q,q_0)$ vs q and q_0, with systematic corrections applied. Notice the expected enhancement in the ratio of correlated to uncorrelated π^- pairs in the low q - q_0 region. Bin widths shown are twenty by twenty (Mev/c and MeV).

As the lifetime parameter is zero for the data and fit shown above, and because historically others have shown correlation results in this manner, figures #4.2a and b below shows the same set of data and the fit, with and without the DC efficiency and Gamow corrections applied, projected onto the q axis.

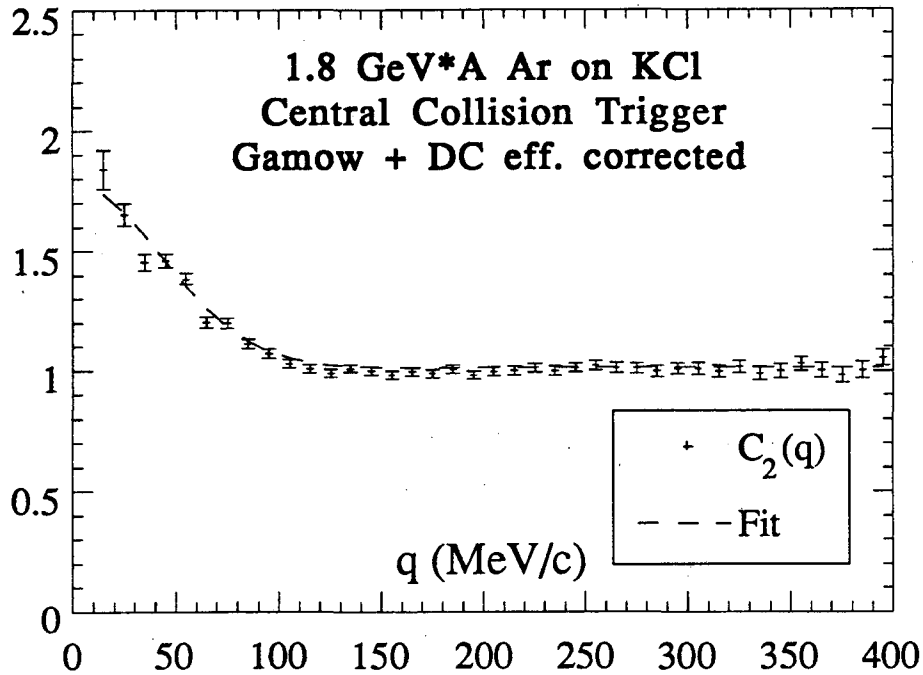

Figure #4.2a $C_2(q)$ vs q with Gamow and DC correction

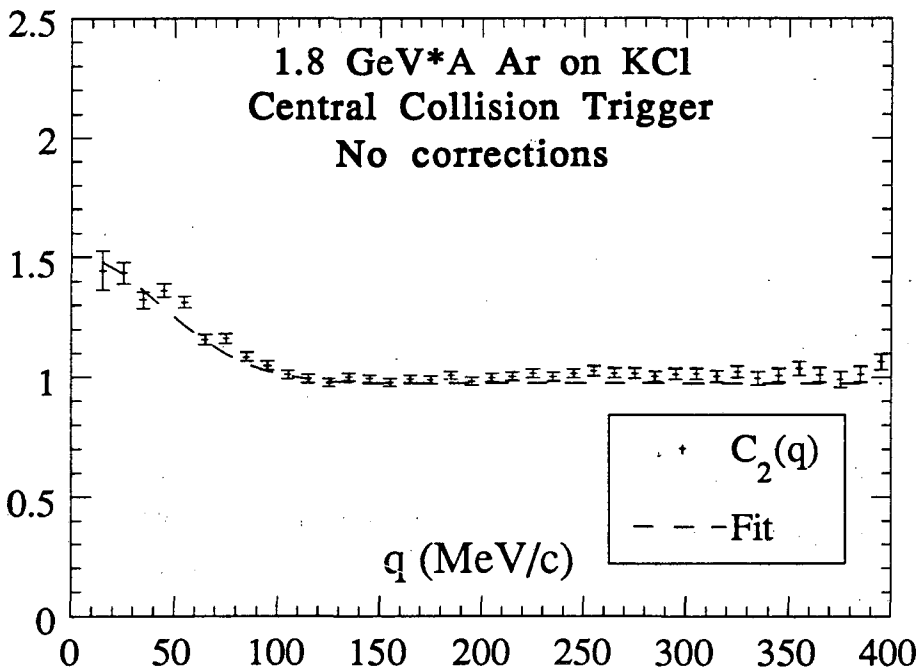

Figure #4.2b $C_2(q)$ with no corrections.

The error bars for the points above are just the statistical errors. The dashed lines are the fit HBT function.

As discussed in the earlier section on fitting, when one plots the error contours the correlation between the various fit parameters can be examined.

Shown in figure #4.3 to the right are the error contours for the same data as shown in figure #4.1 above where the DC efficiency, Gamow, and background corrections are all applied. The contours shown correspond to the one and two standard deviation errors. The positive correlation shown between the chaoticity parameter λ and the radius parameter R is as one would expect, that an increase in R can be compensated for by an increase in λ, and has been seen by others. The lack of any correlation between the radius and lifetime parameters (i.e. error contours are parallel to the axis) is a consequence of the large acceptance of the experimental setup, which has the preferred effect of uncoupling the determination of the two parameters.

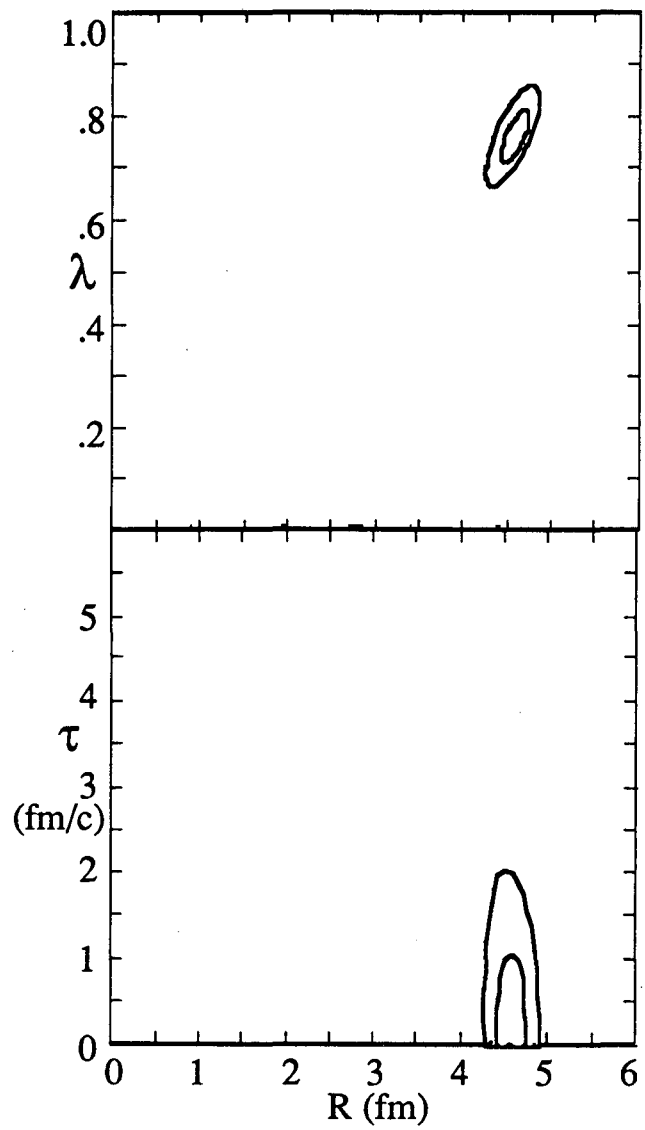

Figure #4.3 Error contours for standard R, τ, λ fit.

It has been suggested by S. Pratt[45] that one may be able to extract information about the evolution of the pion emitting source by performing the HBT analysis as a function of

the mean momentum of the pion pairs in the cm frame. His model incorporates the radial expansion aspects of the hot participant region, as theorized by Siemens and Rasmussen[46], to see how the pion interferometry analysis is affected. What he finds is that the radius parameter R decreases monotonically as a function of **K** ($\mathbf{K} = \mathbf{p}_1 + \mathbf{p}_2$), and that R decreases faster as the ratio of the energy in collective expansion to thermal energy is increased. The physical explanation Pratt gives for this effect is that the faster pions are most likely emitted from the point on the expanding shell which is in the direction of **K**, and therefore appear to come from a smaller effective source. He also points out that another possible explanation could be that as the pion- nucleon cross section falls off rapidly for relative energies above 140 MeV due to the Delta resonance, the faster pions may have a higher probability to escape during the early stages of the collision while the source is small.

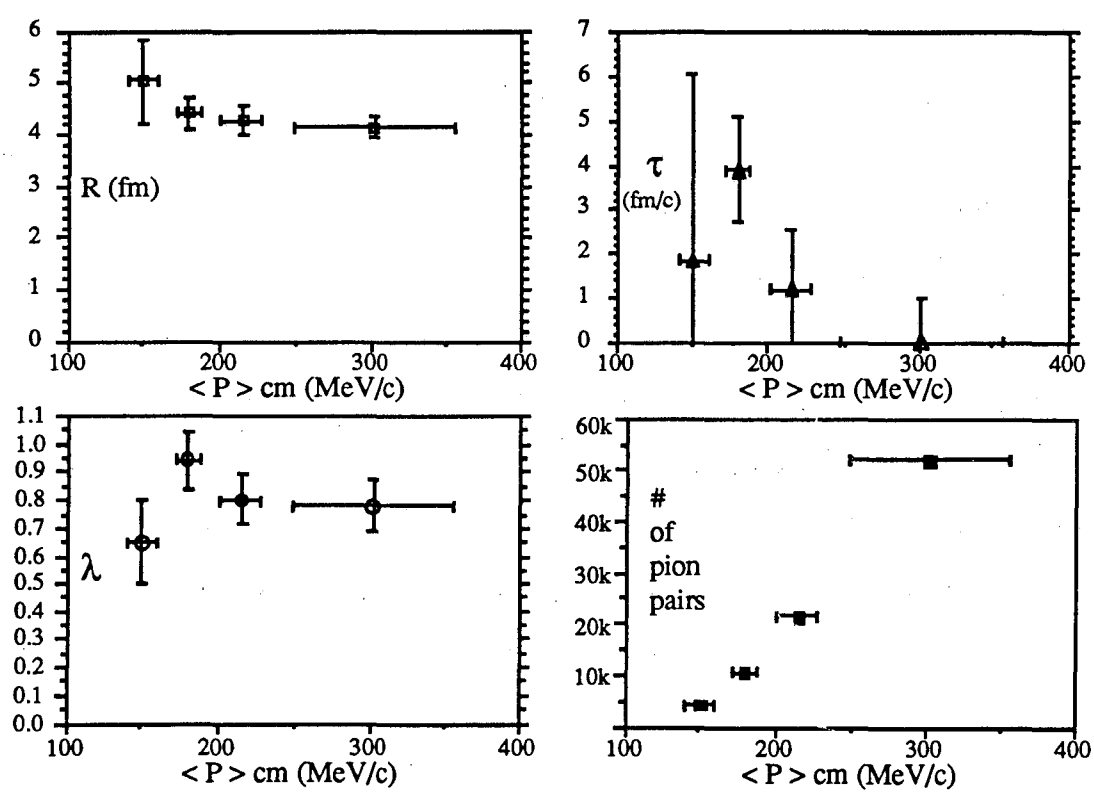

Figure #4.4 HBT parameters as a function of < P >.

In figure #4.4 I show the results obtained when I binned the pion pairs as a function of their mean summed momentum in the nucleus - nucleus cm frame. The requirement I imposed to determine the binning was that I get equal numbers of correlated π^- pairs with relative momentum (q) less than or equal to 50 MeV/c in each bin. I imposed this requirement in an attempt to get roughly equal sensitivity for the various HBT fit parameters in all the bins. The vertical error bars correspond to the one sigma errors in the HBT fits. The horizontal error bars correspond to the standard deviation for the distribution of the mean pion pair momentum within the bin.

The plots shown above are suggestive of the trend which Pratt predicts. If one believes that this effect is manifesting itself in the plots above, it appears that to investigate the effect one should design an experiment which has as low a cutoff in acceptance for pion momentum as possible. It is also clear that one needs very good statistics to pursue this type of study.

The apparent decrease in radius at a mean pion momentum of ≈ 150 MeV/c is very similar to results obtained for 1.5 GeV/ nucleon Ar on KCl data taken at the LBL streamer chamber by D. Beavis *et al*[3], although the magnitude of the effect we see is smaller than observed in their data. As pointed out in their paper, the decreasing of the extracted radius as a function of the pion momentum is consistent with a pion fireball model in which the temperature decreases as the source expands. It is also consistent with the picture in which the higher energy pions are produced directly in the earlier hard collisions while the lower energy pions are emitted at a later time from a thermalized fireball. In a later paper by the same group[6] for 1.8 GeV/ nucleon Ar on Pb this effect of a decreasing radius as one increases the mean value of the pion pair's momentum was also observed.

As a rough qualitative check of the data I've included Figure #4.5 to the right. Shown in the plot are the unnormalized inclusive π^- cross sections versus the kinetic energy of the pions in the cm frame, for three angles in the cm frame. The data is from the 1.8 GeV/nucleon Argon on KCl, central trigger data set. The cross sections shown have not been corrected with target out data. The error bars shown are just those due to statistics. The main feature to notice in this plot is the characteristic exponential fall off in the cross section as a function of the pions kinetic energy.

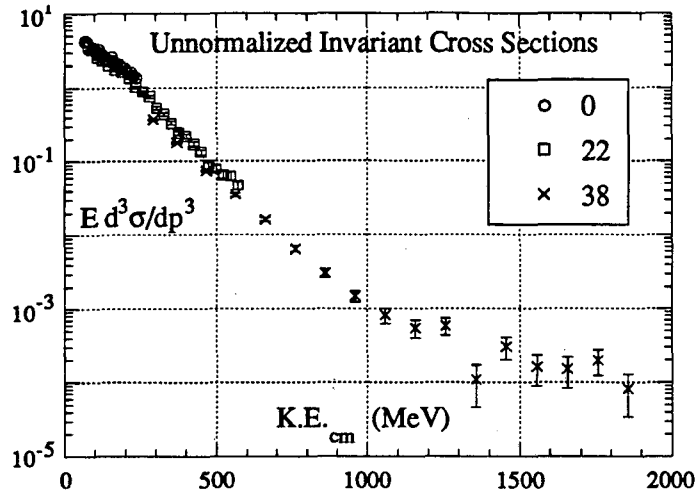

Figure #4.5 Unnormalized Invariant Cross sections.

For a slightly more quantitative evaluation of the inclusive π^- cross sections I've fitted a subset of the 22° cross sections to the following equation:

$$E\frac{d^3\sigma}{dp^3} = c\, e^{(-K.E._{cm}/E_0)} .$$

Figure #4.6 shows the fit line and the value extracted for what's commonly referred to as the slope parameter, E_0. This value compares very well with that seen by others. A. Shor *et al* [38]measured this slope parameter for π^- at 0° in the cm frame for 2.0 GeV/nucleon ^{28}Si on ^{28}Si, over a similar range of pion kinetic energy, and obtained the value $E_0 = 108 \pm 7$ MeV. S. Nagamiya *et al* [16]measured the slope

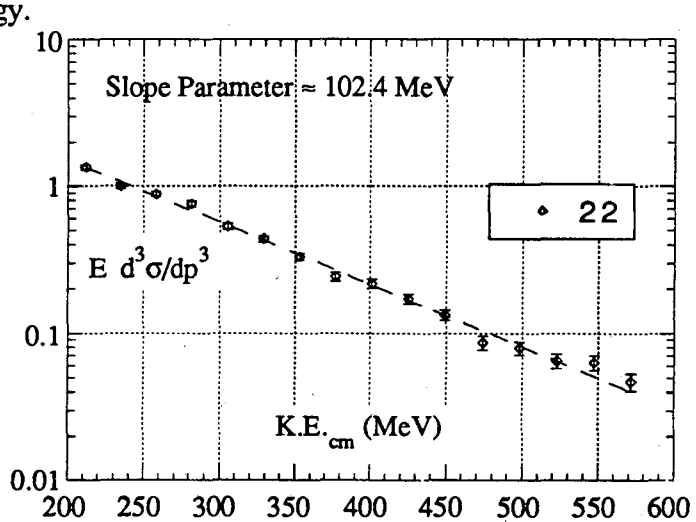

Figure #4.6 Slope parameter for data at 22°.

parameter for π^-s at 90° in the cm frame from 2.1 GeV/nucleon Ne on NaF. They obtained the value $E_0 \approx 102$ MeV. The only point I wish to make with the above plots, and the slope parameter measurement, is the qualitative agreement between the inclusive invariant cross sections measured by others and those from our data set.

Argon on Lanthanum

The data presented in this section was taken using the same central collision (Streamer Chamber Hard) trigger as the earlier section for the central Ar on KCl data. The cross section for satisfying this trigger, for this system, corresponds to ≈ 40% of the geometric cross section. We collected approximately eight 1600 bpi tapes of data for this configuration, each tape having about forty thousand events for a total of around 320,000 raw events. Out of these we ended up with about 12 to 13 thousand correlated pion pairs (depending on whether 10 or 20 MeV bins were used in the fit) and approximately 190,000 uncorrelated pairs, which made it past all the cuts and into the fitting routine.

There is an additional complication that comes into question for asymmetric colliding systems such as the Argon on Lanthanum presented in this section. For symmetric systems one knows that independent of the impact parameter for the collision, the interaction region, which is the source for the pions, will reside in the nucleon - nucleon center of mass (cm), and thus this is the natural reference frame in which to perform the HBT analysis. For asymmetric systems it is not so obvious in which frame to perform the analysis.

Beavis[6] *et al* have shown, using the Streamer Chamber at the BEVALAC, that for 1.8 GeV/n Argon on Lead, the velocity for the pion source ranges from the n - n cm frame for the lowest pion multiplicity events, to the minimum cm velocity expected (using a geometric model prediction for the number of target nucleons involved) for the highest pion multiplicity events.

Using the clean - cut geometric model for the collision, one may calculate the number of nucleons sheared off of the projectile and target nuclei as a function of the

impact parameter. With this information one may then calculate the center of mass velocity of the overlap region (assuming full stopping in the cm), which is the frame in which the HBT analysis is to be performed (i.e. the supposed rest frame of the pion source to be measured). I calculated this overlap region velocity for two different impact parameters. The two cases calculated are for impact parameters of zero and 2.1 fm. The 2.1 fm case corresponds to the maximum impact parameter such that the Argon nucleus is completely occluded by the Lanthanum nucleus (see figure #4.7).

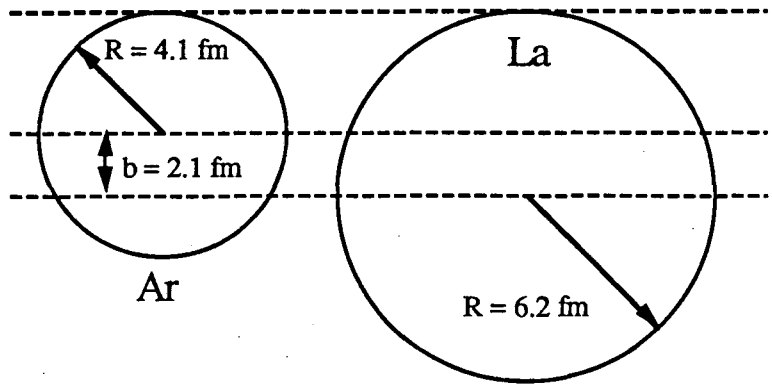

Figure #4.7 Ar on La, b = 2.1 fm

Table # 4.2 shows the results of these calculations.

Table #4.2 Possible center of mass frames for analysis

Impact Parameter b (fm)	Number of nucleons from Argon beam	Number of nucleons from La target	β_{cm} KE_{Ar} = 1.799 GeV/n
0	40	80	.5588
2.1	40	76	.5704
n - n cm			.7009

Notice the last row in the table above. I include this frame as this is clearly the upper limit on the velocity of the pion source in an asymmetric, light on heavy system at these energies. To see what effect this choice of frame has on the HBT analysis I transformed all the pions into the three frames and performed the fits. In figure #4.8 below I show the HBT fit parameters plotted versus the beta for the frame in which the analysis was performed. In all frames the lifetime parameter came out to zero. As a measure of what constitutes a

significant change in the parameters, the one σ uncertainty is shown for the data points from the fit in the frame with β equal to .5704.

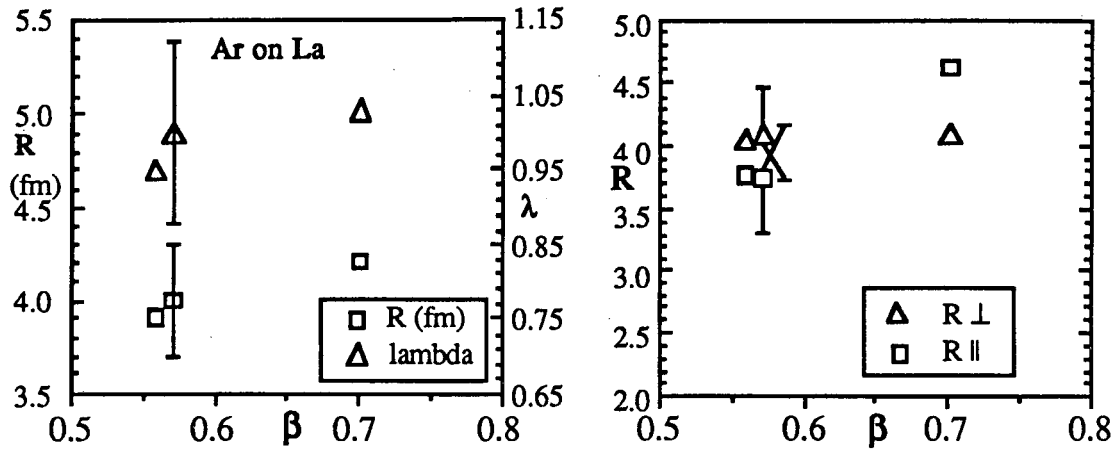

Figure #4.8 HBT parameters vs β of assumed cm frame.

As shown in the figure above, within the reasonable range of rest frames for this experiment, the variations in the parameters R and λ are all within one σ of one another. Note also that in all frames the transverse radius is the same, as one would expect for boosts in the parallel direction.

One expects the combination of our central collision trigger, and the requirement that all events in the analysis have at least two π^- within the spectrometers acceptance, to heavily bias the events toward those with a small impact parameter. On this basis I believe that the true average rest frame for the pion source is probably in the range of $.5588 \leq \beta_{cm} < .6$. As the dependence of the fit parameters on the choice of frame is small (relative to the uncertainties) in this region, and a choice must be made, all fits for the Ar on La will be performed in the frame with βcm equal to .5704. The results are listed in the table below.

Table #4.3 1.8 GeV*A Argon on La					
Systematic Corrections Applied	DC eff.		X	X	X
	Gamow			X	X
	Background				X
R (fm)		4.01		4.11± .28	3.88± .28
τ (fm/c)		0.0		0.0± 1.0	0.0± 1.0
λ		.80		1.02± .12	1.05± .13
$\frac{\chi 2}{NDF}$		$\frac{186.2}{178}$		$\frac{191.0}{178}$	$\frac{193.3}{178}$
Pr ($\chi 2 \geq \chi 2_{meas.}$)		.26		.16	.12
Volume measured (fm^3)				1021± 209	859± 186
Volume at NND (A=116) / Volume measured				0.82± .17	0.98± .21
12,293 Correlated π^- pairs, 191,640 Uncorrelated π^- pairs.					
$R_\perp$ (fm)		3.83	3.84	4.10± .38	
$R_{//}$ (fm)		3.87	3.88	3.74± .43	
$\lambda_{\perp //}$		.75	.76	.98± .12	
$\frac{\chi 2}{NDF}$		$\frac{338.8}{347}$	$\frac{337.3}{347}$	$\frac{338.5}{347}$	
Pr ($\chi 2 \geq \chi 2_{meas.}$)		.34	.31	.33	
Volume measured (fm^3)				925± 202	
Volume at NND (A=116) / Volume measured				0.91± .20	
13,104 Correlated π^- pairs, 203,290 Uncorrelated π^- pairs.					
$R_\perp$ (fm)		4.60		4.82± .45	4.63± .40
$R_{//}$ (fm)		3.88		3.80± .53	3.82± .50
τ (fm/c)		0.0		0.0± 1.90	0.0± 2.0
λ		.82		1.06± .13	1.10± .14
$\frac{\chi 2}{NDF}$		$\frac{564.0}{548}$		$\frac{562.3}{548}$	$\frac{559.5}{548}$
Pr ($\chi 2 \geq \chi 2_{meas.}$)		.24		.26	.30
Volume measured (fm^3)				1299± 303	1205± 261
Volume at NND (A=116) / Volume measured				0.65± .15	0.70± .15
9485 Uncorrelated π^- pairs, 138,710 Uncorrelated π^- pairs.					

Xenon on Lanthanum

In this section the results are presented for a 1.2 GeV/nucleon Xenon beam incident on a Lanthanum target. This set of data was taken using the central collision (SCH) trigger. The cross section for satisfying this trigger, for this system, corresponds to ≈ 37% of the geometric cross section. We filled nine 1600 bpi magnetic tapes for this beam - target - trigger combination, each tape containing approximately 35,000 events for a total of ≈ 320,000 raw events. Out of these events we ended up with about 10,000 correlated π^- pairs which passed all the cuts and made it into the HBT analysis. The results are listed in table #4.4 below.

Table #4.4 1.2 GeV*A Xenon on La					
Systematic Corrections Applied	DC eff.		X	X	X
	Gamow			X	X
	Background				X
R (fm)		5.15	5.20	5.40± .8	4.90± .75
τ (fm/c)		4.60	4.80	$3.60\pm^{2.2}_{3.6}$	$3.44\pm^{1.9}_{3.4}$
λ		.53	.57	.80± .19	.76± .17
$\frac{\chi 2}{NDF}$		$\frac{218.1}{158}$	$\frac{216.3}{158}$	$\frac{218.1}{158}$	$\frac{220.25}{158}$
Volume measured (fm^3)				2316± 1029	1731± 795
Volume at NND / Volume measured				0.84± .37	1.13± .52
Pr ($\chi 2 \geq \chi 2_{meas.}$)		5×10^{-6}	8×10^{-6}	5×10^{-6}	2×10^{-6}
10,241 Correlated π^- pairs, 162,280 Uncorrelated π^- pairs.					
$R_\perp$ (fm)		4.51	4.61	4.99	
$R_{//}$ (fm)		7.89	7.87	7.09	
$\lambda_{\perp //}$		.55	.59	.82	
$\frac{\chi 2}{NDF}$		$\frac{302.2}{231}$	$\frac{301.4}{231}$	$\frac{302.6}{231}$	
Pr ($\chi 2 \geq \chi 2_{meas.}$)		5×10^{-6}	6×10^{-6}	5×10^{-6}	
Volume measured (fm^3)				2597	
Volume at NND / Volume measured				.75	
10,217 Correlated π^- pairs, 160,850 Uncorrelated π^- pairs.					
$R_\perp$ (fm)		5.11	5.17	5.56± .63	5.40± .65
$R_{//}$ (fm)		8.75	8.70	7.94± 1.5	7.70± 1.40
τ (fm/c)		0.0	0.0	0.0+ 3.60	0.0+ 3.60
λ		.60	.64	.90± .18	.91± .18
$\frac{\chi 2}{NDF}$		$\frac{45.8}{394}$	$\frac{454.9}{394}$	$\frac{451.8}{394}$	$\frac{450.0}{394}$
Pr ($\chi 2 \geq \chi 2_{meas.}$)		1.2 x 10-3	1.4 x 10-3	2.3 x 10-3	3.0 x 10-3
Volume measured (fm^3)				3611± 1065	3303± 996
Volume at NND / Volume measured				.54± .16	.59± .18
8,155 Uncorrelated π^- pairs, 123,720 Uncorrelated π^- pairs.					

There are a few features I'd like to point out to the reader in the table above. The first point is the rather large (relative to the previous data sets) value for the lifetime parameter τ in the standard R, τ, λ fit. As is the case with every fit performed in this experiment, however, due to the large error on τ it is still consistent with zero. In the second and third cases presented in the table one sees that, given the freedom, the fits return a large value for the parallel radius and again return lifetime parameters of zero. Whereas the fit source shapes for both the Ar on KCl and the Ar on La were oblate, the Xe on La results above indicate a prolate ($R_{//} > R_{\perp}$) pion source. I'll discuss this further in the next chapter.

Peripheral Collision Data

Argon on KCl

This section contains the results for the Ar on KCl data taken with the Streamer Chamber Soft (SCS) trigger. The trigger is described in detail in the trigger section at the end of chapter #2. The cross section for satisfying this trigger, for this system, corresponds to ≈ 67% of the geometric cross section.

Our goal with this trigger was to see if we could show a direct correlation between the impact parameter of the collision, as deduced from the charge of the leading projectile fragment, and the extracted HBT radius parameter. We collected ten 1600 bpi tapes with this trigger, each tape containing approximately 50,000 events for a total of ≈ 500,000 raw events. Out of these events we ended up with ≈ 17,400 correlated π^- pairs.

As one would expect with a trigger of this sort, when one imposes the requirement that an event must have two negative pions within our experimental acceptance there is a heavy biasing toward central events. This effect can be seen in figure #4.9 which shows a histogram of the signal in the Cherenkov (V_4) radiator used in the trigger for various cuts on the minimum number of π^- observed.

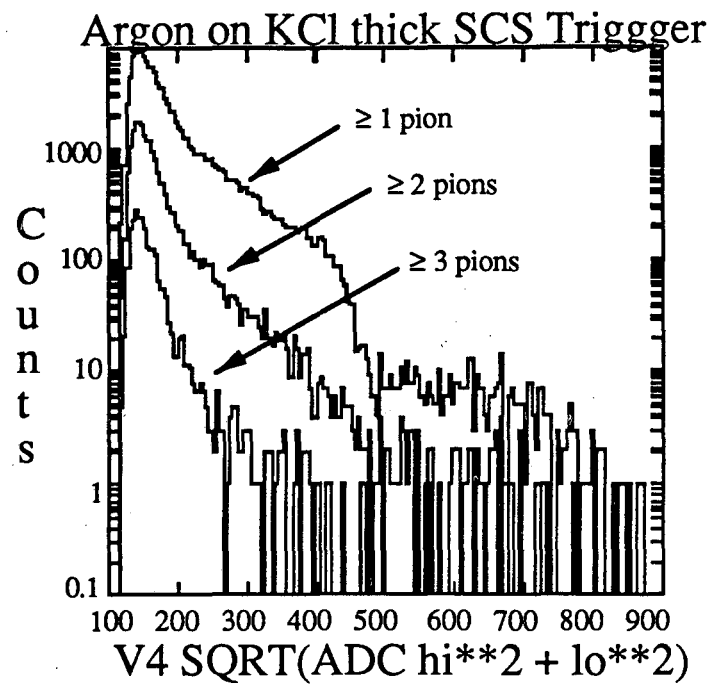

Figure #4.9 V_4 ADC versus number of π^- observed.

The table of results for this beam - target - trigger combination is organized a little differently than the previous three sections. I again show the results of fits to the three forms of the correlation function listed at the start of this chapter, but the results are also given for three different requirements on the maximum projectile charge (Z_{max}, calculated from the ADC signals) observed in the Black TOF wall (placed to detect projectile fragments, see figure #2.1). The requirements are this quantity, Z_{max}, be between zero and thirteen (i.e. no cut), zero and one and a half, and between one and a half and thirteen. Figure #4.10 shows a histogram of Z_{max} in the Black Wall for a portion of the data in which the events contain at least two π^-s. The cut on Z_{max} is represented by the dashed line. The criteria I used to determine the placement of this cut was that there be approximately equal numbers of correlated π^- pairs above and below the cut.

I must emphasize a few points with regard to this cut on Z_{max}. With the voltages we ran on the Black Wall I was only able to discern charges down to Z = 4 in the calibration data for the individual BW slats. This is illustrated by the sharp drop shown in figure #4.10 at charge four.

Below this point the ADC signals ($\sqrt{ADC_{top} * ADC_{bot}}$) for a given slat smeared together into a more or less uniform density spectrum which showed an increase as the ADC signal decreased, generally characteristic of what one observes in a noise spectrum. As a coincidence is required between the ADC signals received from the top and bottom of a given slat, this rise is not a usual noise spectrum.

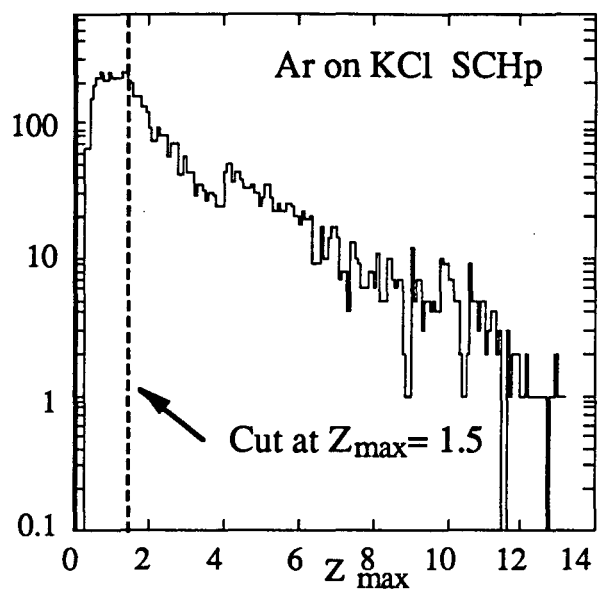

Figure #4.10 Histogram of Zmax for SCS trigger

I believe the explanation for this distribution is that the signals from the photomultiplier tubes are so small in this region that whether or not both ADCs show a signal (ADC value above digital threshold in LeCroy 2280 system) depends on how close to the center (vertically) of the slat the charge one or two nuclei (nucleus) hit the slat. What this means, unfortunately, is that in the region of the spectrum where I'm applying the cut the selection is, to a large extent, not on some physically characteristic parameter for the event, but rather on a more or less random signal. If I require that Z_{max} be greater than or equal to four I end up with only ≈ 2,700 correlated π^- pairs.

For the results shown in the table, bin widths of 10 MeV/c (MeV) were used in the first set of fits (R,τ, λ) and widths of 20 were used in the other two sets of fits. The DC

efficiency and Gamow corrections are applied in all the fits shown. The background correlation correction is not applied.

Table #4.5 1.8 GeV*A Argon on KCl SCS			
Part of Soft trigger Data	ALL	LOW	HIGH
Cut on Z_{max} in Black Wall	Z = 0 - 13	Z = 0 - 1.5	Z = 1.5 - 13
R (fm)	4.55± .35	4.83 ± .48	4.30 ± .48
τ (fm/c)	0 + 2.0	0 + 2.8	0 + 2.8
λ	.68 ± .1	.70 ± .15	.65 ± .14
$\frac{\chi 2}{NDF}$	$\frac{590.4}{606}$	$\frac{535.6}{479}$	$\frac{382.5}{428}$
Pr ($\chi 2 \geq \chi 2_{meas.}$)	.27	.005	.012
Number of Correlated π^- pairs	17,428	8,822	7,484
$R_\perp$ (fm)	5.21 ± .45	5.93 ± .60	4.21 ± .45
$R_{//}$ (fm)	3.81 ± .53	3.87 ± .70	3.03 ± .65
$\lambda_{\perp //}$	.72 ± .11	.88 ± .19	.60 ± .12
$\frac{\chi 2}{NDF}$	$\frac{847.96}{776}$	$\frac{336.3}{280}$	$\frac{253.01}{253}$
Pr ($\chi 2 \geq \chi 2_{meas.}$)	.005	6×10^{-4}	.49
Number of Correlated π^- pairs	16,776	9,619	8,227
$R_\perp$ (fm)	5.01 ± .45	5.72 ±.7	4.75 ± .50
$R_{//}$ (fm)	$2.12^{+1.08}_{-2.12}$	$.90^{+3.10}_{-.90}$	$2.41^{+.8}_{-1.2}$
τ (fm/c)	$3.93^{+1.47}_{-1.93}$	$4.33^{+1.1}_{-4.33}$	0 +2.40
λ	$.71^{+.10}_{-.06}$	$.80^{+.20}_{-.14}$	$.58^{+.14}_{-.10}$
$\frac{\chi 2}{NDF}$	$\frac{833.76}{713}$	$\frac{516.6}{431}$	$\frac{391.4}{366}$
Pr ($\chi 2 \geq \chi 2_{meas.}$)	6×10^{-6}	4×10^{-5}	.09
Number of Correlated π^- pairs	14,646	6,721	5,730

Keeping in mind the point made above on the dubious validity of the cut made on Z_{max}, the results shown in the table exhibit the trends which one would expect. The fit value for the standard radius parameter R is largest for the low cut on Z_{max}, smallest for the high cut on Z_{max}, and in between the high and low when no cut is made on Z_{max}. This

behavior is also shown in the perpendicular ($R_{\perp}$) and parallel ($R_{//}$) radius parameters, although for the parallel radius parameters in particular the errors are large.

While I can't make a definitive statement based on this peripheral collision data that I see a correlation between the leading fragment ($\propto$ impact parameter) and the extracted radius of the pion source, due to the problems with the cut on Z_{max} and the fact that the radii are almost all within one standard deviation of one another, the clear trends in the results are highly suggestive that this correlation exists. I believe that a data set of this type could answer this question if one either acquired a very large data sample with a similar trigger, or devised a trigger which contained a two pion requirement in addition to a selection on the leading fragment charge. My personal preference would be for the latter.

Chapter 5. Discussion

General

Up to this point we've shown that there is an enhancement in the two pion cross section for pions which are close to one another in phase space. We've also shown that if one makes the assumption that the pion emitting sources are Gaussian in space and time (the time part to a lesser degree as this analysis technique is not sensitive to the lifetime parameter) we get a very good fit to the shape of the theoretical correlation function, and for this data set we can extract fairly precise values for the HBT fit parameters. The question which remains is, what is it that we've measured to such precision? While this question is one which should rightly be investigated by theorists, I will present here some simple geometric arguments for the size and the lifetime of the system which set the scales that one would expect.

I'll discuss the three types of fit parameters separately, beginning with the spatial and ending with the chaoticity parameter, λ.

For the spatial parameter, R, the natural quantities with which to compare are the geometric size of the projectile nucleus and of the participant region in the nucleus - nucleus collision. The geometric size of an equivalent sharp - sphere nucleus can be easily calculated :

$$R\ (\mathrm{fm}) = r_0\ A^{1/3}$$

where $r_0 = 1.2$ fm. For the Argon nucleus (A = 40) this gives R = 4.10 fm. If one assumes that one has full stopping of the projectile in the projectile - target center of mass system, that the impact parameter is zero, and that the compound system is at normal nuclear density (almost certainly incorrect as one expects some increase in density in the early stage of the collision, followed by an expansion), the size of the interaction region (IR) (assuming an impact parameter of zero, A = 80) can be calculated with the formula above. This gives a size of 5.17 fm. To compare the radii which we've extracted using the theoretical

framework of Yano and Koonin[25] to the equivalent sharp sphere radii given by the simple formula above, one must multiply by a conversion factor of 1.52. This conversion factor is discussed in appendix A. In table #5.1 below I've listed some of these values for the data from this study. The last column gives the ratio of the calculated interaction region volume at normal nuclear density to the volume which one gets using our extracted radii. Spherical source shapes are assumed in the calculations below.

Table #5.1

A_{beam}	A_{target}	$R_{beam} = 1.2\ A_{beam}^{1/3}$ (fm)	A_{IR}	$R_{IR} = 1.2\ A_{IR}^{1/3}$ (fm)	R_{Fit} (fm)	$1.52\ R_{Fit}$ (fm)	$\frac{R_{IR}^3}{(1.52\ R_{Fit})^3}$ (%)
40	40	4.10	80	5.17	4.30	6.54	38
40	139	4.10	116	5.85	3.88	5.90	97
132	139	6.11	271	7.76	4.90	7.75	113

One observation that is generally true for all the experimental results using two particle interferometry to measure source sizes in RHIC is that the radii one measures are always greater than the radii of the colliding system. In the table above, where a spherical source shape has been assumed, this is only true for the Ar on KCl data set. The explanation for this observation is that the correlations which one measures in the relative momentum and energy of the particles, in this case pions, are those that exist after the last rescattering of the particles as they escape from the interaction region. The density which one calculates using the measured HBT spatial parameters and a measured or assumed number of nucleons participating in the collision is thus commonly referred to as the *freeze out* density for the particular particle used for the interferometry analysis. If this argument is correct then one of the consequences one expects is that the larger the scattering cross section for the particle used in the analysis with the participant nucleons (π^-N in this case), the later in time that the particles have their last rescattering, and, assuming an expanding

interaction region, the larger the radius one will measure. Thus, as $\sigma(\pi^- N) \approx 100$ mb > $\sigma(NN) \approx 40$ mb > $\sigma(K^+N) \approx 10$ mb, one expects to be able to probe different temporal stages of the collision by using different particles in the analysis. The pion interferometry yielding information on the later, cooler stages of an expanding system.

The measured values of the radius parameter given in the table above were for the standard R,τ, λ fits to the data. Implicit in this fit is the assumption that one has a spherical source shape. In figure #5.1 to the right I show the freeze out densities one obtains using the volume of the spheroid defined by the fit values for $R_\perp$ and $R_{//}$ as given in the last set of fit parameters in the results tables for the three central collision data sets. The errors assigned to the points in the plot are merely the errors calculated for the volumes given the errors for the radius parameters. The same assumptions were made for the number of participant nucleons as given in table #5.1 above. As the assumed values for the numbers of participating nucleons correspond to the maximum possible for the symmetric systems, and essentially the maximum possible for the Ar on La, these densities shown above are more correctly interpreted as upper limits. With the errors as shown, and the assumptions made for the number of participant nucleons, there does not appear to be any dependence of the freeze out density on the size of the colliding system. This is consistent with what one would expect from the simple rescattering argument given earlier. If it is indeed true that the freeze out density measured via the HBT analysis is independent of the mass of the colliding system, one could argue that the HBT technique measures the size of

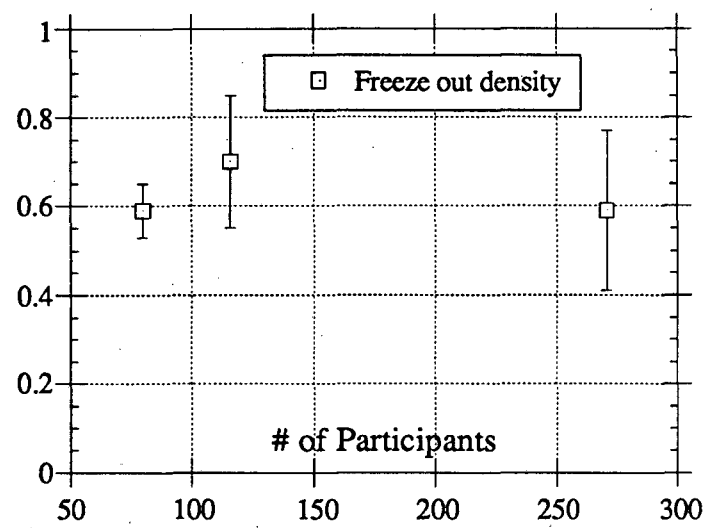

Figure #5.1 Freeze out Densities.

the systems at the same point in the evolution of the participant regions of the collisions. This would support the interpretation of the spatial HBT parameters as actually being a useful measure of the spatial distribution of the pion source.

As mentioned in the discussion above, none of the source shapes measured in this experiment is spherical (within one sigma), although the Argon on Lanthanum source is very close. In figure #5.2 I show the perpendicular and parallel radii for the three central collision data sets. What's shown on the plot are the one σ error contours for the three systems. The dashed 45° line is for reference purposes and corresponds to $R_{\perp}$ equal to $R_{//}$. The first feature I'd like to point out is that the errors in $R_{\perp}$ and $R_{//}$ are essentially uncorrelated, as the axes of the error contours are parallel to the coordinate axes. The next feature to notice is that the uncertainty in $R_{//}$ is larger than the uncertainty in $R_{\perp}$. This is as one would expect for a study at zero degrees in the cm frame. The next feature to note is the very slight dependence of the perpendicular radii on the size of the colliding system. For the Ar on KCl and Ar on La data this could be interpreted as an indication that the size of the projectile is the determining factor for the size of the pion source as determined via HBT analyses. What is perhaps surprising is that the perpendicular radius measured for the Xe on La system is only slightly larger than that for Ar on KCl. Finally, notice that whereas the source shapes for the Ar on KCl and Ar on La are oblate in the cm frame, the source shape as measured for the Xe on La system is prolate. I do not know of any arguments that would explain this effect. It would be interesting to obtain a more precise measurement for a large mass system to see if this transition from oblate to prolate source shapes is correct.

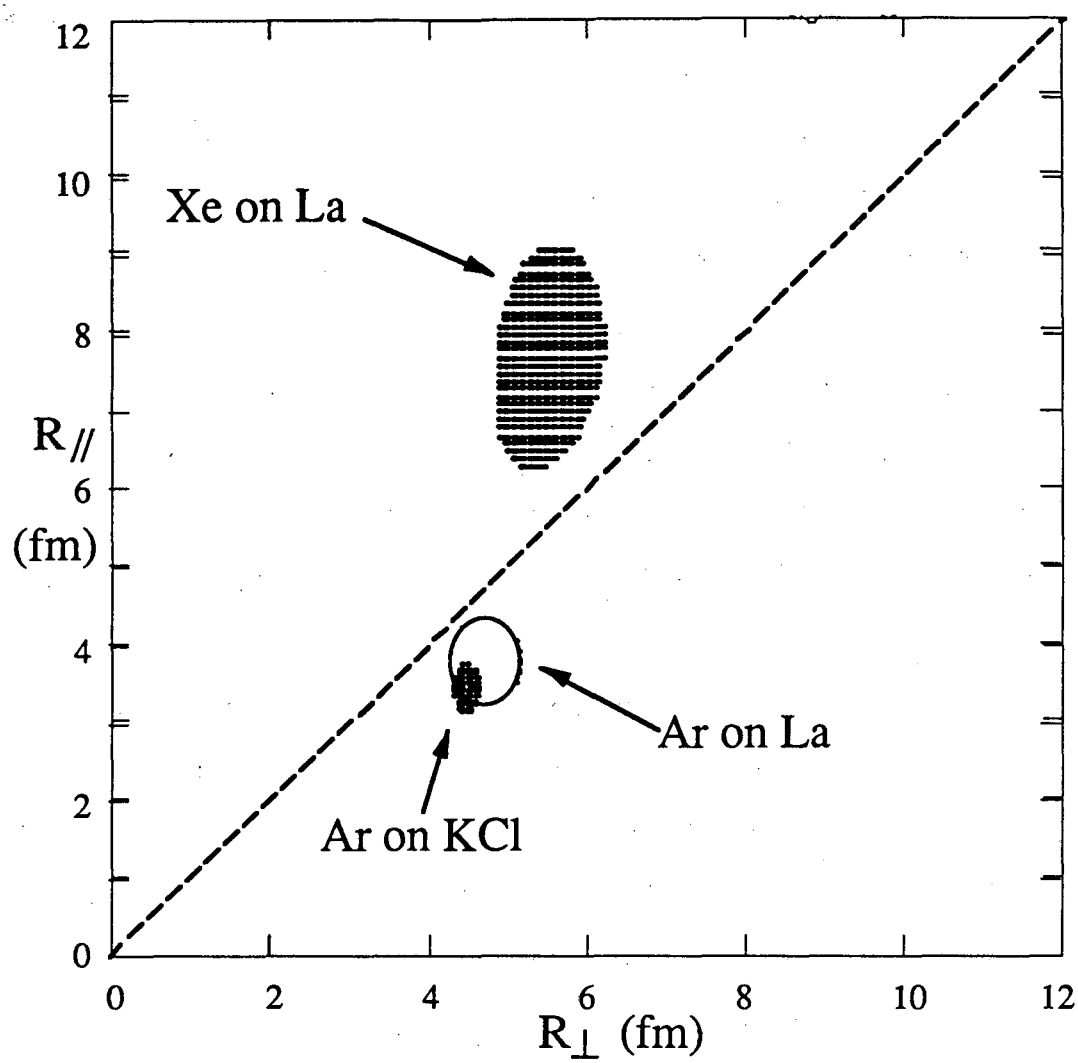

Figure #5.2 $R_\perp$ vs $R_{//}$ for Central Collision data.

Moving on to the lifetime parameter, τ, the main feature which shows up in the data, for all the fits, is that the fit is very insensitive to τ. The insensitivity of the fit to the value of τ is consistent with what Yano and Koonin[25] projected in their theoretical formulation. This insensitivity is clearly seen by looking at the errors given for τ in the results tables.

Another prevailing feature of the lifetime parameter is that in all cases presented in this thesis the errors were such that if the fit value of τ wasn't identically equal to zero, the errors on the parameter were such that within one σ all the measured values of τ were consistent with zero. Due to the large phase space acceptance of the HISS spectrometer

setup used in this study the determination of the lifetime parameter was largely uncoupled from the other fit parameters. The parameter which showed the largest coupling to τ was the parallel radius. This coupling between the parallel radius, which is a function of the relative parallel momentum (P_z), and τ, which is a function of the relative energy of the π^- pairs, is to be expected in pion interferometry at angles close to 0° in the cm system, as is the case in this experiment, due to the tight correlation between parallel momentum and energy. This is seen most dramatically by looking at the results table for the Xe on La data set. In the standard fit to R, τ, λ, which implicitly assumes that $R_\perp$ is equal to $R_{//}$, the fit returned a non - zero value for τ. Given the freedom to fit both spatial components of the radius in addition to the lifetime the fit returned a value of zero for τ and a non zero value for $R_{//}$.

The usual interpretation of the lifetime parameter is that it is a measure of the time over which the pions are emitted. If one was to apply this interpretation to the results presented here one would conclude that the pions all escape from the pion source instantaneously. This is not the conclusion I draw from the results. I merely conclude that as predicted this type of analysis is insensitive to the lifetime parameter.

This brings us to the chaoticity parameter λ. Recall that this parameter was introduced into the fit because experimentally it was observed that the value of the correlation function rarely reached the expected value of two as the relative momentum and energy of the pion pairs went towards zero. The historical interpretation of this parameter has been that it allows for a decrease in the magnitude of the two pion enhancement due to partial coherence of the emitted pions as well as other correlations imposed on the pions.

Assuming that one has correctly accounted and corrected for all kinematic and dynamic correlations in the single and double pion distributions, it has been theorized that the subsequent value of the chaoticity parameter may give a measure of the degree of coherence of the pion source. As given in reference #26, one finds that:

$$C_2(\mathbf{k}, \mathbf{k}) = 2 - (D(\mathbf{k}))^2$$

where **k** is the wave number for the pions (both about equal). This function D(**k**) is related to the number of coherent and chaotic pions via:

$$D(\mathbf{k}) = \frac{n_0(\mathbf{k})}{n_0(\mathbf{k}) + n_{ch}(\mathbf{k})}$$

where n_0 are the number of coherent pions and n_{ch} are the number of chaotic pions with wave number **k**. If I use the value obtained for λ in the fits to the central Ar on KCl data ($\lambda \approx .75$), and solve for the ratio of coherent to chaotic pions using the formulism above I end up with the result that the number of chaotic and coherent pions are approximately equal. As the value for λ obtained from the fit to the asymmetric, Ar on La data is approximately equal to one, the above assumptions and equations would say that all the pions in this data set are from a chaotic source.

The one of the same authors as I've referenced for the arguments given above, in a subsequent paper[34], emphasized that unless one has an exclusive data set, and hence can eliminate the averaging over unobserved final states inherent in inclusive measurements, any interpretation one makes of the λ parameter will be suspect at best. One of the examples given of these "ensemble correlations" is the shadowing of the pions, as a function of their angle of emission in the reaction plane of the collision, due to any target or projectile spectator matter.

Another reason that one should be careful in interpreting the λ parameter as having physical significance is the large effect which the Gamow correction has on λ, and therefore the faith that one must put in the correction.

With the use of the new electronic 4π detectors currently being designed and constructed for the study of RHIC, specifically the HISS Time Projection Chamber and the 4π detector at SIS, one will be better able to investigate and try to answer the question of the degree of coherence of the pion emitting source. In the data set and fits I present here the only comment I'd like to make on this parameter is to point out that for both the

symmetric data sets (Ar on KCl and Xe on La) the value of this parameter is less than one, whereas for the asymmetric data set (Ar on La) the value is about equal to one.

Comparison with Results of others

Comparing the results obtained here with other pion interferometry experiments is facilitated by the compilation of results in this field published by J. Bartke[47]. In table #5.2 below I've reproduced most of Bartke's list and added some recent results of D. Chacon *et al*[48] and the results of this thesis[49]. To make a comparison of the extracted radii meaningful, Bartke has tabulated all the necessary conversion factors which one must apply, depending on the experimenter's choice of the theoretical framework to follow and the source distribution to use. All of the radius values in the table have been converted to the root - mean - square (rms) values.

Ap	At	E/A (GeV)	Selection	RMS radius (fm)	Detector	Ref.
p	H	200	all inel.	1.66 ± 0.04	str. chamber	51
p	Xe	200	all inel.	1.53 ± 0.13	str. chamber	51
p	Xe	200	$n_{ch} > 20$	1.45 ± 0.11	str. chamber	51
d	Ta	3.4	all inel.	2.20 ± 0.50	bub. chamber	52
^{4}He	Ta	3.4	all inel.	2.90 ± 0.40	bub. chamber	52
^{12}C	C	3.4	all inel.	2.75 ± 0.76	bub. chamber	53
^{12}C	C	3.4	"central"	3.76 ± 0.88	bub. chamber	53
^{12}C	Ta	3.4	all inel.	3.40 ± 0.30	bub. chamber	52
^{20}Ne	NaF	1.8	all inel.	$2.24^{+0.98}_{-1.96}$	magn. spectr.	54
^{40}Ar	KCl	1.8	all inel.	$3.53^{+0.61}_{-1.10}$	magn. spectr.	31
^{40}Ar	KCl	1.8	all inel.	2.3 ± 0.6	magn. spectr.	50
40Ar	KCl	1.8	"soft"		magn. spectr.	E684H
^{40}Ar	KCl	1.8	"central"	5.27 ± 0.17	magn. spectr.	E684H
^{40}Ar	KCl	1.5	"central"	6.04 ± 0.54	str. chamber	3
^{40}Ar	KCl	1.2	"central"	4.65 ± 0.61	str. chamber	5
^{40}Ar	BaI_2	1.8	all inel.	3.74 ± 1.35	str. chamber	1
^{40}Ar	La	1.8	"central"	4.75 ± 0.34	magn. spectr.	E684H
^{40}Ar	Pb_3O_4	1.8	all inel.	4.04 ± 1.14	str. chamber	1
^{40}Ar	Pb_3O_4	1.8	"central"	4.87 ± 0.96	str. chamber	1
^{56}Fe	Fe	1.7	all inel.	2.5 ± 0.6	magn. spectr.	50
^{84}Kr	RbBr	1.2	all inel.	6.61 ± 1.47	str. chamber	55
^{92}Nb	Nb	1.5	all inel.	$4.8 \pm .1$	magn. spectr.	50
^{132}Xe	La	1.2	"central"	6.00 ± 0.92	magn. spectr.	E684H

Table #5.2 Comparison with results of others.

For the results presented in this thesis the appropriate conversion factor is $\sqrt{3/2}$ (i.e. multiply values from the results tables given earlier by $\sqrt{3/2}$ This conversion factor is discussed in appendix A). In figure #5.3 below I've plotted the values from table #5.2 in essentially the same format as that used by Bartke. The dashed line shown on the plot corresponds to what Bartke refers to as the "effective nuclear radius" and was derived from

a series of inelastic (interaction) cross section measurements for various nuclei[55]. The data points for Carbon and Argon have been spread out a bit to separate the points. The arrow on the x axis points to the appropriate position for Argon.

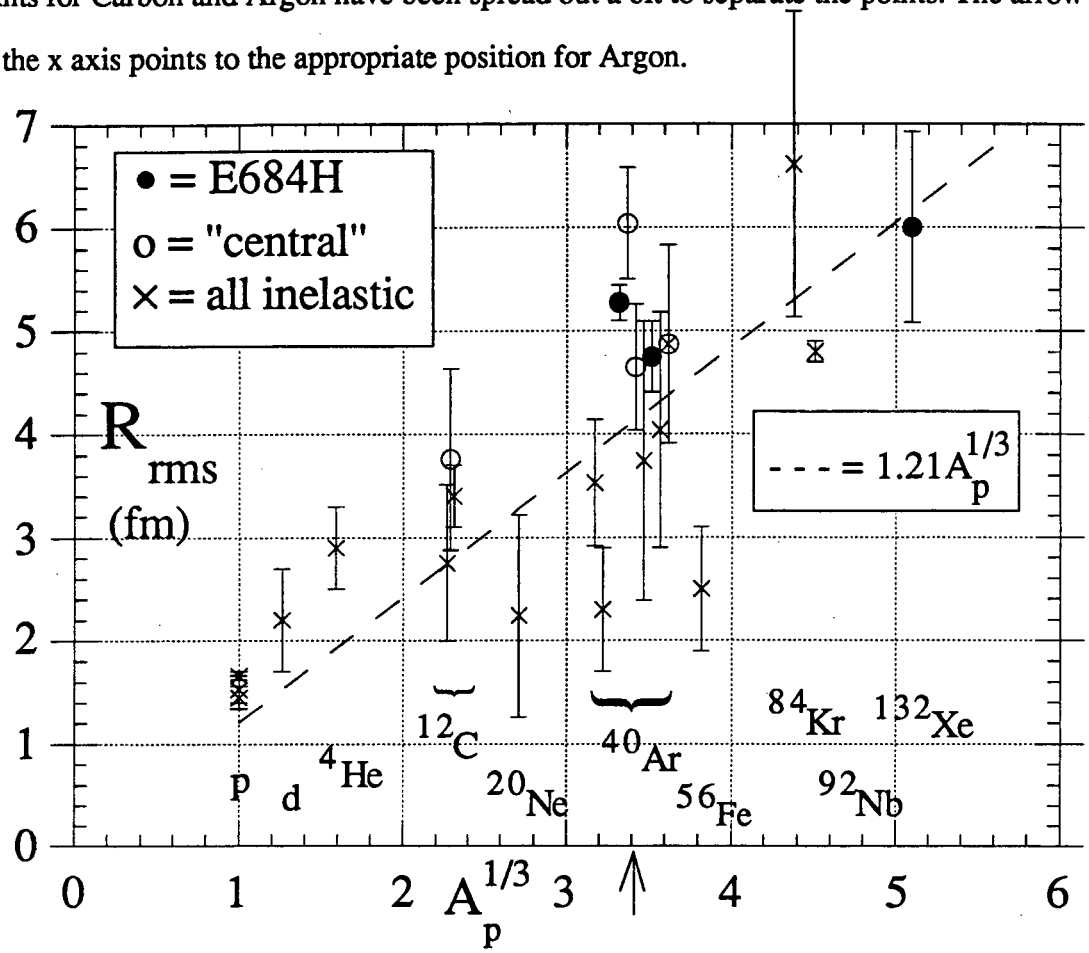

Figure #5.3 Comparison with results of others.

I don't understand why Bartke choose to convert the data points to their rms values instead of to their equivalent sharp sphere values. It seems as though the latter would be more appropriate to compare to the line in the plot. However, regardless of the multiplicative factor which one chooses to multiply the data, the data points do appear to exhibit a scaling with $A_p^{1/3}$.

As shown earlier, the extracted pion source shapes do not appear to be spherical, thus it is interesting to compare the source shapes with those measured by others. Bartke states that, in general, the source shapes extracted in hadron - hadron collisions appear to be oblate. There are only five results that I'm aware of in nucleus - nucleus collisions where

the shape of the source has been investigated. D. Beavis and the Riverside group[3] extracted a spherical source shape for 1.5 GeV/A Argon on KCl in their studies using the LBL streamer chamber. The uncertainties on their extracted radii were large however ($R_\perp = 5.03 \pm 0.47$ fm, $R_{//} = 5.11 \pm 1.17$ fm) and, within these uncertainties, their results agree with those presented here. The same group also investigated[6] the source shape for 1.8 GeV/A Argon on Lead and extracted radii that were spherical ($R_\perp = 5.67 \pm 0.54$ fm, $R_{//} = 5.16 \pm 0.50$ fm) within uncertainties.

D. Chacon[49] *et al* extracted an oblate source shape for 1.7 GeV/A Fe on Fe. More recently, the same group[50] have done a source shape analysis for 1.8 GeV/A Argon on KCl, at 0°, using the JANUS spectrometer at the BEVALAC. Their results ($R_\perp = 4.8 \pm 0.3 \pm 0.07$ fm, $R_{//} = 4.2 \pm 0.4 \pm 0.2$ fm, $\tau = 1.1^{+1.4}_{-1.1} \pm 0.4$, $\lambda = 0.81 \pm 0.05 \pm 0.03$) agree within uncertainties with those presented here in all four fit parameters! In the same paper they give results for 1.54 GeV/A ^{93}Nb on Nb in which they extracted a spherical source shape.

Conclusions

I believe we have accomplished the two main goals of this experiment as stated back in the introduction. These goals were to initiate the use of the HISS facility in the study of central Relativistic Heavy Ion Collisions, and to perform a second generation experiment for the detailed study of the pion source in RHIC, to complement the earlier work done in this field.

The HISS facility is well suited to pion correlation studies. Its relatively high data taking rate allows one to obtain more precise values for the pion correlation fit parameters than possible using visual detectors such as the earlier streamer chamber work done by the Riverside group and others. The large phase space acceptance of the HISS system uncouples the determination of the HBT fit parameters and reduces the size of any acceptance related correlations in ones background pion pair distribution.

This was the first experiment analyzed using the large 2 m × 1.5 m HISS drift chambers. The tracking software has been tuned to optimize the tracking of multiple particles as well as finding spatially close pairs of tracks, which is important if one wishes to pursue the type of particle correlation analysis presented in this thesis. The efficiency of the Drift Chamber for finding these close pairs of tracks, due to both the hardware and the software, has been characterized and, while corrected for in the analysis, shown to have a negligible affect on the results presented here.

The results obtained for Argon on KCl are more precise than any yet published for this well studied system. The results presented here for Xenon on Lanthanum represent the heaviest system yet studied using pion correlations. While the results of the data set taken with the peripheral collision trigger do not allow me to make a conclusive statement about the correlation between the size of the leading projectile fragment and the extracted size of the pion source, the results clearly show the trend which one expects (the smaller the projectile fragment the larger the size of the pion source). The source shapes extracted are oblate for the Argon on KCl and Lanthanum data, and prolate for the Xenon on Lanthanum data.

Future Work

The HISS facility has been shown to be well suited for the study of pion correlations. With the Drift Chamber tracking and efficiency software now written and well understood, I believe future pion correlation experiments could be performed and analyzed in a relatively short period of time. The first system I'd like to see measured with the high precision possible using the HISS facility would be a heavy symmetric system such as Lanthanum on Lanthanum or larger. It would be interesting to see if the change in the shape of the pion source from oblate to prolate as one goes to heavier systems is correct. I think it would also be interesting to study a given asymmetric system in both configurations, heavy on light and light on heavy, at the same beam energy per nucleon, to see if there is any

systematic trend in the size of the chaoticity parameter. Finally, I believe that it will be very interesting to see the techniques of particle correlations applied in the analysis of data from the new four π electronic detectors currently being built for the study of RHIC (the HISS TPC and the 4π array at SIS).

References

[1] S.Y.Fung, W. Gorn, T. Kiernan, J. Lu, W. Oh, R. Poe, Phys. Rev. Lett. **41** 1592 (1978).

[2] J.J. Lu, D. Beavis, S.Y. Fung, W. Gorn, A. Huie, G. Kiernan, R. Poe, G. VanDalen, Phys. Rev. Lett. **46**, 898 (1981).

[3] D. Beavis, S.Y. Fung, W. Gorn, A. Huie, D. Keane, J.J. Lu, R. Poe, B. Shen, G. VanDalen, Phys. Rev. C **27**, 910 (1983).

[4] D. Beavis *et al*, Bulletin of the Amer. Phys. Soc. **28**, 703 (1983).

[5] D. Beavis, S.Y. Chu, S.Y. Fung, W. Gorn, D. Keane, R. Poe, G. VanDalen, M. Vient, Phys. Rev. C **28**, 2561 (1983).

[6] D.Beavis, S.Y. Chu, S.Y. Fung, D. Keane, Y.M. Lui, G. VanDalen, M. Vient, Phys. Rev. C **34**, 757 (1986).

[7] Y.M. Liu, D. Beavis, S.Y. Chu, S.Y. Fung, D. Keane, G. VanDalen, M. Vient, Phys. Rev. C **34**, (1986).

[8] J. Engelage *et al.*, Nucl. Instr. and Meth. A**277** 431 (1989).

[9] T. Kobayashi, F.S. Beiser, P.J. Lindstrom, T.J.M. Symons, D.E. Greiner, H.J. Crawford, Nuclear Instr. and Meth. A**254**, 281 (1987).

[10] T. Kobayashi *et al*, Nucl. Instr. and Meth. (1990).

[11] W. Christie, Masters Thesis, University of California, Davis 1985.

W. Christie, J.L. Romero, F.P. Brady, C.E. Tull, C.M. Castenada, E.F. Barasch, M.L. Webb, J.R. Drummond, H.J. Crawford, I. Flores, D.E. Greiner, P.J. Lindstrom, H. Sann, J.C. Young, Nucl. Instr. and Meth. A**255**, 466 (1987).

[12] S. Nagamiya, Dept. of Phys., Univ. of Tokyo, Bunk - Yo, Tokyo, Rep.# UTPN - 186.

S. Nagamiya, Proceedings, 3rd Int. Conf. on Ultra Relativistic Nucleus - Nucleus Collisions, Brookhaven National Lab. Sept. 1983.

[13] J. Hufner, K. Schafer, B. Schurmann, Phys. Rev. C **12**, 1888 (1975).

[14] D.J. Morrissey, W.R. Marsh, R.J. Otto, W. Loveland, G.T. Seaborg, Phys. Rev. C **18**, 1267 (1978).

[15] L.F. Oliveira, R. Donangelo, J.O. Rasmussen, Phys. Rev. C **19**, 826 (1979).

[16] S. Nagamiya, M.C. Lemaire, E. Moeller, S. Schnetzer, G. Shapiro, H. Steiner, I. Tanihata, Phys. Rev. C **24**, 971 (1981).

[17] H. Stocker, G. Buchwald, G. Graebner, P. Subramanian, J.A. Maruhn, W. Greiner, B.V. Jacak, G.D. Westfall, Nucl. Phys. A**400**, 63c (1983).

[18] R. Stock *et al*, Phys. Rev. Lett. **49** 1236 (1982).

[19] J. Cugnon, T. Mizutani, J. Vandermeulen, Nucl. Phys. A**352** 505 (1981).
J. Cugnon, D. Kinet, J. Vandermeulen, Nucl. Phys. A**379** 553 (1982).

[20] R. Hanbury - Brown and Twiss, Nature **178** 1046 (1956).

[21] E.V. Shuryak, Phys. Lett. **44**B 387 (1973).

[22] G.I. Kopylov and M.I. Podgoretskii, Sov. J. Nuc. Phys. **18** 336 (1974).

[23] G. Cocconi, Phys. Lett. **49**B 459 (1974).

[24] S.E. Koonin, Physics Lett. **70**B 43 (1977).

[25] F.B. Yano and S.E. Koonin, Phys. Lett. **78**B 556 (1978).

[26] M. Gyulassy, S.K. Kauffman, L.W. Wilson, Phys. Rev. C **20** 2267 (1979).

[27] W.J. Knox, Phys. Rev. D **10** 65 (1974).

[28] G. Goldhaber, S. Goldhaber, W. Lee, A. Pais, Phys. Rev. **120** 300 (1960).

[29] The Intensity Interferometer, R. Hanbury - Brown, Taylor and Francis, London (1974).

[30] The Feynman Lectures in Physics, R.P. Feynman, R.B. Leighton, M. Sands, Addison Wesley, Reading, Mass. Vol. 3, 4-3.

[31] W.A. Zajc, Ph.D. Thesis (1982) LBL report #14864.
W.A. Zajc *et al*, Phys. Rev. C **29** 2173 (1984).
W.A. Zajc, Nevis Lab report #1384, Columbia University.

[32] M.G. Bowler, Z. Phys. C - Part. and Fields **29** 617 (1985).

[33] M. Deutchmann *et al.*, Cern/EP/Phys 78 - 1 (1978).

[34] M. Gyulassy, Phys. Rev. Lett. **48** 454 (1982).

[35] H.J. Crawford and P.J. Lindstrom, LBL Report #16171.

[36] C. Lechanoine, M. Martin, H. Wind, Nucl. Instr. and Meth. **69** 122 (1969).

[37] D. Olson, Chebychev Momentum Reconstruction at HISS, Internal Hiss Document (1986).

[38] A. Shor *et al*, Phys. Rev. Lett. **63**, 2192 (1989).

[39] Data Analysis for Scientists and Engineers, Stuart L. Wilson, John Wiley & Sons, Inc.

[40] Particle Data Book, Particle Data Group, North - Holland Amsterdam.

[41] J.P. Sullivan *et al*, Phys. Rev. C, **25** 1499 (1982).

[42] H.M.A. Radi, J.O. Rasmussen, K.A. Frankel, J.R. Sullivan, H.C. Song, Phys. Rev. C, **27** 606 (1983).

[43] A.S. Goldhaber, Phys. Lett. **53**B, 306 (1974), see also H. Feshback and K. Huang, Phys. Lett. **47**B, 300 (1973).

[44] M. Gyulassy and S.K. Kauffmann, Nucl. Phys., A**362** 503 (1981).

[45] S. Pratt, Phys. Rev. Lett. **53**, 1219 (1984).

[46] P.J. Siemens and J.O. Rasmussen, Phys. Rev. Lett. **42**, 880 (1979).

[47] J. Bartke, Phys. Lett. B, **174** 32 (1986).

[48] D. Chacon *et al*, Phys. Rev. Lett. **60** 780 (1988).

[49] D. Chacon, Ph.D. Thesis, Reproduced as LBL Report # 28149. (1989).

[50] C. DeMarzo *et al.*, Phys. Rev. D **29** 363 (1984).

[51] G.N. Agakishiev *et al.*, Yad. Fiz. **39** 543 (1984).

[52] N. Akhababian *et al.*, Z. Phys. C**26** 245 (1984).

[53] K.M. Crowe *et al.*, Proc. 7th High Energy Heavy Ion Study (Darmstadt, Oct. 1984), Report GSI - 85 - 10 (Darmstadt, 1985) p. 801.

---

[54] D. Beavis *et al.*, Proc. 7th High Energy Heavy Ion Study (Darmstadt, Oct. 1984), Report GSI - 85 - 10 (Darmstadt, 1985) P 771.

[55] I. Tanihata, Proc. 7th High Energy Heavy Ion Study (Darmstadt, October 1984), Report GSI - 85 - 10 (Darmstadt, 1985) p. 413.

Appendix A

Conversion Factors.

In this appendix I will briefly discuss the conversion factors which are commonly used in two particle correlation analyses. Recall from chapter #1 that in deriving the two particle correlation function one finds that:

$$C_2(q,q_0) = 1 + |\rho\ (q,q_0)|^2$$

where $\rho\ (q, q_0)$ is the Fourier transform of the pion emitting source distribution. At this point one must choose a distribution for $\rho(\mathbf{r}, t)$. In Yano and Koonin's formulation, which I've used in this analysis, a gaussian distribution was chosen which was parameterized as:

$$\rho_1\ (r)\ d\mathbf{r} \propto c\ e^{(-r^2/R^2)} d\mathbf{r}.$$

In this discussion I will ignore the time component of the distributions for simplicity. The subscript on ρ is merely to allow me to refer to this particular gaussian parameterization below. This leads to a correlation function of the form:

$$C_2(q, q_0) = 1 + e^{-q^2R^2/2}.$$

When one fits this function to the data and quotes a radius parameter, the quantity being quoted is thus this parameter R, which is dependent on how one choose to parameterize one's gaussian.

The trouble that arises is that different theoretical formulations have used different algebraic forms for their gaussians and hence one must be careful when comparing the quoted radius parameters from different groups. As an example, some formulations parameterize their gaussians as:

$$\rho_2\ (r)\ d\mathbf{r} \propto c\ e^{(-r^2/2R^2)} d\mathbf{r}.$$

This leads to a correlation function of the form:

$$C_2(q, q_0) = 1 + e^{-q^2R^2}.$$

One may easily see that the extracted radius parameters for the two gaussian parameterizations given above will differ by a factor of $\sqrt{2}$. Recognizing this problem,

Bartke and Kowalski[45] suggested that if the results are quoted using the root mean square (rms) radii of the gaussians this ambiguity can be avoided. This is illustrated below.

Using ρ_1 above,

$$\frac{\int_0^\infty r^2 \rho_1(r)\, dr}{\int_0^\infty \rho_1(r)\, dr} = \frac{4\pi c \int_0^\infty r^4 e^{-r^2/R^2} dr}{4\pi c \int_0^\infty r^2 e^{-r^2/R^2} dr} = \frac{3R^2}{2} = \langle r^2 \rangle \rightarrow r_{rms} = \sqrt{\frac{3}{2}}\ R_1$$

Using ρ_2 above,

$$\frac{\int_0^\infty r^2 \rho_2(r)\, dr}{\int_0^\infty \rho_2(r)\, dr} = \frac{4\pi c \int_0^\infty r^4 e^{-r^2/2R^2} dr}{4\pi c \int_0^\infty r^2 e^{-r^2/2R^2} dr} = 3R^2 = \langle r^2 \rangle \rightarrow r_{rms} = \sqrt{3}\ R_2.$$

As we've already seen, $\sqrt{2}\, R_2 = R_1$, therefore two different groups could analyze the same experimental data, using the different parameterizations for their gaussians, and get the same result if they compare their rms radii.

Bartke and Kowalski also give various conversion factors to convert the extracted radius parameters (for example R_1 and R_2 above) to the rms radii for an equivalent sharp sphere with the pion emitters distributed uniformly inside. These conversion factors are calculated by equating the rms radii of the gaussian distributions with those for a uniform sphere, as illustrated below.

For a uniform spherical distribution;

$$\frac{\int_0^{R_u} r^2\, dr}{\int_0^{R_u} dr} = \frac{4\pi \int_0^{R_u} r^4\, dr}{4\pi \int_0^{R_u} r^2\, dr} = \frac{3R_u^2}{5} = \langle r^2 \rangle_u \rightarrow r_{rms} = \sqrt{\frac{3}{5}}\ R_u$$

Equating this to the rms radius for ρ_1 above;

$$\sqrt{\frac{3}{5}}\ R_u = \sqrt{\frac{3}{2}}\ R_1$$

$$\rightarrow R_u = \sqrt{\frac{5}{2}}\ R_1.$$

The conversion factors which Bartke and Kowalski have tabulated for converting to the rms radii for the various gaussian parameterizations are correct and applicable to two particle interferometry analyses. I don't believe the same can be said for their conversions to uniform spheres. The factors are correct but they are not applicable to two particle interferometry analyses. The problem lies in the fact that it is the Fourier transform of the gaussian and the uniform spherical distributions between which one wants to convert. Goldhaber, Goldhaber, Lee, and Pais[28] showed in their pioneering paper that the Fourier transform of a gaussian and a uniform spherical distribution are almost identical (within ≈ 2% everywhere) if one multiplies the width parameter for the gaussian by the appropriate constant.

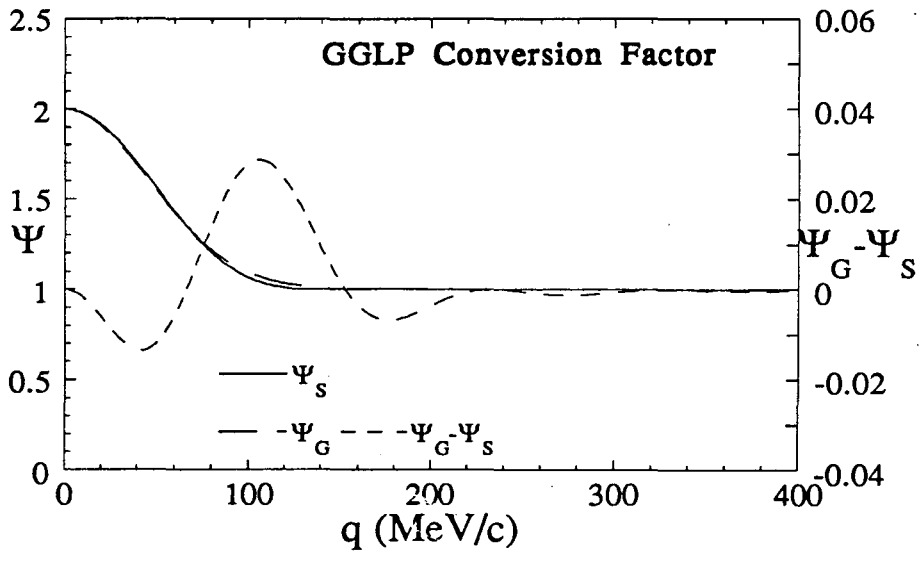

Figure #A1 GGLP Conversion Factor.

Figure #A1 shows the two pion correlation function derived using a uniform spherical distribution (Ψ_S), the same function derived using a gaussian distribution (Ψ_G), and the difference between the two.(Ψ_G - Ψ_S). In the plot I've used Ψ instead of C2(q) to be

consistent with GGLP's notation. One conclusion which may be drawn from this plot is that one cannot determine the shape of the source (spherical or gaussian) via the two pion interferometry method. In figure #A2 below I show the same plot where I've used the conversion factor between the gaussian and spherical distributions given by Bartke and Kowalski.[45]

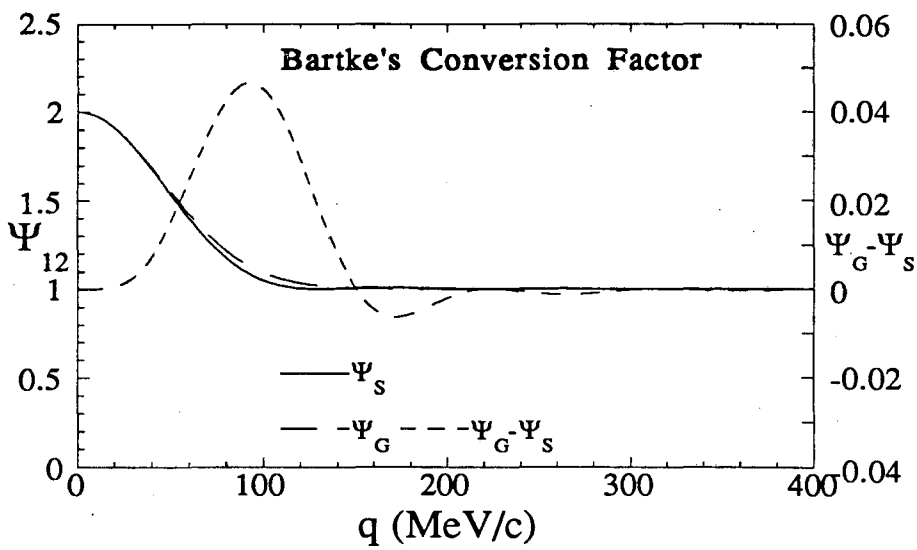

Figure #A2 Bartke's Conversion Factor.

It's clear from the comparison of figures #A1 and A2 that the deviation between the correlation functions which one derives using the uniform spherical and gaussian distributions of pion emitters is smaller when one applies GGLP's conversion factor.

From GGLP's paper the appropriate conversion factor between the gaussian and the uniform sphere is 1.52 if one uses the Yano - Koonin formulation (ρ_1), and 2.15 if one uses a gaussian parameterization of type ρ_2.

LAWRENCE BERKELEY LABORATORY
UNIVERSITY OF CALIFORNIA
INFORMATION RESOURCES DEPARTMENT
BERKELEY, CALIFORNIA 94720